Chapter 5.

keV and GeV irradiation induced modification of WS_2: Excitonic features and computational perspectives

5.1. Introduction

The remarkable physical and chemical properties of two-dimensional (2D) transition metal dichalcogenides (TMDCs) make them highly adorable for scientific investigation, particularly due to their immense potential for point defect formation and structural adaptability [1,2]. The intrinsic properties of TMDC systems can be tailored by intentionally introducing defects such as vacancies or impurities at substitutional and interstitial sites [3,4]. Recently, TMDCs have drawn significant attention because of their tunable electronic and optoelectronic properties enabled by defect engineering [5]. Among these, WS_2, a key member of the TMDC family, exhibit outstanding electronic, optical, and mechanical properties.

Ion beam irradiation is a highly promising physical technique for nanostructuring and modification of materials due to its exceptional control, purity and preciseness [6]. It can help alter surface microstructure, morphology, and, most notably, the electronic properties of the targeted material. The ion implantation process involves a multi-collisional process between incident ions and the target material, where the relative influence of two primary energy loss mechanisms, namely, electronic stopping (S_e) and nuclear stopping (S_n) are affected by factors such as projectile mass, atomic number, ion velocity, and the nature of the target atoms. These factors play a crucial role in the modification and defect manifestation of the material [7,8]. A key benefit of an ion implantation process is its ability to modify surface properties without subjecting materials to excessive electronic energy loss. During the process, implanted ions transfer energy to either the target atoms or the electronic subsystem before coming to rest within the material, eventually following a Gaussian distribution profile [9,10]. To tailor the near-surface properties of TMDCs, a low-energy, low-mass ion beam was selected, enabling controlled modification through ion implantation. In this approach, low-energy ion irradiation dominated by nuclear energy loss via elastic collisions frequently generates nanoscale point defects and induces localized stress within the material. These ion-matter interactions lead to significant alterations in the near-surface region, such as compositional changes, the formation of point defects, and notable micro-morphological transformations [11,12]. Most importantly, the nature and extent of these modifications depend on the type of ion used for implantation. Additionally, the relative concentration of interstitial and vacancy defects near the surface is influenced by the implantation energy, further affecting the structure of the material and functional properties [13].

Radiation-assisted modifications in geometry, crystal structure, chemical composition, and patterning can occur due to the strong interaction between energetic ions and the target material, as well as the associated energy loss mechanisms. In recent years, keV ion beam irradiation has been widely considered for doping and surface patterning of 2D materials with a high degree of precision and reproducibility. By adjusting the type and concentration of structural defects or disorders, ion beam irradiation is considered to be a powerful technique for implantation based defect engineering and tuning of band gaps in 2D materials [14].

Moreover, numerous experiments conducted at large-scale accelerator facilities have significantly advanced the understanding of swift heavy ions (SHI) interaction with target materials. SHI irradiation is also widely employed as a technique for structuring materials at the micro- and nanoscale [15]. The formation of ion tracks during irradiation can substantially alter the properties of a material. These ion tracks are observed in various solids, including certain metals and semiconductors, as well as in all types of insulators, such as polymers and inorganic materials. For patterning of materials, ion fluences in the range of 10^6 to 10^{11} ions/cm^2 are sufficient and can be readily achieved using a typical beam current of a few nA, or less [16].

Considering these aspects, this chapter reports the effects of low-energy 15 keV Helium (He), Carbon (C) ions with a charge state of +2 and Uranium (U) projectile ions with +28 charge state in the target of the WS_2 system. The structural, vibrational and morphological evidence of both 15 keV He^{2+}, 15 keV C^{2+} and 0.85 GeV U^{28+} ions are investigated and compared. These findings are crucial for manifesting the properties of WS_2 material and its implementation under different radiative conditions. The irradiation-led morphological, surface constructs, vibrational modes, and compositional features of the WS_2 specimens are discussed in subsequent sections. The altered structural, morphological, and electronic properties of the layered WS_2 before and after irradiation are also discussed, along with the first principles calculations on the role of defects and electronic band structure. Furthermore, the excitonic properties of WS_2 are explored after exposed to GeV irradiation.

5.2 Irradiation effect of WS_2 system with 15 keV He^{2+}, 15 keV C^{2+} and 0.85 GeV U^{28+} ions

Bulk and exfoliated WS_2 systems were irradiated using low-energy 15 keV He^{2+} and C^{2+} ions and high-energy 0.85 GeV U^{28+} ions. The low-energy experiments were conducted in the Variable Energy Cyclotron Centre (VECC) at Kolkata utilising the K130 variable energy cyclotron equipped with a 6.4 GHz electron cyclotron resonance (ECR) ion source. Bulk WS_2 system were irradiated with 15 keV He^{2+} ions, whereas 15 keV C^{2+} irradiation was performed on exfoliated forms of WS_2. For the irradiation experiments, the samples were prepared in powdered form and compressed into pellets using a 1.3×1.3 cm^2 area round teflon base. These pellets were then mounted on a flat rectangular ladder to ensure proper alignment for the ion beam. The experiments were conducted inside a high-vacuum target chamber at a ~10^{-6} mbar pressure. For He^{2+} irradiation at low energy of 15 keV, bulk WS_2 system were irradiated at fluences of 1×10^{15} ions/cm^2, 5×10^{15} ions/cm^2 and 1×10^{16} ions/cm^2 under normal incidence (0°). The schematic representation of projectile ions bombarded on the target at normal and oblique angle incidence is presented in the *Appendix* (Fig. A5). Furthermore, the WS_2 system was irradiated at an oblique angle of 55° with a mid-fluence of 5×10^{15} ions/cm^2. On the other hand, WS_2 systems in exfoliated form were irradiated with 15 keV C^{2+} ions at fluences of 1×10^{15} ions/cm^2, 3.5×10^{15} ions/cm^2, 7.5×10^{15} ions/cm^2, and 1×10^{16} ions/cm^2 under normal incidence. The following relation between the irradiation time (t), the ion fluence (φ), and the ion beam current (i) has been used during the irradiation experiment,

$$t = \frac{\varphi \times A \times n \times q}{i}, \tag{5.1}$$

where, A is the area of the pellet, n is the charge state, and q is the electronic charge. The beam current was monitored and maintained using a Faraday cup integrated into the chamber. An operating voltage of 7.5 kV and a maximum current of 1.5 μA was applied to achieve the +2 charge state for the projectile ions.

For the 0.85 GeV U^{28+} ion irradiation experiment, bulk and exfoliated WS_2 pellets were considered. The preparation of the samples employed for this work is based on a UMAT irradiation experiment, which was performed at the beamline X0 at the GSI Helmholtzzentrum für Schwerionenforschung, Darmstadt (Germany) in the frame of FAIR-Phase. Teflon-supported pellets, consisting of bulk and few-layer WS_2, were

exposed to uranium (U) ions at fluences, 1×10^9 ions/cm^2, 1×10^{10} ions/cm^2, and 1×10^{11} ions/cm^2 at normal incidence. To prevent any small fragments of the samples from falling into the irradiation chamber, all samples were shielded with a 10 µm-thick aluminium (Al) foil. This foil effectively reduced the specific energy of the U^{28+} ions with a mass of 238.08 amu from an initial 1.14 GeV to 0.85 GeV. Given the sample dimensions (~1.3×1.3 cm^2), the selected ion fluences were carefully chosen to minimize the overlapping of tracks and prevent melting or excessive damage.

5.3 Effect of 15 keV He^{2+} ion irradiation in few layer WS_2

5.3.1 SRIM-TRIM simulations

The SRIM® (Stopping and Range of Ions in Matter) [17] calculations that use the Monte Carlo simulation approach were performed to predict the transport of ions into the target matter. The parameters used in the TRIM calculations are described in *Appendix* A8. The three-dimensional (3D) plots as regards the distribution of ions and total displacements that occurred due to the bombardment of 15 keV He^{2+} ions onto the WS_2 material at 0° and 55° incident angles, respectively, can be found in *Appendix* (Fig. A6). To be specific, the ions can penetrate to a depth of 82.9 nm in normal incidence and 66.3 nm in oblique angle incidence. As the ions traverse a target material, the number of collisions required to bring ions to rest within the medium varies for each ion, and accordingly, there will be a variation in the penetration depth, referred to as straggling. The corresponding lateral straggling is around ~39.9 nm and ~35.7 nm in the cases of normal and oblique angle incidence, respectively. The number of atoms displaced and the vacancies generated for each ion, resulting from energy transfer as the ions moved through the target material, are shown in the *Appendix* (Fig. A6). The trajectories of He^{2+} ions penetrating the target material, the ion concentration versus depth profiles, and the vacancy plots for W and S atoms generated by primary knock-on collisions of He^{2+} ions in the WS_2 system for different fluences and considering both normal (0°) and oblique (55°) angles of incidences are presented in Fig. 5.1. Under normal incidence, greater displacements and more vacancies were produced compared to the oblique angle case. This is due to collisions between lattice atoms, which cause a larger area to be affected or damaged when the ion beam strikes at a normal incidence. In this regard, the peak maxima of vacancies generated arise at a depth of ~70 nm. Conversely, the peak maxima are closer to the surface, around 20 nm for an oblique

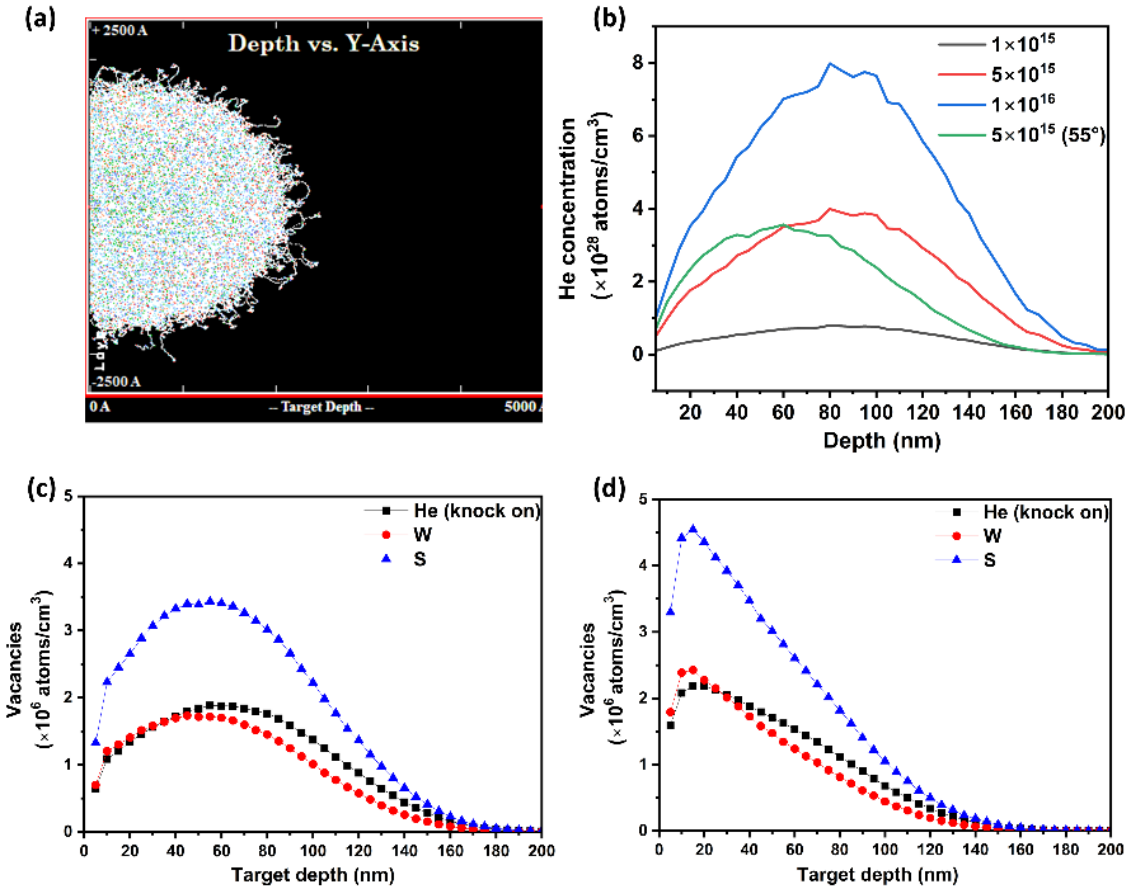

Figure 5.1: Ion implantation results from SRIM/TRIM simulations for 15 keV He^{2+} ions in WS_2, (a) ion trajectories, (b) He concentration vs. depth, (c,d) vacancies vs. depth, for 15 keV He^{2+} ions for normal (0°) incidence and for 55° incident angle, respectively.

angle incidence. In other words, the angle of incidence can have a profound effect on structural reordering and defect healing events.

5.3.2 Structural and surface compositional features

5.3.2.1 X-ray diffraction analysis

The powder diffraction patterns of bulk WS_2 in the pristine form and irradiated with 15 keV He^{2+} ions at fluences 1×10^{15}, 5×10^{15}, 1×10^{16} ions/cm^2 at normal incidence (0°), and 5×10^{15} ions/cm^2 at oblique angle incidence (55°) can be found in Fig. 5.2. The diffraction patterns were attained in the range of Bragg's angle, 2θ ~10°-70°. The diffraction pattern of pristine WS_2 (bulk) offers peak maxima at 2θ values ~14.54°, 29.12°, 44.2°, and 60.15°, which corresponded to (002), (004), (006), and (008) crystallographic planes, respectively. The assigned peaks in all the cases belong to the hexagonal crystal structure of WS_2 and match with the space group *P63/mmc* (Space group no. 194) according to the JCPDS file

no. 08-237 [18]. The prominent (002) peak located at 2θ~14.54º indicates the most favoured direction along the *c*-axis of the WS_2 crystallites. In addition, the lattice parameters were calculated from the acquired XRD patterns of the pristine and 15 keV He^{2+} irradiated WS_2 by employing the relevant formula of the hexagonal structure (Table 5.1). Moreover, the average crystallite sizes (d_c) were estimated using the most prominent (002) peak that appeared in WS_2 systems following Scherrer's law [19],

$$d_c = \frac{0.9\,\lambda}{\Gamma\, Cos\,\theta}, \tag{5.2}$$

and the micro-strain is given by the equation,

$$\varepsilon = \frac{\Gamma Cos\theta}{4}, \tag{5.3}$$

where λ = 1.543 Å and Γ is the full width at half maxima (FWHM) of the distinctive (002) peak fitted by single line peak fitting obtained in degrees and converted to radians. A reduction in the FWHM is observed for the irradiated samples as a consequence of the coalescence growth of crystallites with an increase in ion fluence [20].

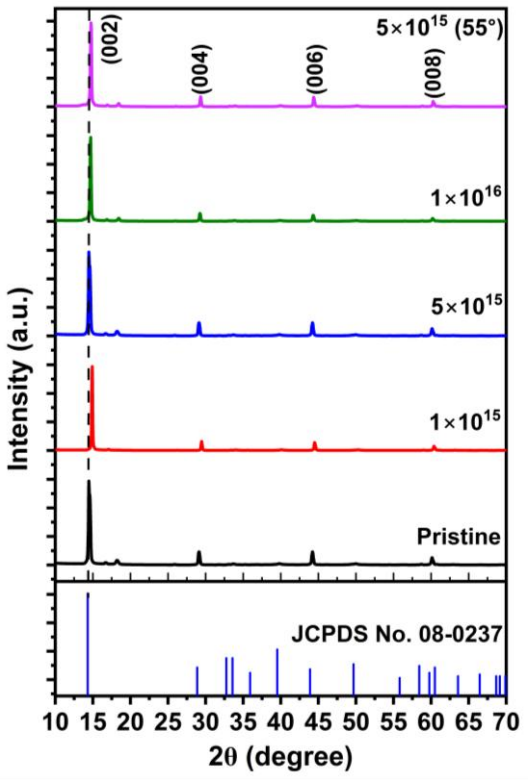

Figure 5.2: X-ray diffraction patterns of pristine (bulk WS_2) and 15 keV He^{2+} irradiated WS_2 systems at fluences 1×10^{15}, 5×10^{15}, 1×10^{16} ions/cm^2 at normal incidence (0º), and 5×10^{15} ions/cm^2 at oblique angle incidence (55º).

Table 5.1. Structural parameters of pristine and irradiated samples of bulk WS_2.

Sl. No.	Sample	Lattice parameter (Å) along the *c*-axis	FWHM (radian)	Average crystallite size, d_c (nm)	Micro strain, $\varepsilon \times 10^{-3}$
1	Pristine	12.18	0.0056	24.95	1.39
2	1×10^{15} (0°)	11.87	0.0028	50.46	0.69
3	5×10^{15} (0°)	12.04	0.0035	40.39	0.86
4	1×10^{16} (0°)	11.87	0.0027	51.96	0.67
5	5×10^{15} (55°)	12.00	0.0036	38.82	0.89

5.3.2.2 Raman spectra analysis

Raman spectroscopy is a versatile, non-invasive and widely used technique to determine the level of exfoliation, the introduction of defects and impurities in 2D materials. Raman spectra of pristine WS_2 (bulk), and 15 keV He^{2+} irradiated WS_2 at fluences of 1×10^{15}, 5×10^{15}, 1×10^{16} ions/cm^2 under normal incidence (0º), and 5×10^{15} ions/cm^2 at oblique angle incidence (55º) are shown in Fig. 5.3 (a). The acquired Raman spectra reveal first-order optical phonon modes with Raman peaks at ~348 cm^{-1}, 418 cm^{-1}, and 168 cm^{-1}, corresponding to E^1_{2g}, A_{1g}, and $LA(M)$ modes. The He^{2+} irradiation onto WS_2 results in adequate exfoliation of the layers by virtue of an increase in the vibrational intensity of the in-plane E^1_{2g} mode compared to the out-of-plane A_{1g} mode. The He^{2+} irradiation forming He bubbles accumulates at the trapping sites, and diffusion of these helium bubbles in between the layered sheets of WS_2 structures stacked together via weak van der Waal bonding leads to cracks as discussed in section 5.3.3.2. The formation of vacancies or interstitials, caused by the removal of sulfur atoms or the breaking of tungsten-sulfur (W-S) bonds through low-energy irradiation, leads to significant changes in Raman mode intensities. Additionally, the Raman peak observed at ~168 cm^{-1} corresponds to the longitudinal acoustic (*LA*) branch of the Brillouin zone, associated with zone-edge phonon modes. The appearance of this mode in the Raman spectra indicates the presence of defects or structural disorders, particularly under higher doses of helium ions. This *LA* (*M*) mode is attributed to Raman scattering induced by structural disorder at the *M*-point of the

Brillouin zone, where the momentum is $q \neq 0$ [21]. Furthermore, a column bar plot for a range of fluences illustrates the upsurge in the intensity ratios of E^1_{2g} to A_{1g} modes (Fig. 5.3 (b)). Besides, a drop in the intensities of E^1_{2g} and A_{1g} Raman modes could be observed, caused by the ablation of material as the ions bombard layered WS_2 at oblique angle incidence (55°). The separate plot of the pristine and He^{2+} irradiated WS_2 at a fluence of 1×10^{16} ions/cm^2 are displayed in Fig. 5.3 (c) to show the variation in the intensities of the Raman modes and the newly emerged $LA(M)$ mode associated with defects.

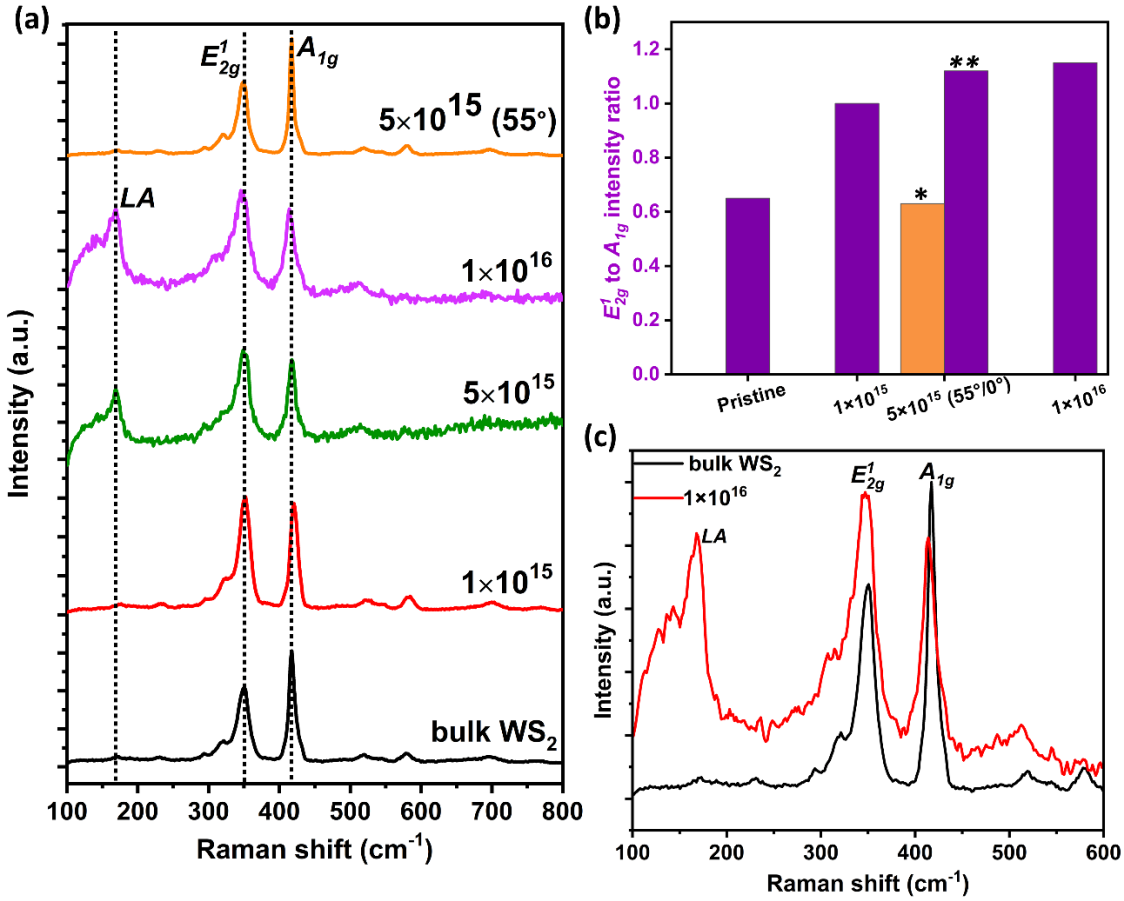

Figure 5.3: Raman spectra of WS_2 (a) before (pristine, bulk) and after 15 keV He^{2+} irradiation at fluences 1×10^{15}, 5×10^{15}, 1×10^{16} ions/cm^2 for normal incidence (0°) and also for an incident angle of 55° for the mid-fluence, (b) Column bar plot of intensity ratios of E^1_{2g} to A_{1g} modes attained from the Raman spectra displayed in Fig. 5.3 (a), (here, * denotes intensity ratio at oblique angle incidence and ** represent normal incidence which corresponds to specific ion fluence of 5×10^{15} ions/cm^2), (c) Zoomed view plot of pristine WS_2 and at the highest fluence of 1×10^{16} ions/cm^2 illustrating the variation in the intensities of the Raman modes after He^{2+} irradiation.

5.3.2.3 Core-level spectra analysis

The X-ray photoelectron spectroscopy (XPS) was utilized to analyze the surface chemical compositions and elemental information of the bulk and 15 keV He^{2+} ion irradiated WS_2 at a fluence of (5×10^{15} ions/cm^2), displayed in Fig. 5.4. The survey scans of WS_2 system before and after irradiation can be found in Fig. 5.4 (a,b). The W 4*f* core level spectra of the WS_2 system were deconvoluted through multi-peak Gaussian fitting, revealing W $4f_{7/2}$ and W $4f_{5/2}$ states of tungsten corresponding to two distinct peaks positioned at ~31.0 eV and 33.0 eV, respectively [22]. In addition, a peak arises at ~33.8 eV, attributable to the development of WO_3, belonging to a higher oxidation state (+6) of W. The relatively weak peak of the W^{+6} oxidation state corresponding to the W $4f_{7/2}$ of WO_3 suggests the adsorption of oxygen (O_2) molecules at the vacancy sites of WS_2 layers. The lack of a WO_3 peak in the XRD results (Fig. 5.4) supports that the W^{+6} peak is due to adsorbed oxygen [23]. Moreover, the W $5p_{3/2}$ state of tungsten is observed as a broad peak around ~36.5 eV. In contrast, two distinct peaks at ~160.5 eV and ~161.6 eV correspond to the sulfur states, S $2p_{3/2}$ and S $2p_{1/2}$, as illustrated in Fig. 5.4 (c,d).

The XPS spectra indicate a significant shift towards higher binding energies for both W and S after 15 keV He^{2+} irradiation at a fluence of 5×10^{15} ions/cm^2 (Fig. 5.4 (e, f)).

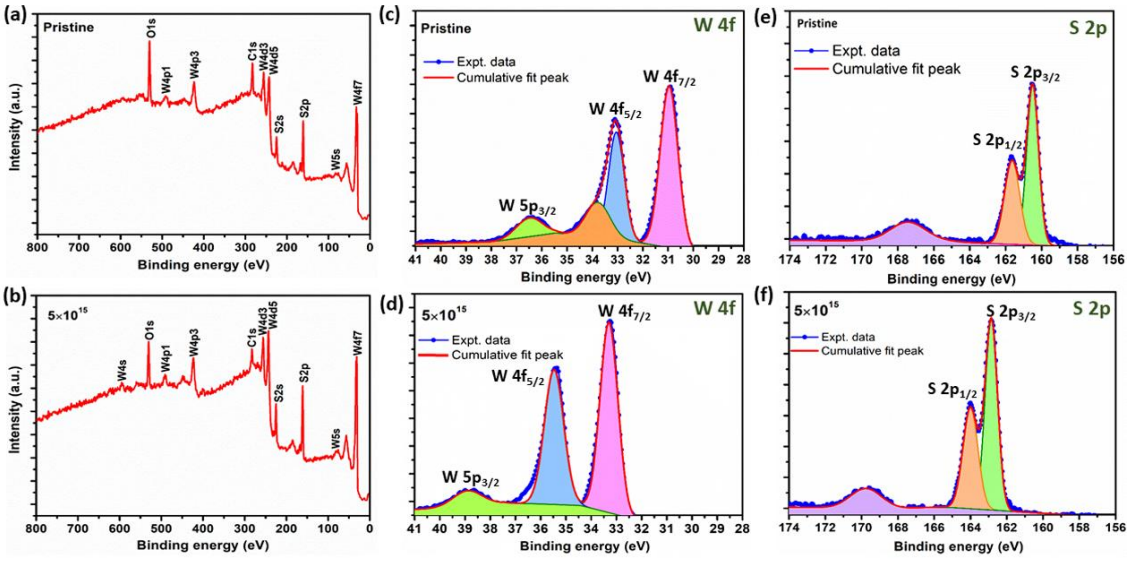

Figure 5.4: XPS survey scan of (a) pristine, (b) irradiated sample with fluence 5×10^{15} ions/cm^2; spectra of (c) W 4*f*-core level of the pristine case, (d) W 4*f*-core level of irradiated specimen, (e) S 2*p*-core level of pristine case, (f) S 2*p*-core level of irradiated specimen.

For example, the irradiated WS_2 sample exhibits tungsten states W $4f_{7/2}$ and W $4f_{5/2}$ positioned at ~33.3 eV and ~35.5 eV, respectively, along with the W $5p_{3/2}$ state at around 38.9 eV. These peak positions, corresponding to their respective binding energies, suggest the W^{4+} valence state of tungsten, which aligns with the phase-pure structure of WS_2 reported in earlier studies [24]. To be mentioned, the oxidized state of tungsten could not be traced after He^{2+} ion irradiation. Furthermore, the peaks of the irradiated WS_2 system tend to shift towards a higher binding energy of the S element as compared to the pristine WS_2. They are located at ~162.8 eV and ~164.0 eV and attributed to S $2p_{3/2}$ and S $2p_{1/2}$ states of divalent sulfide ions and specify the 2H phase of the semiconductor. The peaks detected at ~167.4 eV for the bulk and the one at ~169.8 eV for the irradiated case might have arisen owing to the presence of a (+6) S state of oxidized sulfur. The presence of O 1*s* and C 1*s* can be due to oxygen and carbon adsorbed into the material's surfaces during the processing stage, which leads to a lowering of intensity with irradiation. Nevertheless, a noticeable shift in the W and S-core level spectral features would indicate considerable charge transfer in the system after ion irradiation [25].

5.3.3 Morphological and surface topographical analysis

5.3.3.1 Exfoliation and slipping of layers through bubble formation

High-resolution transmission electron microscopy (HRTEM) images were obtained to analyse the morphological variations in the WS_2 system after irradiation with 15 keV He^{2+} ions at a fluence of 5×10^{15} ions/cm^2. The He^{2+} irradiation was carried out at normal incidence (θ = 0°) and oblique incidence (θ = 55°), as shown in Fig. 5.5 and 5.6. The pristine WS_2 appears as layered sheets arranged in stacks (Fig. 5.5 (a,b)). While after irradiation at a fluence of 5×10^{15} ions/cm^2 at normal incidence, various morphological features are observed. The WS_2 system displays deformed as well as nice, exfoliated rectangular sheets. Additionally, the partial formation of localized inorganic fullerene (IF)-like structures with polyhedral morphologies is observed after helium ion exposure (Fig. 5.6 (a,b)). These IF-like WS_2 structures exhibit sharp corners and edges due to the pronounced bending of the layered facets. Unlike carbon-based Buckminster fullerenes, such as C_{60}, C_{70}, or C_{84}, which have hollow cores formed by the buckling of hexagonal networks, IF-like WS_2 structures may not necessarily adopt the same hollow cage-like configuration [26]. It is assumed that the layered WS_2 nanosheets, composed of only a few

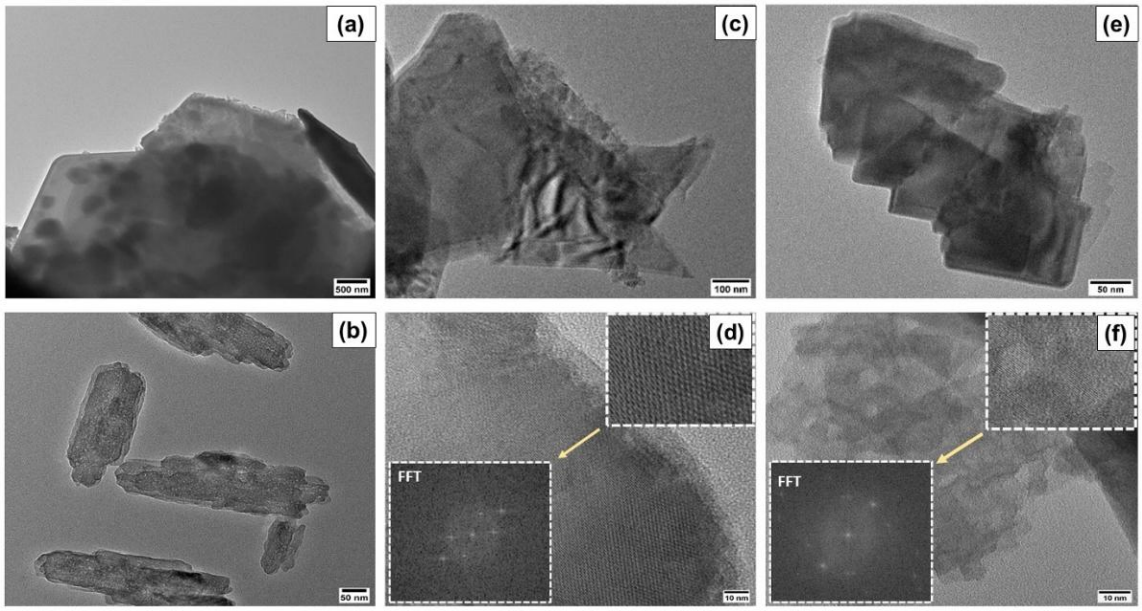

Figure 5.5. HR-TEM images of the (a,b) pristine (bulk WS_2), (c) lower magnified image of crumpled sheets, (d) higher magnified image of multi-sheets, (e) lower magnified image of slipping of sheets, and (f) higher magnified image of several sheets. The FFT images are shown as insets in the bottom left corner of the zoomed images shown in the top-right corners, after irradiation at a fluence of 5×10^{15} ions/cm^2 at normal angle incidence (0°) and at an oblique angle incidence (55°), respectively.

layers, may develop curvature or fold into IF-like structures due to internal stress gradients. This transformation could be facilitated by the abundance of dangling bonds and active functional sites at the edges of the sheet, which may interact with structural defects induced by irradiation, such as sulfur vacancies or edge dislocations. These interactions are likely to promote the curling of the sheets, contributing to their thermodynamic stability [27]. Thus, the difference in the origin of an IF-like structure in the present case, concerning the conventional fullerene, lies in local defect sites and vacancies created in the basal plane of the WS_2 system. Along with partial IF-like morphological evidence, several displaced and disrupted sheets with kinks were observed under the normal incidence of ions (Fig. 5.6 (c)).

In contrast, under oblique incidence, sliding or slipping of the layered sheets is observed (Fig. 5.5 (e) and 5.6 (d)). The fast Fourier transform (FFT) images, provided as insets in Fig. 5.5 (d, f), reveal hexagonal patterns, which is a characteristic of the irradiated WS_2 structure. With the oblique angle incidence of 15 keV He^{2+} ions, the development of helium bubbles and its collapse within the van der Waal bonded WS_2 layers caused

noticeable exfoliation and sliding of sheets/layers to varying degrees, resembling slipped playing cards (Fig. 5.6 (d-g)). As the sheets gradually separate from the stack, smooth, rectangular-shaped structures become visible (Fig. 5.6 (d)). The schematic illustration of He^{2+} irradiation on the WS_2 system, both at normal and oblique angle incidences, can be found in Fig. 5.7. The TEM images of these systems at normal and oblique angle incidences resulted in an interlayer spacing of ~0.35 nm of the WS_2 layers, indicating no expansion or contraction of the crystal planes (Fig. 5.6 (c,f)). The selective area electron diffraction (SAED) pattern of the irradiated system, obtained at a normal incidence angle,

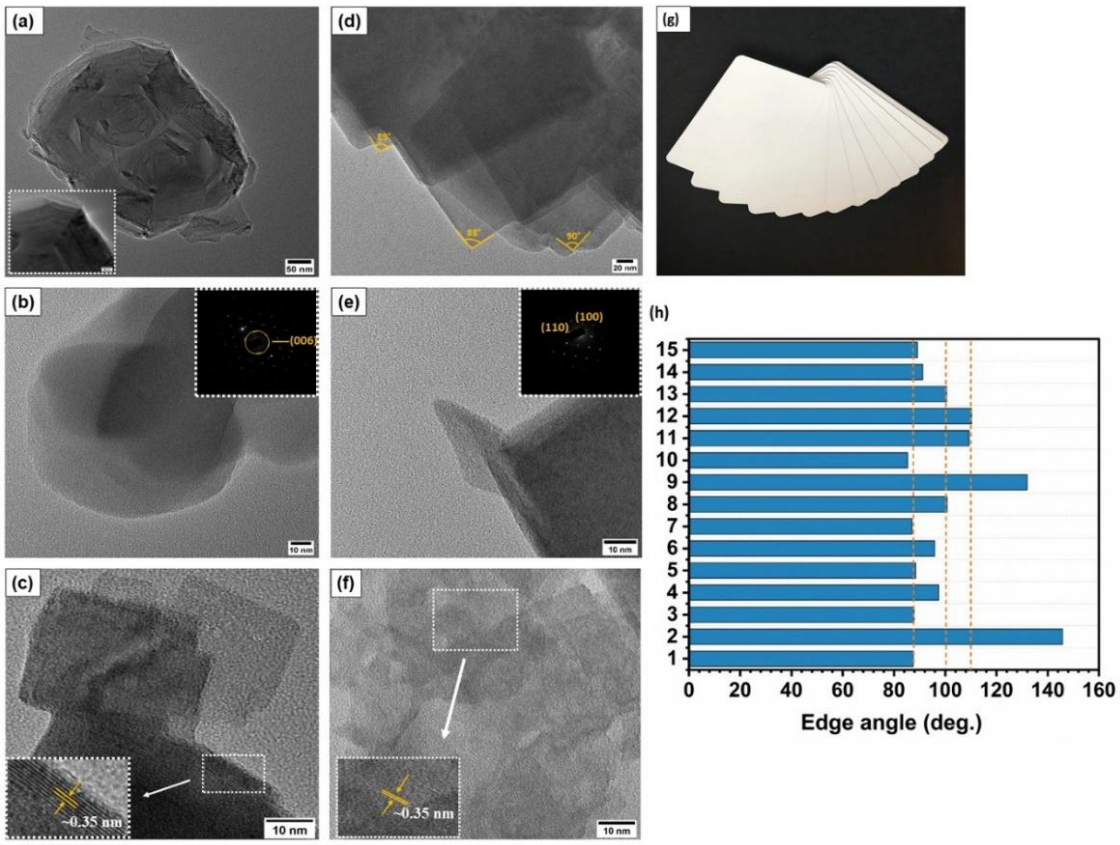

Figure 5.6: HR-TEM images of irradiated WS_2 at a fluence of 5×10^{15} ions/cm^2, (a) inorganic fullerene-like structure with bend edges after irradiation at normal angle incidence (0°); note that higher magnified image of irradiated system is shown as an inset in the bottom left corner (scale bar: 20 nm), (b,c,e,f) higher magnified imaging (scale bar: 10 nm) with SAED pattern shown as an inset in Fig. 5.6(b,e) at 0° and 55° incident angle, respectively, (d) Sliding of exfoliated sheets after irradiation at an oblique angle incidence (55°), (g) displayed playing cards that resemble slipped layers or sheets (Source:https://i.etsystatic.com/31648153/r/il/032b02/3289436322/il_794xN.3289436322_s2n2.jpg), (h) a bar graph depicting edge angles of the slipped rectangular sheets.

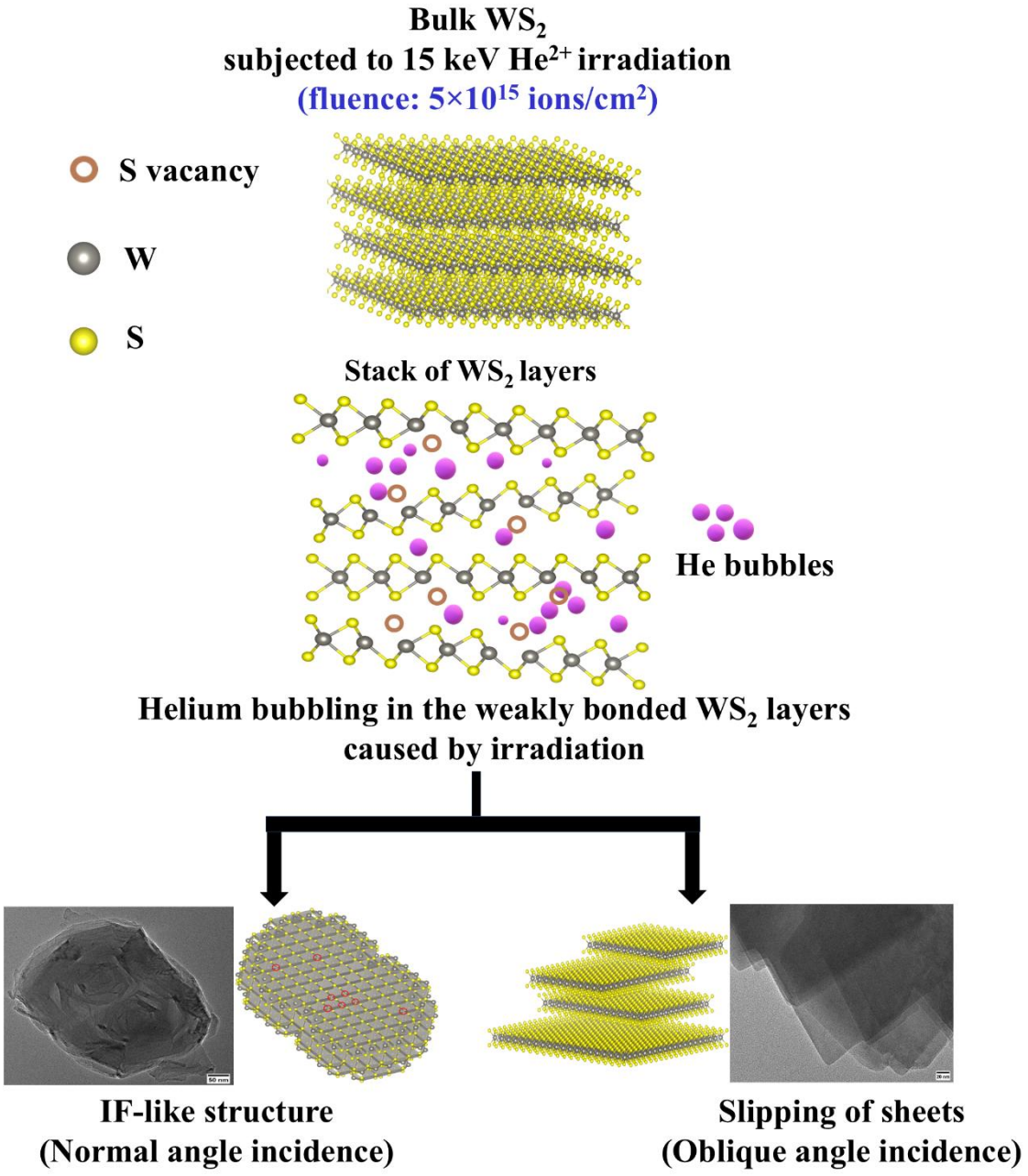

Figure 5.7: Schematic representation of the effect of 15 keV He^{2+} ion irradiation through bubble formation on the WS_2 system, resulting in an inorganic fullerene (IF)-like structure and slipped sheets under normal (0°) and oblique angle incidence (55°), respectively. (Published on the back cover page of *Physica Status Solidi (b)*, 260 (6), 2200598)

reveals the hexagonal pattern of WS_2, indexed to the (006) crystal plane (Fig. 5.6 (b)). However, at an oblique incidence angle of 55°, distinct diffraction spots emerge, confirming the monocrystalline nature of the WS_2 nanosheets, which are oriented along the (110) and (100) planes of 2H-WS_2 (Fig. 5.6 (e)). Additionally, measurements of the edge angles of various rectangular sheets in the stack varied in the range of ~80°-140°. A

series of bars representing these measured angles under different conditions is shown in Fig. 5.6 (h).

5.3.3.2 2D surface scans, 3D topography and its height profiles

Atomic force microscopy (AFM) imaging was conducted to examine the surface morphology of both pristine and 15 keV He^{2+} irradiated WS_2 systems, as shown in Fig. 5.8. The surface morphology, texture and the corresponding 3D topography were derived

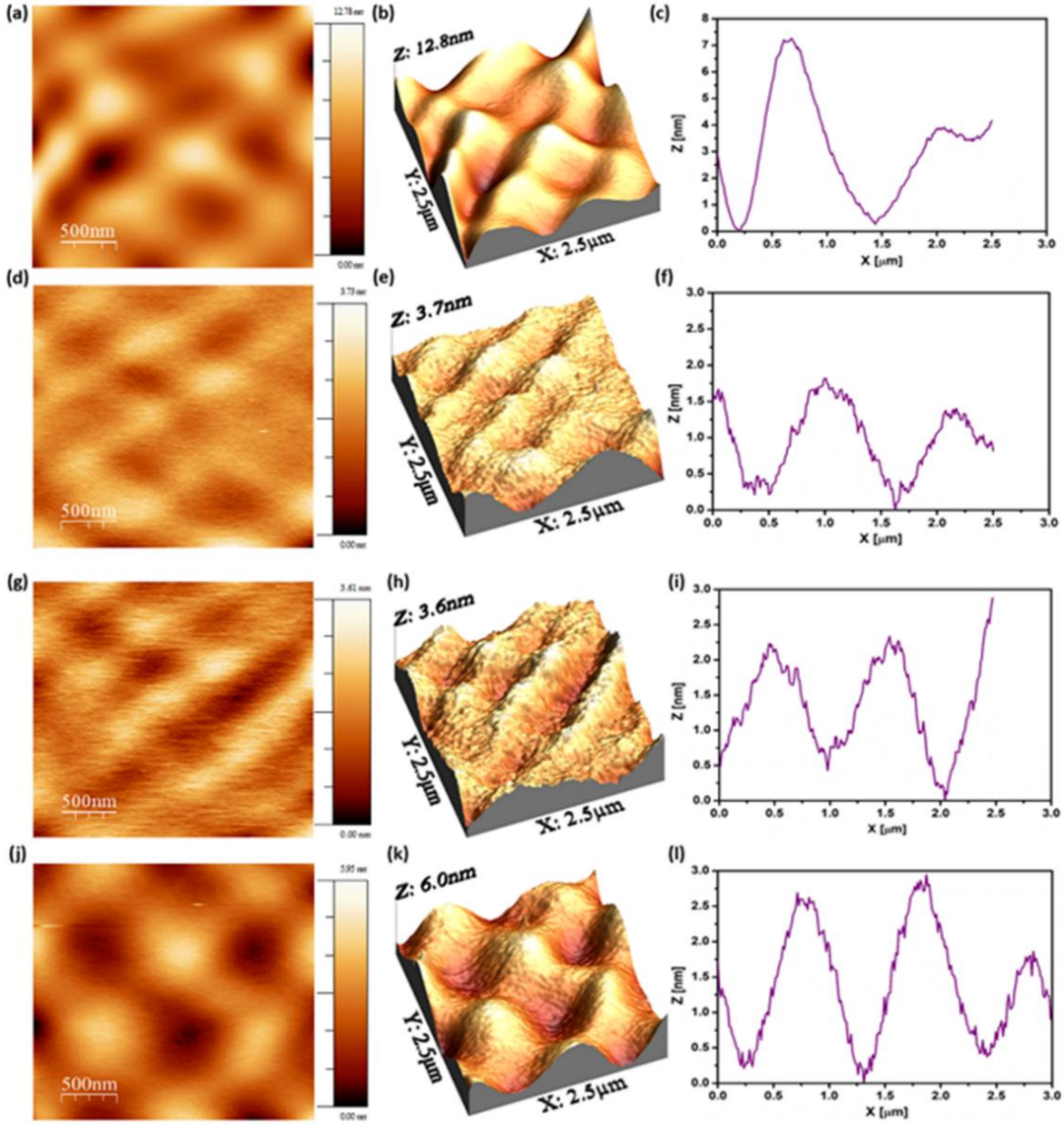

Figure 5.8: AFM images of 2D surface scans, 3D topology and height profiles, respectively of (a-c) pristine (bulk WS_2) and irradiated with fluence of (d-f) 1×10^{15} at normal incidence (0°), (g-i) 5×10^{15} ions/cm^2 at 55º incident angle, (j-l) 1×10^{16} ions/cm^2 at normal incidence (0°).

Table 5.2. RMS roughness measured for pristine WS_2 (bulk) and 15 keV He^{2+} irradiated WS_2 system from the acquired AFM images are tabulated. (Sample at Sl. No. 4 corresponds to irradiation at a tilting angle of 55°.

Sl. No.	Energy	Fluence (ions/cm^2)	RMS roughness (nm)
1	15 keV He^{2+} ion	Pristine	1.81 ± 0.13
2		1×10^{15} (0°)	0.36 ± 0.03
3		1×10^{16} (0°)	0.87 ± 0.09
4		5×10^{15} (55°)	0.48 ± 0.07

using WSxM 5.0 (Nanotec, Inc.) software [28], from 2D surface scans taken at specific locations (Fig. 5.8 (a,d,g,j)). Notably, the hillocks observed in pristine WS_2 tend to diminish in height, resulting in corrugated surface structures upon both normal and oblique angle incidence, as illustrated in Fig. 5.8 (b,e,h,k). The root-mean-squared (RMS) roughness determined by analysing the AFM images is presented in Table 5.2. Compared to bulk WS_2, the RMS roughness decreases upon irradiation, though it is significantly influenced by the angle of incidence (normal or oblique), with values ranging from ~0.36 to 0.87 nm [29,30]. Thus, the irradiation-induced displacement of tungsten (W) and sulfur (S) atoms, generating point defects such as vacancies, interstitials, results in these types of structures.

Moreover, the diffusion of helium plays a crucial role in bubble formation and growth, primarily governed by the ratio of helium production to atomic displacement rates. The accumulation of helium at adequate concentrations (doses) within the target material is often accompanied by displacement damage and temperature effects [31]. These defects may subsequently form various complexes, known as He_nV_m clusters, while He^{2+} ions can utilize vacancies or voids as trapping sites [32]. These sites exhibit low electron density due to the implantation process. As these defects nucleate within the lattice, they lead to the formation of vacancy clusters and helium-infused nanovoids, which are nearly spherical structures containing hollow regions at the nanometer scale. Over a certain period, these nanovoids aggregate to form bubbles through the co-precipitation of helium

ions and vacancies, leading to an increase in internal pressure. The bubbles then transform into platelets, undergo elastic interactions, and eventually merge to form micro-cracks. These cracks expand due to stress accumulation. Chemically inert helium ions become charge-neutral and diffuse through the lattice, promoting localized nucleation within the projectile range. As a result, bubble formation weakens van der Waals forces, giving rise to exfoliated and corrugated surfaces. With an increase in irradiation dose, defect and vacancy concentrations rise significantly. At a critical dose of 1×10^{16} ions/cm^2 under normal incidence, nanovoids may form beneath the surface. These helium bubbles, embedded within the solid, serve as stable sites for impurity retention. Thus, atomic displacements, associated vacancies, self-interstitial atoms, and defect clusters all influence helium diffusion under He^{2+} irradiation. In contrast, no such globular structures are observed in angle-dependent cases, likely due to the reduced number of defects formed, as substantiated by SRIM calculations (Fig. 5.1 (c,d)).

5.4 Effect of 15 keV C^{2+} ion irradiation in nanoscale WS_2: Experimental and theoretical perspectives

5.4.1 SRIM/TRIM calculations

SRIM calculations were performed for 15 keV C^{2+} ions to understand the dominant energy loss mechanisms in the WS_2 system. A +2 charge state was considered during the ion irradiation experiment to achieve the desired beam energy of 15 keV. Although referred to as C^{2+} ions to distinguish the incident ions from the target atoms, the ions become neutralized upon entering the target by capturing electrons and form atomic C [33]. From SRIM calculations, the energy *vs.* stopping power graph was plotted to examine the interaction of C ions with the target matter. Whereas electronic energy loss (S_e) is ~13.39 eV/Å, nuclear energy loss (S_n) is ~11.30 eV/Å, thereby offering an energy loss ratio of 1.18 and favouring competitive events (Fig. 5.9 (a)). With a lateral and longitudinal straggling of ~18.2 nm and ~24.1 nm, respectively, and the projected range of ions ~25.6 nm, it is apparent that ions would impinge on the surface of the target as the overall thickness of the specimen is larger than the calculated projected range. While electronic energy loss proceeds via inelastic collisions of C ions with the electronic sub-system of the host atoms (WS_2 layer), both S_n and S_e contribute largely to the slowing down of projectile ions.

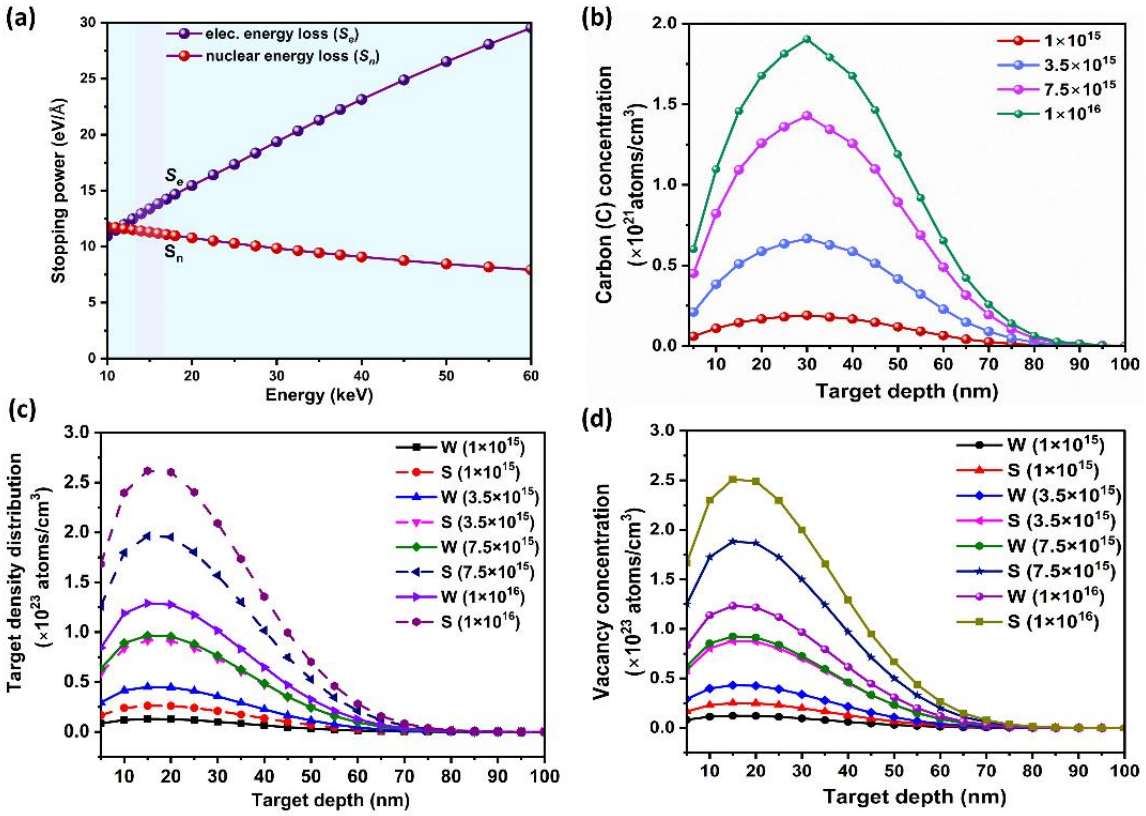

Figure 5.9: SRIM/TRIM calculation with 15 keV C^{2+} ion irradiation, (a) shows the stopping power *vs.* energy plot to determine the primary cause of energy loss into the target material, i.e., WS_2, after Carbon (C) irradiation, (b) C concentration *vs.* target depth, (c) target density distribution *vs.* target depth, and (d) vacancy concentration *vs*. depth.

Collision cascades under energetic ion irradiation were studied using TRIM calculations, which consider every recoil atom until its energy lowers below the displacement energy of any target atom. The primary knock-on atom (PKA) generated in the WS_2 target due to energetic incident ions induces displacement atoms through cascade collision. In the process of target atom displacement, vacancy, and interstitial atoms are generated. These damage events and the density distribution plots were computed for C ions in the WS_2 target using TRIM calculations. The parameters used in the TRIM calculations are described in *Appendix* A8. The C concentration *vs.* target depth shows the impacted region or the target depth of the material influenced by ions into the sample surface. The depth of influence was up to ~80 nm. The density distribution and vacancy formation were observed to be maximum for S at the highest fluence (1×10^{16} ions/cm^2) affecting the near-surface region, i.e., ~20 nm (Fig. 5.9 (b-d)). The 3D plots of target

displacements and recoil distribution taking place due to the bombardment of incident C ions into the WS_2 target are shown in the *Appendix* (Fig. A7).

5.4.2 Phase structure and vibrational analysis

5.4.2.1 X-ray diffraction study

The XRD diffraction patterns of pristine and 15 keV C^{2+} ion irradiated exfoliated WS_2 were acquired in the range of Bragg's diffraction angle, 2θ~10°-80° (Fig. 5.10 (a)). The diffractograms of WS_2 exhibited peaks located at ~14.49º, 29.26º, 44.29º, and 60.21º and are attributed to (002), (004), (006), and (008) crystallographic planes, respectively indexed with JCPDS card no. 08-237 [18]. Additionally, poorly resolved peaks appeared at ~33.66º, 39.50º, and 49.78º, which corresponded to (101), (103), and (105) diffraction planes of the material after irradiation and above the fluence of 3.5×10^{15} ions/cm^2. The intense (002) plane that emerged in all the XRD patterns corresponds to the hexagonal phase structure of WS_2 and is assigned to *P63/mmc* (Space group no. 194). However, the peak intensity of the (002) plane was suppressed at 3.5×10^{15} ions/cm^2. The lattice parameters along the *c*-axis of the WS_2 hexagonal crystal structure and the average crystallite size (d_c) were calculated by Voigt curve fitting of the most intense peak corresponding to the (002) plane of pristine WS_2 and irradiated systems via Scherrer's law, using equation 5.2, which can be found in Table 5.3. Additionally, XRD peak broadening resulting from irradiation can be analyzed to measure the degradation in crystallinity. Irradiation affects the lattice structure and long-range order of the material. Its impact on crystallite size, particularly in the presence of competing S_e and S_n, can also be evaluated through changes in the XRD peak broadening. Thus, the irradiation-induced disorder (%) is quantified by measuring the relative change in the FWHM of the (002) peak compared to the pristine sample. It is estimated using the following equation [34],

$$\text{disorder} = \frac{\text{FWHM}_{(002)\_\text{irradiated}} - \text{FWHM}_{(002)\_\text{pristine}}}{\text{FWHM}_{(002)\_\text{pristine}}}, \tag{5.4}$$

where $\text{FWHM}_{(002)\_\text{pristine}}$ and $\text{FWHM}_{(002)\_\text{irradiated}}$ are the FWHM of the (002) diffraction peak for the pristine and irradiated samples.

Upon irradiation, some low-intense peaks have appeared at 2θ ~30.76º, 35.20º, and 72.98º and were predicted to fit the respective crystallographic planes (001), (100), and

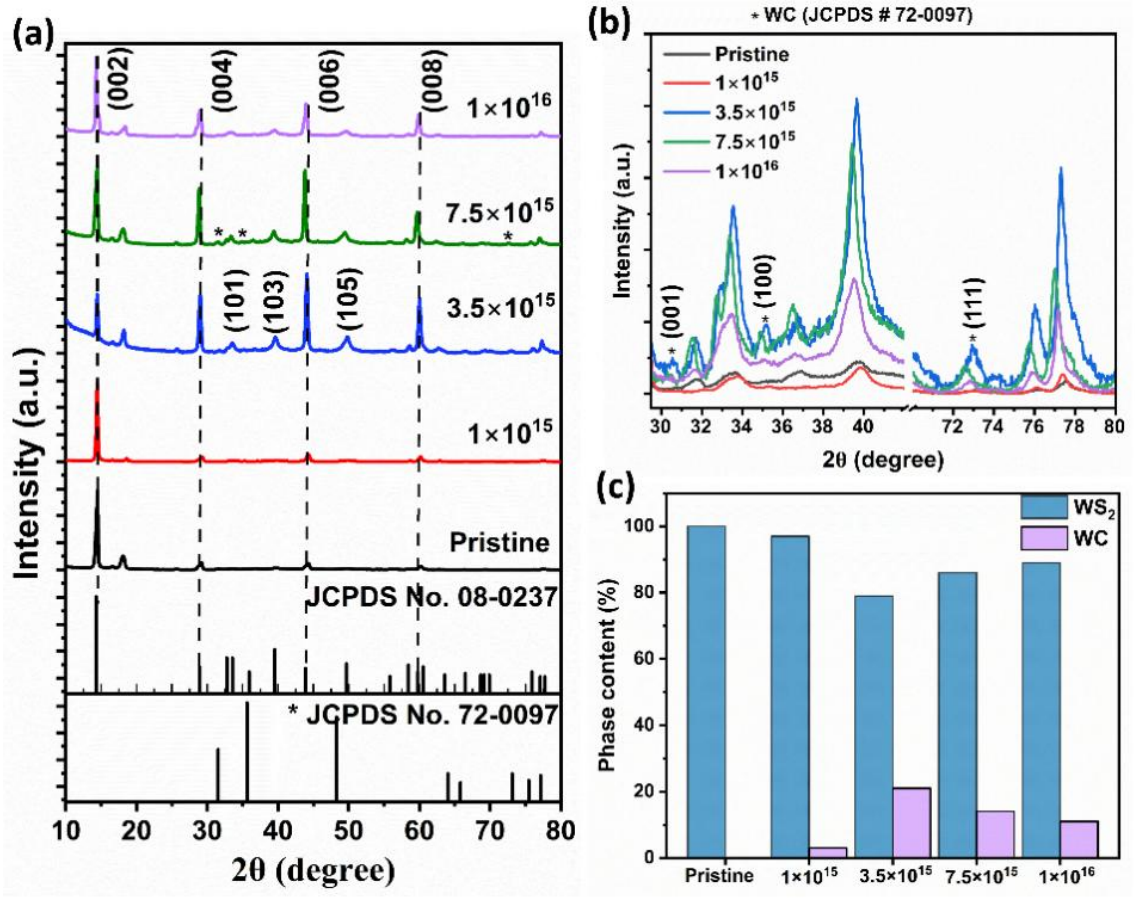

Figure 5.10: (a) XRD patterns, and (b) resolved plot of pristine (exfoliated WS_2) and irradiated WS_2 at fluences 1×10^{15}, 3.5×10^{15}, 7.5×10^{15}, and 1×10^{16} ions/cm^2, (c) plot for phase content of WS_2 and WC after C^{2+} irradiation with varying fluences.

(111) of WC by JCPDS card no. 72-0097 (Fig. 5.10 (b)) [35]. The observed peaks are slightly shifted towards the lower *2θ* value from the standard data. These results specify partial phase transformation to tungsten carbide (WC), which would form locally upon a combinatorial effect of the formation of chalcogen vacancies and insertion of C ions in the host lattice of WS_2. Additionally, irradiation can create adequate vacancies, and their uneven distribution could induce microstrain within the crystal lattice, thereby offering a significant impact on the characteristics of these carbides. The localized WC belongs to *P-6m2* (Space group no. 187), bearing a hexagonal phase. The lattice parameters for the WC phase oriented along the '*a*' and '*b*' axes are calculated to be ~2.95 Å and ~2.77 Å along the '*c*' axis. These deviate little from the lattice constants calculated from the standard file, where $a = b = 2.91$ Å and $c = 2.84$ Å. There is a negligible variation in the *a* or *b*-axis direction, while a slight shift of 0.07 Å in the *c*-axis direction can be observed when comparing our obtained results with the standard one. Thus, the coexistence of the WC-

Table 5.3. Structural parameters of pristine and 15 keV C^{2+} irradiated WS_2 exfoliated systems.

Sl. No.	Energy	Sample (fluence in ions/cm^2)	Lattice parameter (Å) along the *c*-axis	FWHM (002) in degree	Crystallite size (d_c) in nm	Disorder (%)
1	15 keV C^{2+} ion	Pristine	12.22	0.34±0.01	23.37	-
2		1×10^{15}	12.26	0.26±0.00	30.43	23.3
3		3.5×10^{15}	12.26	0.24±0.01	33.01	29.3
4		7.5×10^{15}	12.26	0.42±0.01	19.33	20.9
5		1×10^{16}	12.39	0.22±0.01	36.92	36.6

Table 5.4. Phase content of WS_2 and WC upon 15 keV C^{2+} ion irradiation.

Sl. No.	Energy	Sample (fluence in ions/cm^2)	WS_2 content (%)	WC content (%)
1	15 keV C^{2+} ion	Pristine	100	0
2		1×10^{15}	97	3
3		3.5×10^{15}	79	21
4		7.5×10^{15}	86	14
5		1×10^{16}	89	11

WS_2 phase is observed above a critical fluence of low-energy 15 keV C^{2+} irradiation. Similar results have been reported in other systems. Bhowmick *et al*. reported the bombardment of silicon with 14 keV N_2^+ ions at a grazing incidence angle of 70°, using an ion fluence of 1×10^{18} ions/cm^2 [36]. Subsequently, 5 keV C^+ ions were implanted at a fluence of 1×10^{17} ions/cm^2 on selective sites of pyramidal nano-templates, resulting in carbon dots (CDs) that were predominantly amorphous, along with silicon carbide (SiC) and graphitic nitrogen (CN) [36]. The same group also observed SiC formation on Si

surfaces under 10 keV C^+ bombardment at an ion fluence of 2×10^{17} ions/cm^2 [37]. In another study, carbon ion irradiation of Ti at fluences of 1.2×10^{17} - 3.6×10^{17} C^+/cm^2 and energies of 30-180 keV led to the formation of TiC [38]. In addition, the phase analysis was carried out by using advanced software, and the phase content of WS_2 and WC is presented in (Fig. 5.10 (c)) and Table 5.4. Additionally, the peak intensity of WC content drops above a specific fluence of 3.5×10^{15} ions/cm^2. This might be due to the probable formation of clusters of C atoms with higher fluences discussed later through TEM imaging (Fig. 5.16 (c)).

5.4.2.2 Raman spectra analysis

The Raman spectra of pristine and 15 keV C^{2+} ion irradiated exfoliated WS_2 can be found in Fig. 5.11 (a). The first-order, zone-centre optical phonon modes are noticeable at ~352 cm^{-1} and 421 cm^{-1}, belonging to the in-plane vibration between tungsten (W) and sulfur (S) atoms, denoted by the E^1_{2g} (Γ) mode and out-of-plane vibration among the S atoms between the successive layers are labelled as A_{1g} (Γ) mode of the *2H*-WS_2 system, respectively. The shoulder peak at ~324 cm^{-1} would represent the *2LA* (*M*)-E^2_{2g} (Γ) mixed mode, while *LA* is a longitudinal acoustic mode in the low-frequency region of the Raman spectrum. Also, the combinatorial peak at ~583 cm^{-1} signifies the A_{1g} (*K*) + *LA* (*K*) mixed mode [39]. Likewise, the emergence of a peak near ~170 cm^{-1} characterizes the *LA(M)* acoustic mode, which was absent before radiation exposure [40]. This *LA*(*M*) mode arises due to a double resonance process, signifying the presence of defect states, resulting in additional pathways for phonons in the scattering process. Besides, these defects are indicative of disorder, or lattice deformation caused by dopants, or vacancies [41]. Moreover, *D* and *G* bands were seen to have emerged with humps between 1400-1600 cm^{-1}, resulting from the implantation of C in WS_2 generating an immiscible WS_2-WC structure (Fig. 5.11 (a)). The figure clearly shows the emergence of the *D*- and *G*-bands at an ion fluence of above 1×10^{15} ions/cm^2. However, the intensity of the *D* and *G* bands displays site-specific variations, independent of the chosen ion fluences. These results confirm the presence of WC content and substantiate the phase analysis of WC derived from the XRD analysis shown in Fig. 5.10 (c). Furthermore, the bands associated with WC stretching modes were positioned at around 696 cm^{-1} and 807 cm^{-1} in the case of highest fluence, i.e., 1×10^{16} ions/cm^2 (Fig. 5.11 (b)) [42]. The dangling bond to be realized at the chalcogen vacancy site is expected to facilitate the bonding of W-C. As previously mentioned, the

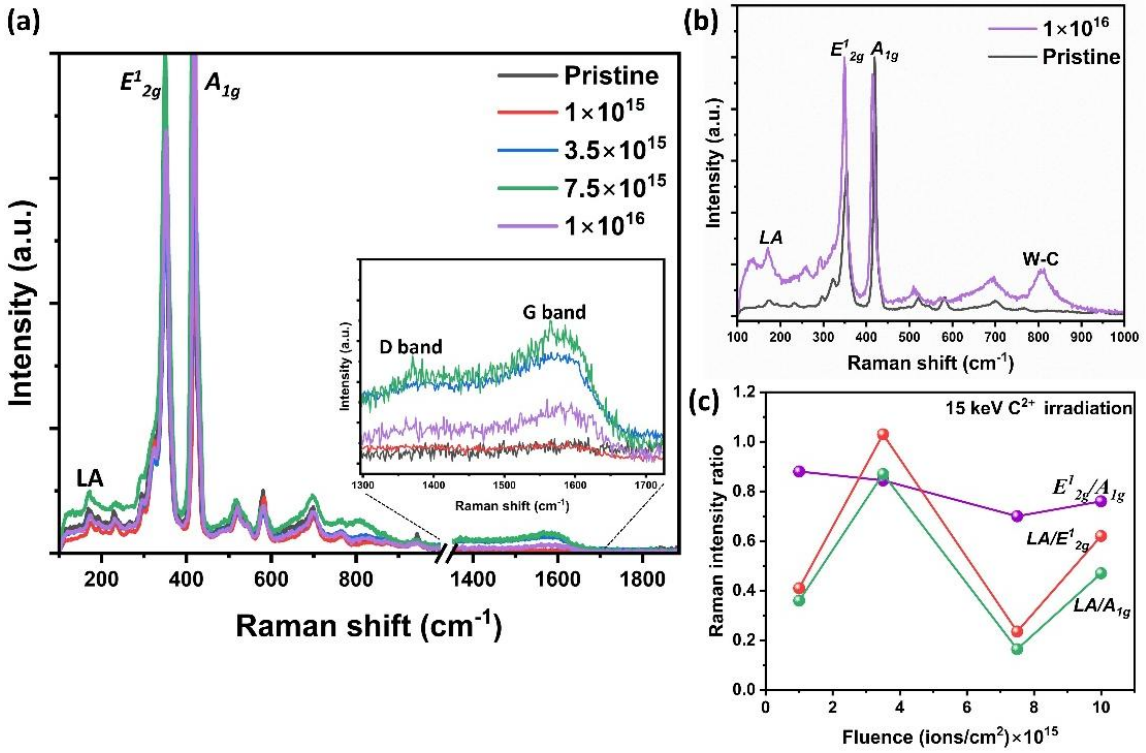

Figure 5.11: (a) Raman spectra of pristine (exfoliated WS_2) and after irradiation for fluences 1×10^{15}, 3.5×10^{15}, 7.5×10^{15}, and 1×10^{16} ions/cm^2, (b) plot for pristine WS_2 and after irradiation at fluence 1×10^{16} ions/cm^2 to show the presence of bands related to W-C, (c) Intensity ratios vs. fluence plot acquired from the Raman spectra.

defect density can be estimated from the intensity ratios of the *LA* mode to the first-order E^1_{2g} and A_{1g} Raman active peaks. The normalized intensity ratios for E^1_{2g} to A_{1g}, *LA* to E^1_{2g}, and *LA* to A_{1g} modes, respectively, are plotted against fluences and shown in Fig. 5.11 (c). The plot with intensity ratios of *LA(M)* to first-order phonon modes predicts an optimal disorder in the system irradiated at a fluence of 3.5×10^{15} ions/cm^2. But the intensity ratio dropped at a particular fluence of 7.5×10^{15} ions/cm^2. We speculate that, taking advantage of competitive S_e and S_n values, C will replace the sites of S atoms locally and would bond with W, forming isolated WC. A clear indication of D and G bands can also be found at fluence, 7.5×10^{15} ions/cm^2. Nevertheless, there is an upsurge in the intensity ratio at the highest fluence of 1×10^{16} ions/cm^2. In addition, the E^1_{2g}/A_{1g} ratio attains a maximal value at the lowest fluence. However, as we moved towards higher fluences, it progressively declined due to the abrupt removal of W or S atoms caused by ion bombardment, with S vacancies being more noticeable.

5.4.3 Elemental composition and morphological study

5.4.3.1 Energy dispersive X-Ray spectra and elemental mapping analysis

The EDX spectra of the pristine and the irradiated specimens after 15 keV C^{2+} irradiation are shown in Fig. 5.12 (a-d), along with the weight % as well as the atomic % of tungsten (W), sulfur (S) and carbon (C) elements, respectively. The elemental mapping of pristine and C^{2+} irradiated WS_2 (a fluence of 7.5×10^{15} ions/cm^2) are shown in Fig. 5.13 and Fig. 5.14 (a-d), respectively. The elemental mapping of the pristine sample, as shown in Fig. 5.13 (a-d), reveals the presence of W, S, and a small amount of C. The trace amount of carbon is likely due to contamination from the environment or the use of carbon tape for casting samples on the grid. After irradiation at an ion fluence of 7.5×10^{15} ions/cm^2, the elemental mapping shows a noticeable increase in carbon content, along with the persistent detection of W and S atoms (Fig. 5.14 (b-d)). The presence of tungsten (W) and sulfur (S) peaks with a strong signal along with a weak signal of C in the lower energy spectrum can also be found from the EDX spectra for 15 keV C^{2+} irradiated WS_2 system at the highest fluence (Fig. 5.14 (e)). At high fluence, i.e., 1×10^{16} ions/cm^2, the percentage of carbon incorporated in WS_2 at the projectile range was maximum and estimated to be 52.28 % at

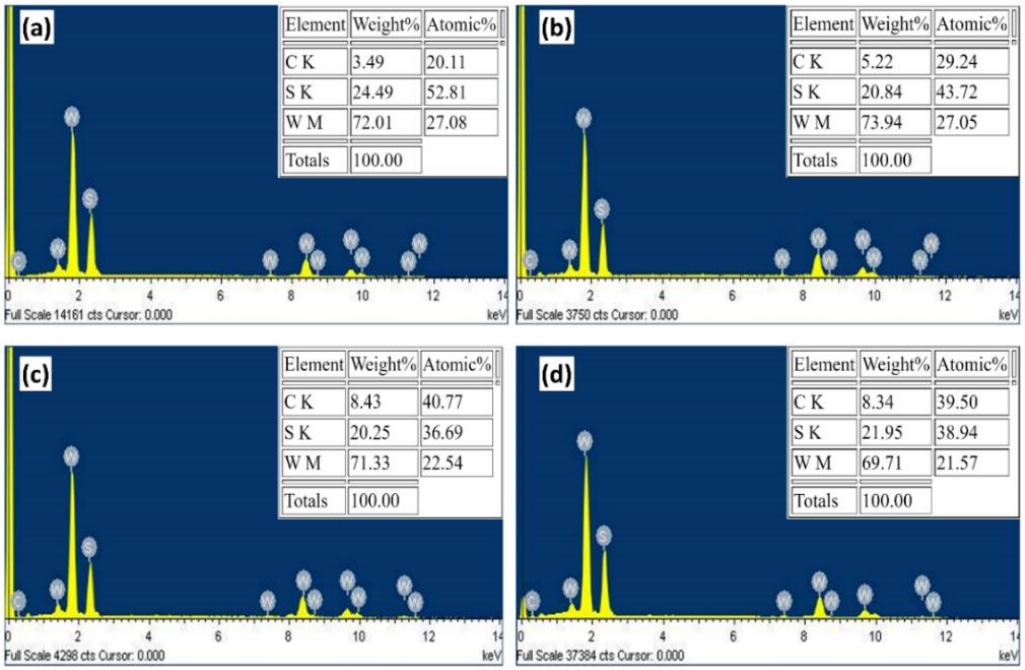

Figure 5.12: EDX spectra of (a) pristine, and irradiated WS_2 with 15 keV C^{2+} irradiation at fluences (b) 1×10^{15} (c) 3.5×10^{15}, and (d) 7.5×10^{15} ions/cm^2, respectively.

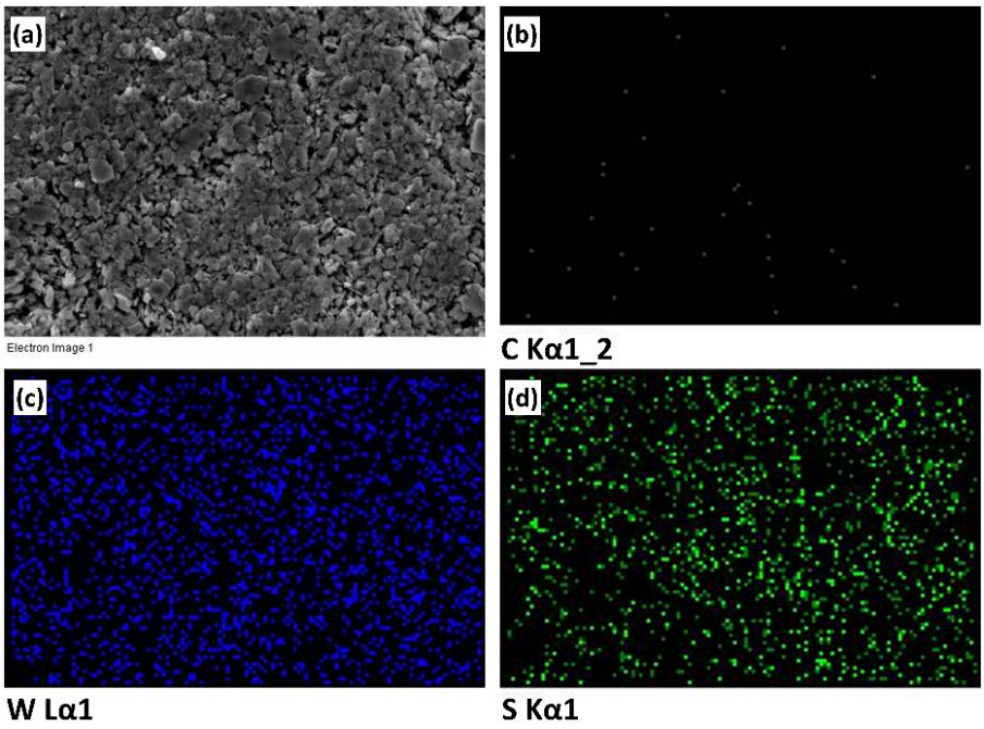

Figure 5.13: Elemental mapping of un-irradiated (pristine) WS_2 (a) SEM image, (b) Carbon (C), (c) tungsten (W), and (d) sulfur (S) elements are shown.

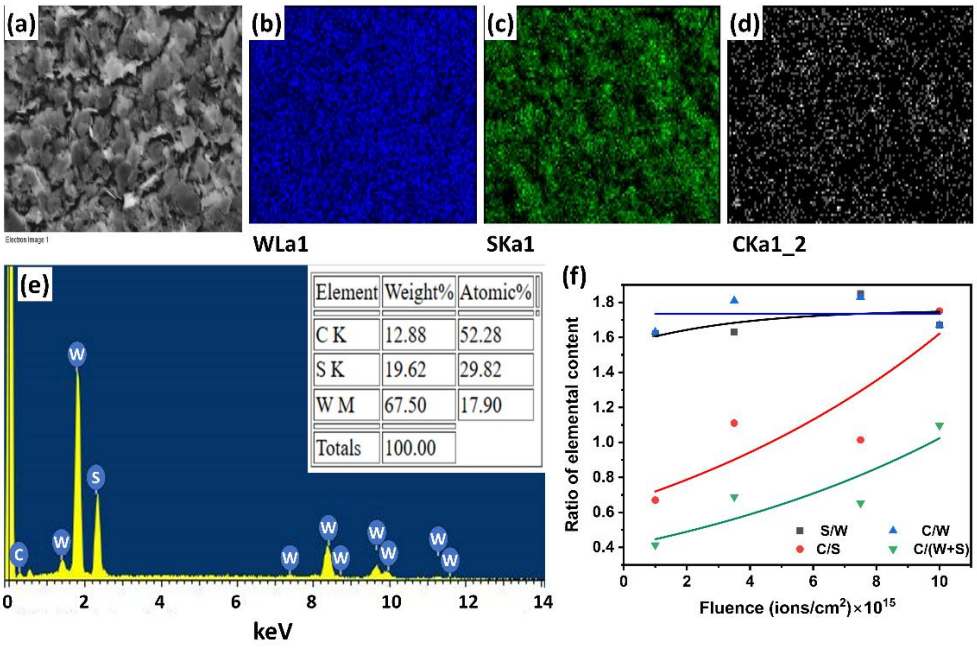

Figure 5.14: Elemental mapping of 15 keV C^{2+} after irradiation at fluence 7.5×10^{15} ions/cm^2 (a) SEM image, and elemental mapping corresponding to (b) tungsten (W), (c) sulphur (S), and (d) carbon (C) elements; (e) EDX spectrum of irradiated WS_2 at the highest fluence of 1×10^{16} ions/cm^2, (f) content of S/W, C/S, C/W, C/(W+S) ratio *vs*. fluence showing the incorporation of C and sulphur deficiency in the material after ion irradiation.

a designated site. The mapping was done for this fluence as it would create maximum S vacancies [43], as revealed from the SRIM plot (Fig. 5.9 (d)). Subsequently, the S/W, C/S, C/W and C/(W+S) ratios were calculated and plotted in Fig. 5.14 (f). While C/W maintains a relatively steady pattern, C/S and C/(W+S) showed an increasing trend with an increase in C^{2+} ion flux. We speculate that the intrusion of C into the WS_2 lattice would occur against the disruption of W-S bonds, thereby creating chalcogen vacancies. Removal of S vacancies, substantiated by C ions, can be responsible for the development of the immiscible WC phase locally. Given the lattice parameter of WC is much shorter than that of the *2*H-WS_2 phase, this would contract the lattice at the site of phase transformation.

5.4.3.2 Morphological analysis

AFM imaging illustrates the surface morphology of pristine and 15 keV C^{2+} irradiated WS_2 systems (Fig. 5.15 (a-f)). The 2D surface scans at selected locations and 3D topographies of the systems under study were used to analyze surface topology and texture parameters. Surface topography is characterised by irregularly packed heterogeneous features, lumped and clustered with fragmented sheets, resulting in significant variations in height with

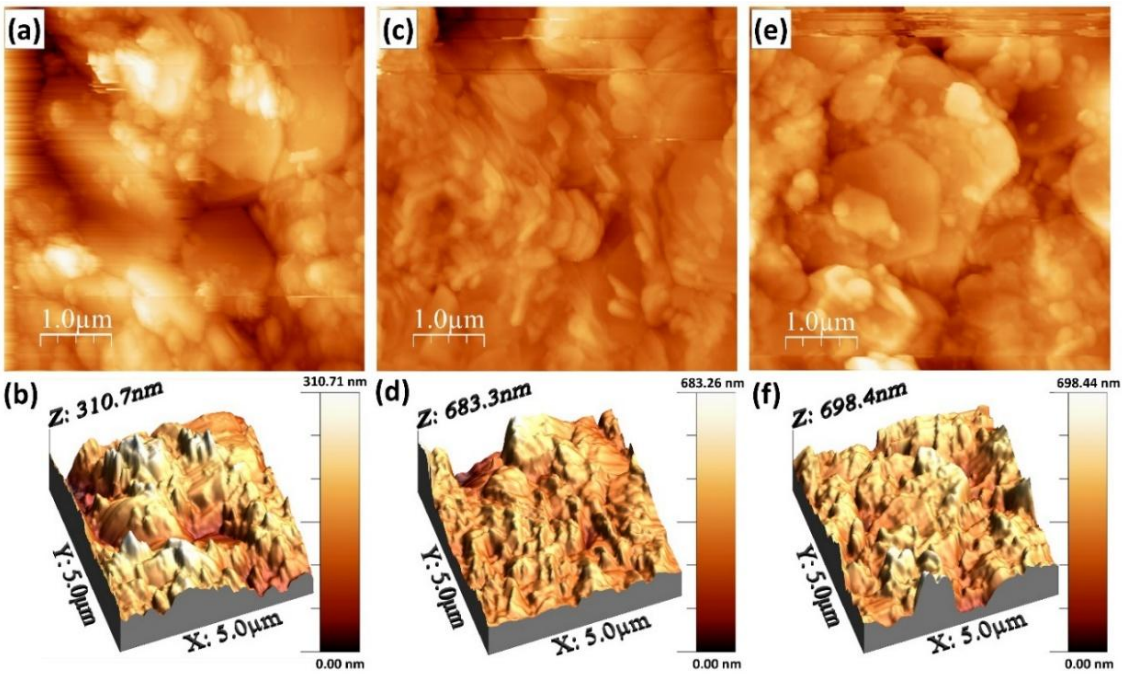

Figure 5.15: AFM images of 2D surface scans of (a) pristine (exfoliated WS_2) and after irradiation for fluence (c) 1×10^{15}, and (e) 1×10^{16} ions/cm^2; (b,d,f) are the corresponding 3D topography, respectively.

irradiation. The RMS roughness varied from ~32.3 nm in the case of the pristine system (before irradiation) to ~67.6 nm and ~81.9 nm at fluences of 1×10^{15} and 1×10^{16} ions/cm^2, respectively. The irregular holes, ditches, and trenches witnessed in the micrographs are supposed to augment the RMS roughness. Thus, differences in surface roughness from the pristine case can be attributed to the variations in the material surface after irradiation at a given fluence. Furthermore, the sputtering effect due to irradiation must be considered, which results in de-atomization and distortion in the target material.

TEM analysis was carried out to investigate the morphological changes of the irradiated WS_2 at higher fluences ranging from 3.5×10^{15} to 1×10^{16} ions/cm^2, shown in Fig. 5.16 and Fig. 5.17 (a-d). The morphology displays layered sheets of WS_2 (Fig. 5.16 (a)) with *d*-spacing values ~0.59 nm and ~0.28 nm belonging to (002) and (100) planes, respectively, in the case of pristine WS_2 (Fig. 5.16 (b)). However, TEM imaging at the highest fluence depicts incorporation of C-dots through implantation with 15 keV C^{2+} ion irradiation. The average diameters of C-dots formed varied from ~2 nm to 7 nm (Fig. 5.16

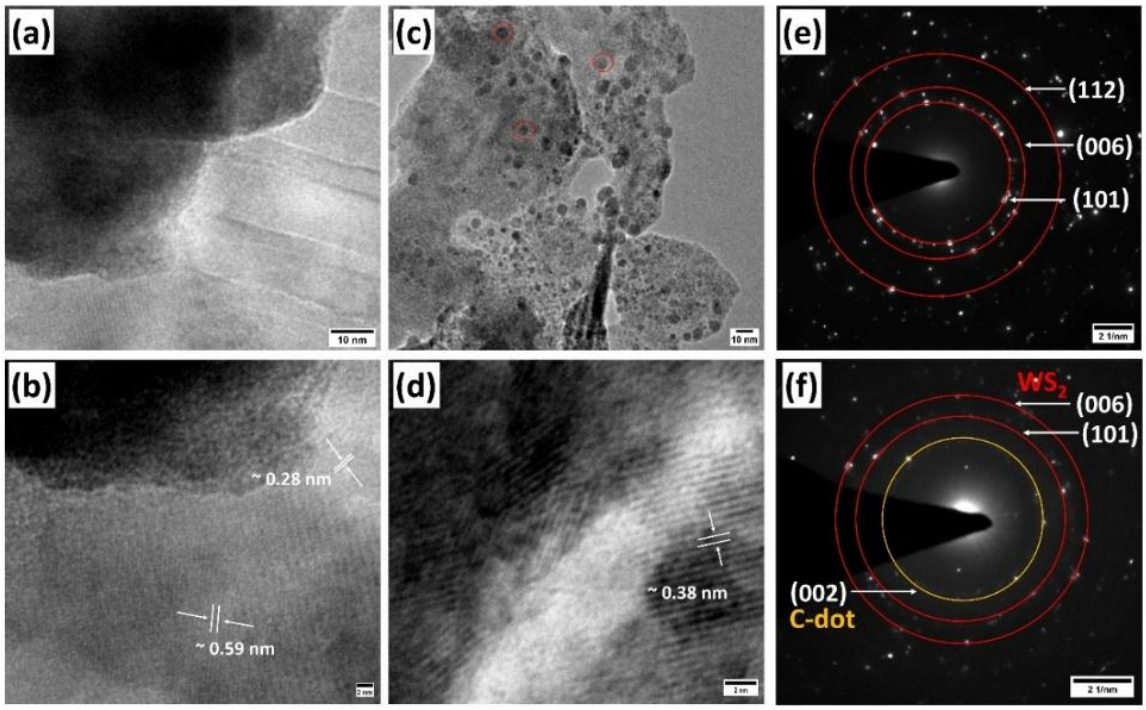

Figure 5.16: HR-TEM images of (a,b) pristine WS_2, (c,d) 15 keV C^{2+} irradiated WS_2 at a fluence of 1×10^{16} ions/cm^2, with the scale bars 10 nm and 2 nm for (a,c) and (b,d) cases, respectively. (e,f) SAED patterns of the pristine and irradiated cases. Note the central ring in (f) is attributed to the (002) plane of the graphitic C-dot.

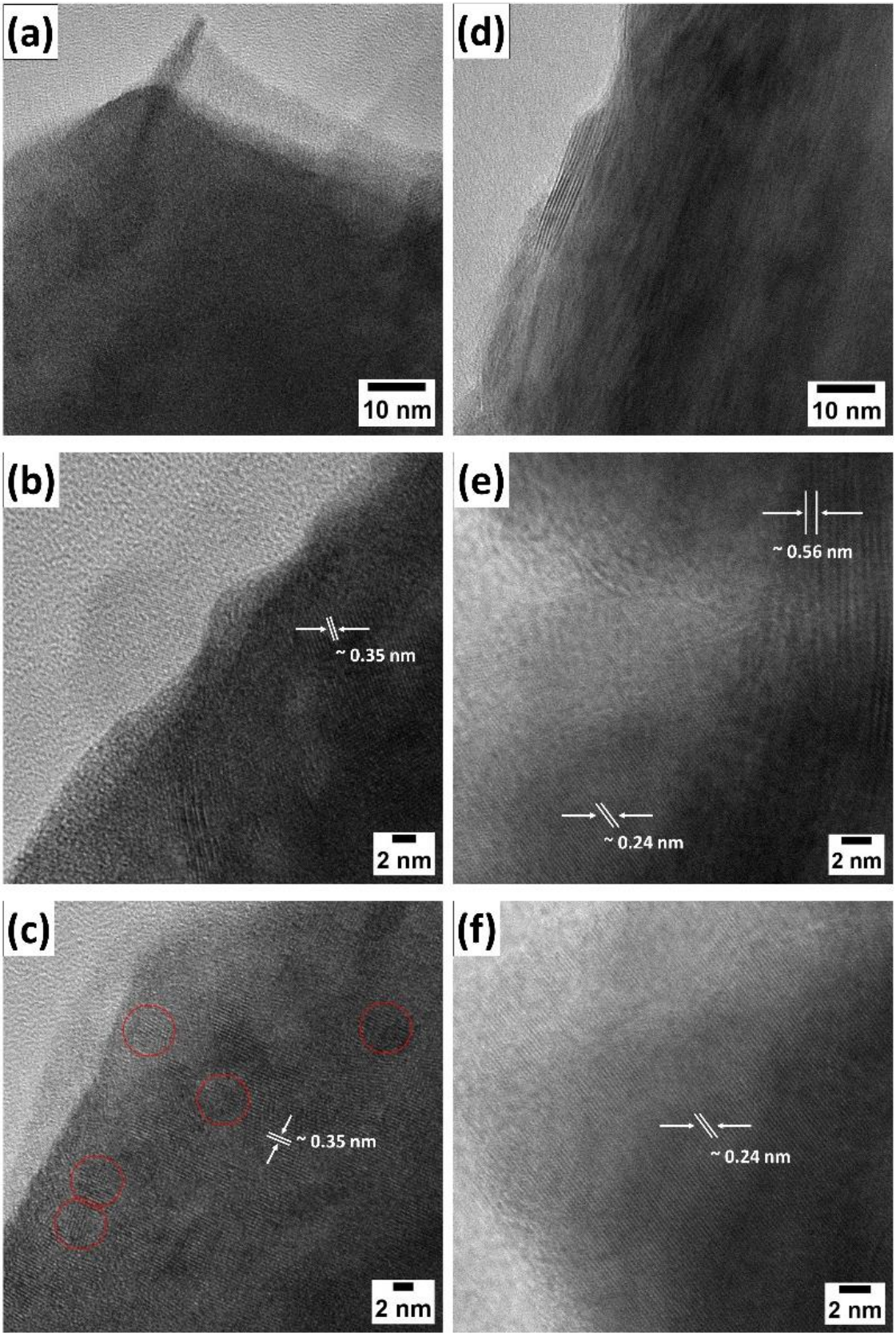

Figure 5.17: HR-TEM images of 15 keV C^{2+} irradiated WS_2 at a fluence of (a-c) 3.5×10^{15} ions/cm^2, and (d-f) 7.5×10^{15} ions/cm^2. Note: Scale bars are 10 nm and 2 nm, respectively.

(c)). At a fluence of 1×10^{16} ions/cm^2, the lattice fringe observed was due to the developed C-dots. This fringe was estimated to have a *d*-spacing of ~0.38 nm, matching the *d*-spacing value of the (002) plane of graphitic C-dots that would typically occur after the C^{2+} ion impact (Fig. 5.16 (d)) [44,45]. The SAED analysis of both pristine and irradiated samples at the highest fluence offers bright spots with circular patterns illustrating polycrystalline arrangements of the crystals (Fig. 5.16 (e,f)). The planes (101), (006), and (112) indexed in the SAED pattern of the pristine specimen belong to the WS_2 crystal structure. Whereas the newly emerged (002) plane is attributed to the formation of graphitic C-dots, as indicated by the SAED pattern observed at an ion fluence of 1×10^{16} ions/cm^2, as shown in Fig. 5.16 (f) [46].

The TEM analysis for mid-fluences reveals interplanar spacings corresponding to localized WC and C-dots due to C ion irradiation, along with the noticeable (002) plane of the WS_2 system. At a mid-fluence of 3.5×10^{15} ions/cm^2, an interplanar spacing of ~0.35 nm is identified, corresponding to the (002) plane of the C-dot formation, which emerged due to C^{2+} ion bombardment (Fig. 5.17 (b,c)). Moreover, at an ion fluence of 7.5×10^{15} ions/cm^2, the interplanar spacing of around 0.24 nm corresponds to the (100) plane, indicating WC formation, as depicted in Fig. 5.17 (e,f). Furthermore, a *d*-spacing value of ~0.56 nm is also observed, associated with the (002) plane of the pristine WS_2 structure.

5.4.4 Computational study of C-incorporated WS_2 systems

5.4.4.1. Computational details

The spin-polarized calculations were carried out using density functional theory (DFT) based on plane-wave pseudopotential, as implemented in the PWSCF code of the Quantum Espresso software package. To deal with the exchange-correlation functional, the generalized gradient approximation with Perdew-Burke-Ernzerhof parameterization (GGA-PBE) was utilized. The wavefunction kinetic energy cutoff (ecutwfc) and charge density cutoff (ecutrho) have been adjusted to 50 Ry/680 eV and 300 Ry/4082 eV, respectively. Furthermore, throughout the computations, the scalar-relativistic Optimized Norm-Conserving Vanderbilt Pseudopotential (ONCVPSP) represents the electron-ion interaction. A 3×3×1 supercell of WS_2 with a doped C atom and a S vacancy is modelled for the nudged elastic band (NEB) calculation. Prior to the calculation of migration energies, the initial and final images were completely optimized to the ground state energy level. The images for intermediate stages can be found in the *Appendix* in Fig. A8.

To model the bilayer WS_2 system, 2×2×1 super cell comprising 8 metal atoms and 16 chalcogen atoms was taken into consideration. To study the defected bilayer, C atoms as dopants were introduced, replacing the S atoms. Chalcogen vacancies (V_s) were introduced by simply removing the S atoms from the layer. Using the Monkhorst Pack method, the reciprocal space of the first Brillouin Zone (BZ) was partitioned into a 5×5×1 mesh of *k*-points. Relaxation of cell parameters and atomic locations is permitted until an energy convergence of 10^{-6} Ry and a force convergence of 10^{-4} Ry/Bohr is achieved. To obtain the electronic properties, a dense *k*-grid of 10×10×1 was taken into consideration.

5.4.4.2 Migration barrier energy

Low-energy ion irradiation techniques inevitably lead to the formation of point defects, particularly vacancies, in 2D materials [47]. Among these, chalcogen vacancies, especially sulfur (S) vacancies in WS_2, are of particular interest due to their relatively lower threshold formation energy [48]. Additionally, the presence of the *LA* (*M*) mode in the Raman spectra of exfoliated WS_2 suggests the formation of substantial point defects, primarily S vacancies, as a result of ion irradiation. To further understand this phenomenon, a first-principles study was conducted to calculate the vacancy formation energy for sulfur in WS_2, which was found to be ~6.08 eV, consistent with previously reported values [49]. In contrast, the formation energy required to create a tungsten (W) vacancy was significantly

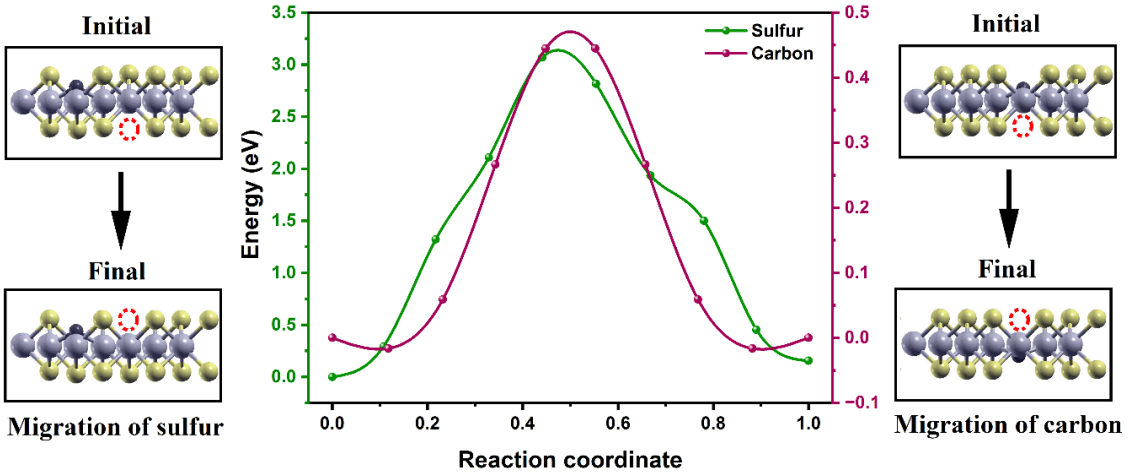

Figure 5.18: Migration barrier of sulfur and carbon in WS_2. The purple, yellow and black balls indicate tungsten (W), sulfur (S), and carbon (C) atoms, respectively and red dotted balls depict sulfur vacancy.

higher by 14.47 eV. Due to the remarkably low vacancy formation energy of S, it was believed that WS_2 is highly susceptible to ensuring S vacancies under ion irradiation. Furthermore, the creation of chalcogen vacancies due to incident projectile ions, particularly through irradiation, is well established. During ion irradiation, where carbon (C) ions serve as projectile and S atoms are displaced from the WS_2 lattice, there is a high probability that nearby vacant sites may be occupied by both C and S atoms. This makes it essential to investigate the migration barriers of both sulfur and implanted carbon atoms, as their diffusion behaviour plays a crucial role in the irradiation process. To study this, a 3×3 supercell of a WS_2 monolayer was considered, featuring a doped C atom and S vacancy. The activation energy for vacancy migration was found to be around 0.44 eV for

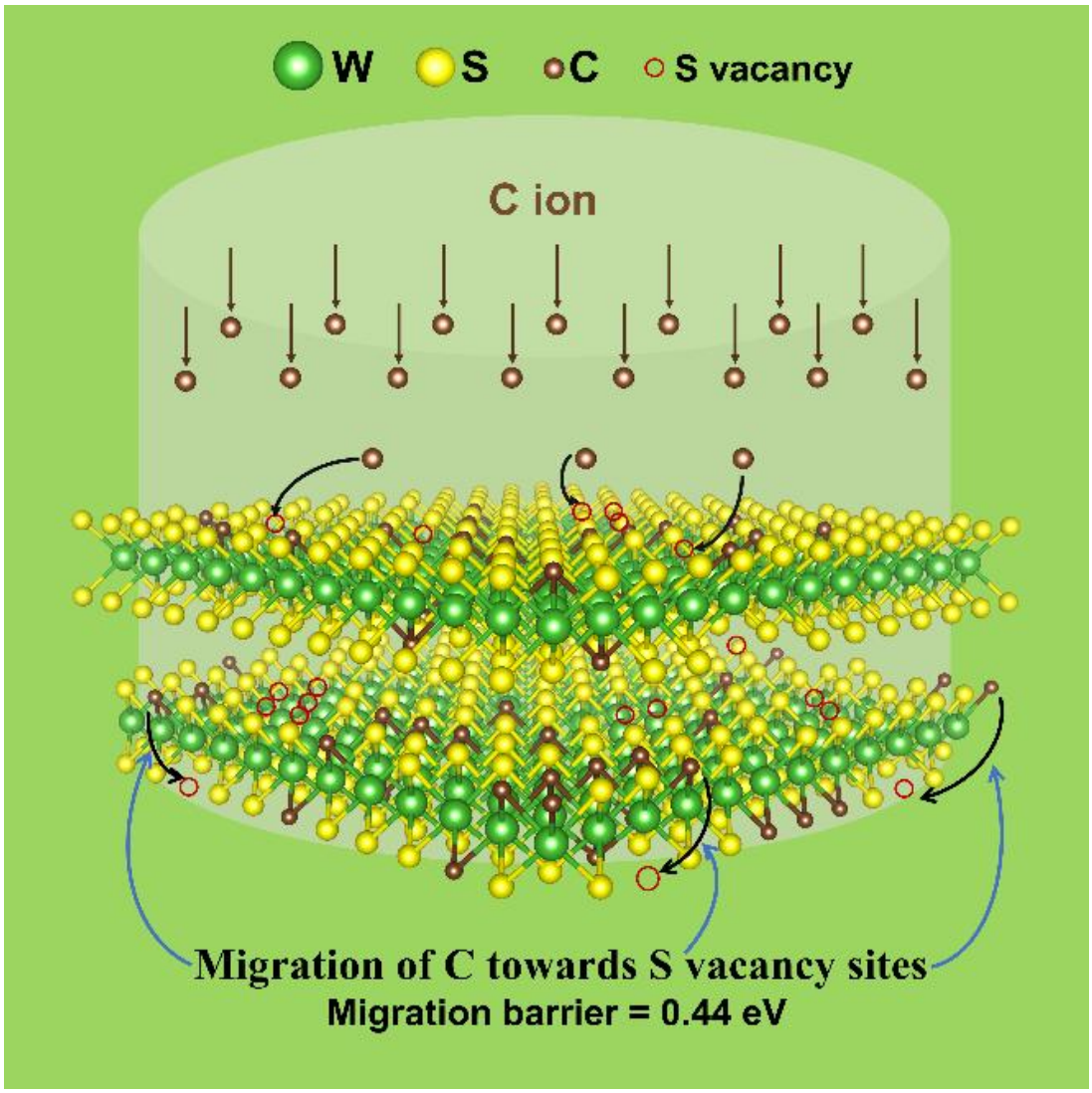

Figure 5.19: Schematic representation of migration of C atoms towards vacant S sites.

C and 3.07 eV for S (Fig. 5.18). Due to its lowered migration barrier, implanted C atoms are more likely to diffuse into the WS_2 lattice, potentially leading to the localized formation of the WC phase. The schematic in Fig. 5.19 illustrates the migration of C atoms toward S vacancy sites in WS_2 layers.

5.4.4.3 Structural and electronic properties

Subsequently, the modification of the electronic band gap with different concentrations of dopants (C) and vacancies (S) has been studied. In this regard, a 2×2 supercell of the bilayer WS_2 system was taken considering these point defects independently, including their co-existence (Fig. 5.20 (a-h)). The electronic nature and the defect percentage of these systems are listed in Table 5.5. In contrast to monolayer WS_2, the bilayer one is an indirect band gap material, with its valence band maxima (VBM) and conduction band minima (CBM) lying at the *Γ*-point and *K*-point of the Brillouin zone (BZ), respectively [50,51]. In agreement with the reports, its indirect band gap is calculated to be ~1.46 eV, and the

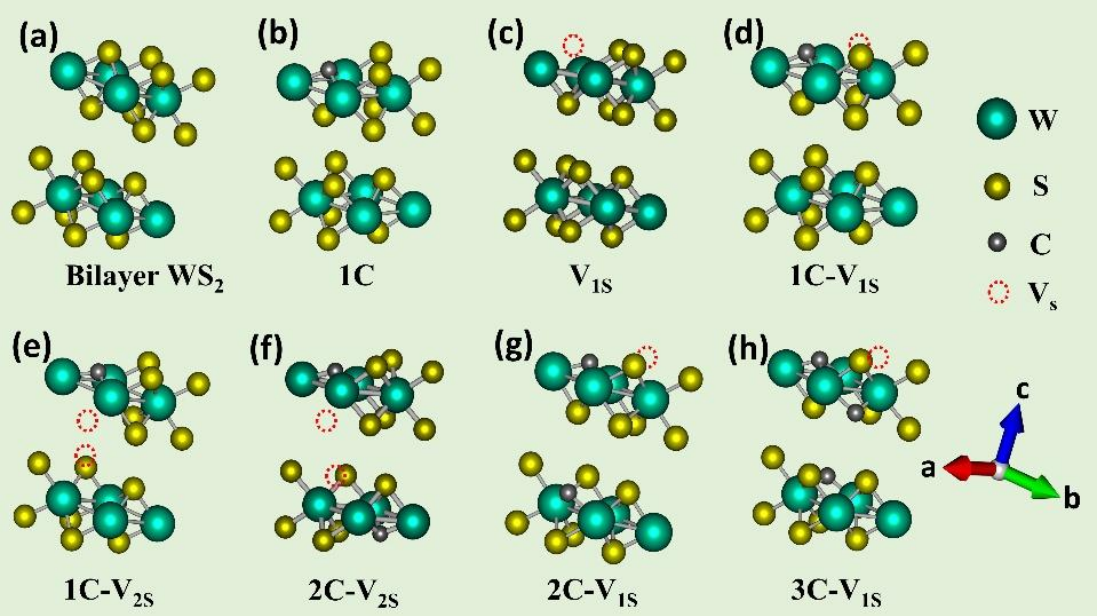

Figure 5.20: Optimized geometrical structures of (a) bilayer WS_2, (b) one C atom substituting S atom, (c) one S vacancy, (d) one C doped along with one S vacancy, (e) one C doped along with two S vacancies, (f) two C doped along with two S vacancies, (g) two C doped along with one S vacancy, and (h) three C doped along with one S vacancy. The red arrow in the bottom right points towards the *x*-direction, the green arrow towards the *y*-direction, and the blue one corresponds to the *z*-direction.

direct gap at *K* point has a band energy difference of ~1.76 eV (Fig. 5.21 (a,d)) [52]. Typically, the W-S bond length is ~2.42 Å [53]. In the WS_2 (1C) system with one doped C and without having a vacancy, the C atom moves closer to the metal atom with a bond length of 2.03 Å (Fig. 5.20 (b)). The shrinking of the W-C bond length is due to the smaller atomic radii of the C atom as compared to S (also note the lattice parameter of WC (a=b=2.94 Å), which is less than that of WS_2 (a=b=3.19 Å). From the band structure, the lowest conduction band in the system drops to 0.013 eV above the Fermi level, reducing the electronic band gap to ~0.27 eV at the *K*-point of the BZ (Fig. 5.21 (b)). This defect band is highly localised at the W (*d*), S (*p*), and C (*s, p*) orbitals (Fig. 5.21 (e)). When a single vacancy is added into the system, the S atoms settle vertically opposite (along the *z*-direction) to the vacant site, shifting near the middle metal atomic layer, occupying the available free space in the structure (Fig. 5.20 (c)). The W-S bond length near the vacant site is ~2.38 Å. The defect state in the conduction band in this case also has its band minima at the *K*-point but ~0.21 eV away from the Fermi level as compared to the WS_2 (1C) system (Fig. 5.21 (c)). This defect state is mostly contributed by the W (*d*), and S (*p*) orbitals (Fig. 5.21 (f)). The WS_2 (V_{1S}) system with one sulfur vacancy retains the indirect electronic nature of its pristine counterpart with a band gap of ~0.68 eV lying along the *Γ*-*K* direction. The direct band gap (~0.97 eV) of this system lies at the *K*-point. Thus, the presence of a C atom can bring a profound change to the electronic structure of the bilayer WS_2, whereas the presence of S vacancies can alter the energy difference between the VB and CB without causing much change to the band alignment along the high symmetric path (*Γ*-*M*-*K*-*Γ*). Even with the substitution of vacant sites by C ions in the system, some sites would remain unoccupied in the host lattice.

Considering the simultaneous existence of both C atoms and S vacancies, five additional bilayer WS_2 systems were modelled with varying defect densities. The systems are (i) one doped C atom with one S vacancy (1C-V_{1S}), (ii) one doped C atom with two S vacancies (1C-V_{2S}), (iii) two doped C atoms with two S vacancy (2C-V_{2S}), (iv) two doped C atoms with one S vacancies (2C-V_{1S}), (v) three doped C atoms with one S vacancy (3C-V_{1S}). The very first system with the coexistence of defects in this study (1C-V_{1S}) shows a transformation of the semiconducting nature of bilayer WS_2 to a semi-metallic one (Fig. 5.20 (d) and Fig. 5.22 (a,f)). Like pristine WS_2, the VBM of WS_2 (1C-V_{1S}) remains at the *Γ*-point but raises to the vicinity of the Fermi level. The CBM in this system undergoes significant changes as it moves from the *K*-point to the *M*-point and crosses the Fermi level

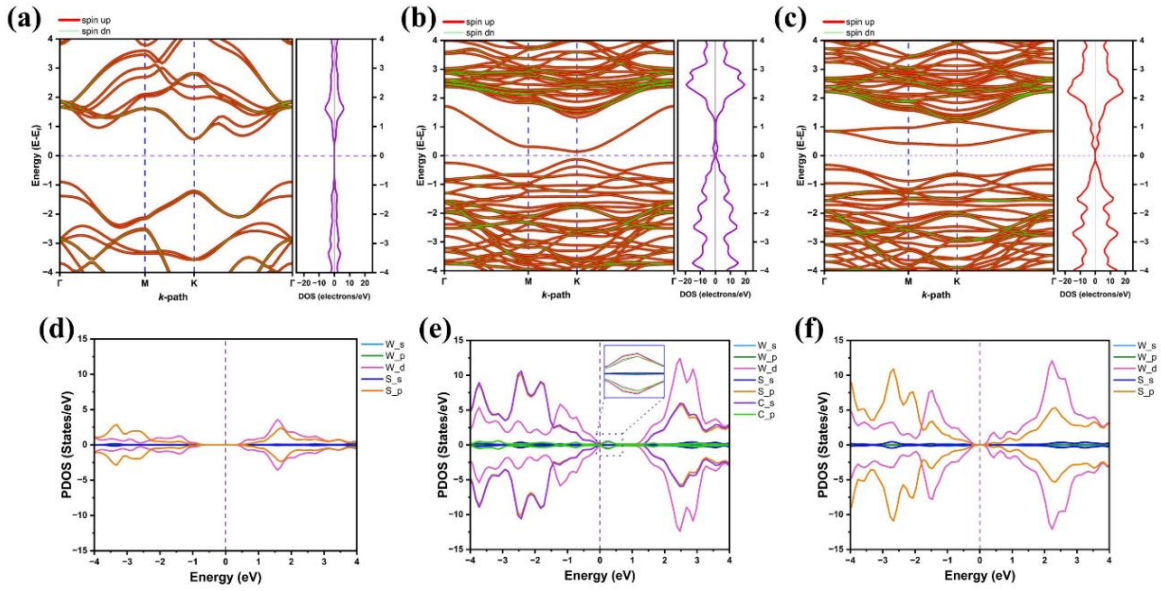

Figure 5.21: Electronic band structure of (a) bilayer WS_2, (b) single C doped WS_2 (1C), (c) single S vacancy WS_2 (V_{1S}), along with their respective (d,e,f) PDOS plots.

Table 5.5. Nature of the band gap engineering and electronic state due to the combinatorial defects in the host WS_2.

Sl. No.	Structural configuration	Doped C	S vacancy	Band gap Indirect (direct)	Nature	Defect %
1	Bilayer	---	---	1.46 (1.76) eV	Indirect semiconductor	0
2	1C	1	---	0.39 (0.27) eV	Direct semiconductor	4.1
3	V_{1S}	---	1	0.68 (0.97) eV	Indirect semiconductor	4.1
4	1C-V_{1S}	1	1	---	Semi-metallic	8.33
5	1C-V_{2S}	1	2	0.66 (0.39) eV	Direct semiconductor	12.5
6	2C-V_{1S}	2	1	---	Semi-metallic	12.5
7	2C-V_{2S}	2	2	0.05 eV	Semi-metallic	16.67
8	3C-V_{1S}	3	1	0.07 eV	Semi-metallic	16.67

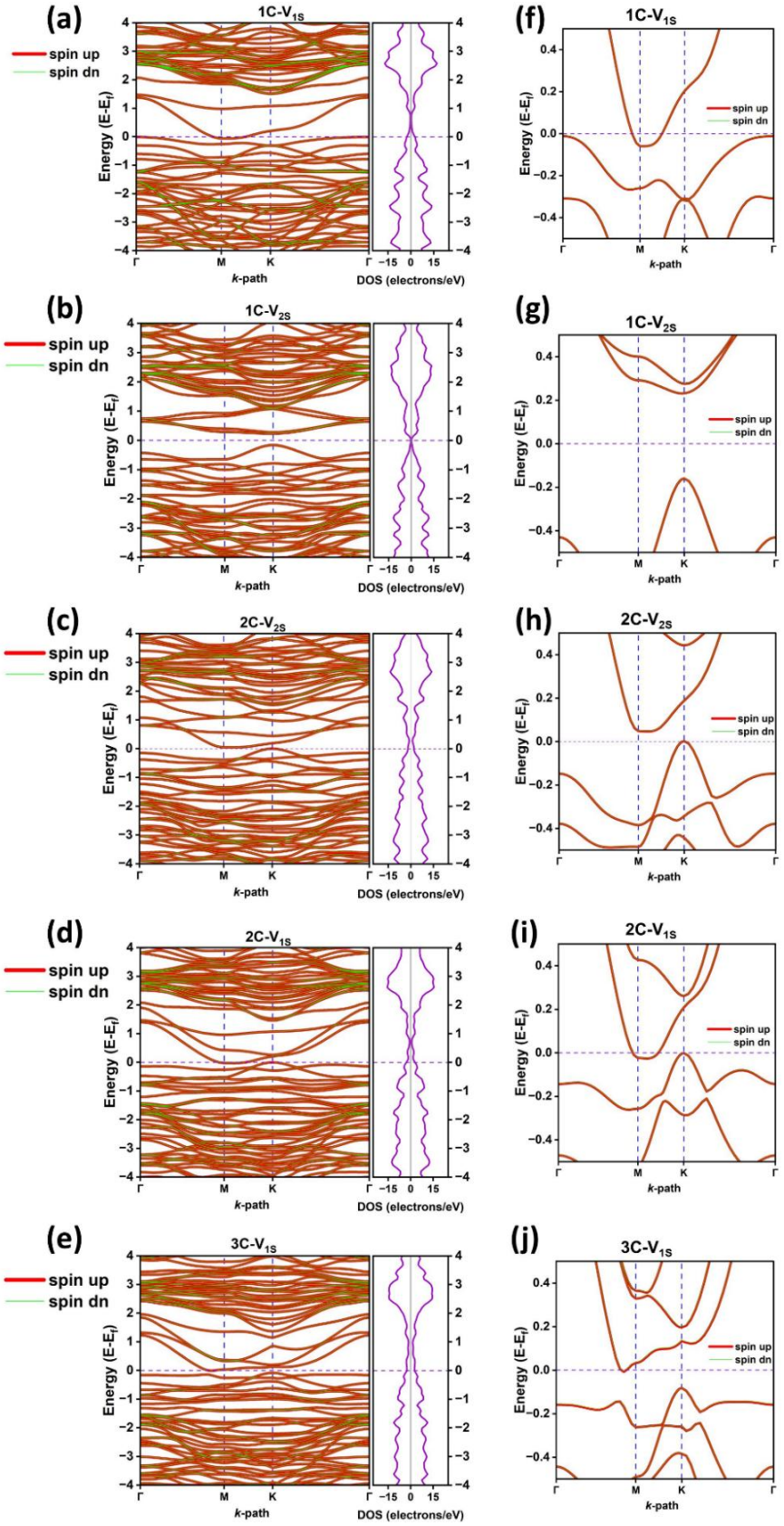

Figure 5.22: Band structure of (a,f) 1C-V_{1S} WS_2, (b,g) 1C-V_{2S} WS_2, (c,h) 2C-V_{2S} WS_2, and (d,i) 2C-V_{1S} WS_2, (e,j) 3C-V_{1S} WS_2. The plots from (f-j) are zoomed-in images of the band structures shown from (a-e), respectively.

(shown in Fig. 5.22 (f)). This simultaneous presence of an equal number of C dopant and S vacancy makes the material an electronically gapless semimetal. Next, the structure WS_2 (1C-V_{2S}) was investigated by increasing the number of S vacancies by one from the previous structure to check the sustainability of the semi-metallic nature of 1C-V_{1S} (Fig. 5.20 (e)). With a greater number of S vacancies in co-existence with C as a dopant atom, the bilayer system becomes a direct semiconductor at the *K*-point with a bandgap of ~0.39 eV, losing the semi-metallic nature of 1C-V_{1S} (Fig. 5.22 (b,g)). Subsequently, we examine the electronic structure by adding one more C atom to WS_2 (1C-V_{2S}). As the number of C dopants and S vacancies becomes equivalent, the 2C-V_{2S} system behaves almost as a semi-metallic material with a near-zero band gap of ~0.05 eV at the vicinity of the Fermi level (Fig. 5.22 (c,h)). Analogous to the band structure of 1C-V_{2S}, the VBM of 2C-V_{2S} remains at the *K*-point. However, the inclusion of the C atom shifts the CBM to the *M*-point from the *K*-point. To verify this semi-metallic nature, two more structures of bilayer WS_2 were studied with two doped C and one S vacancy (2C-V_{1S}) and three doped C atoms with one S vacancy (3C-V_{1S}) (Fig. 5.20 (g,h)). For 2C-V_{1S}, the VBM is found at the *K*-point and the CBM is at the *M*-point (Fig. 5.22 (d,i)). The Fermi level in this case crosses both the lowest conduction band and the highest valence band, creating a perfect gapless semimetal. As we increase the C dopant in 3C-V_{1S}, the CBM sees a shift away from the *M*-point towards

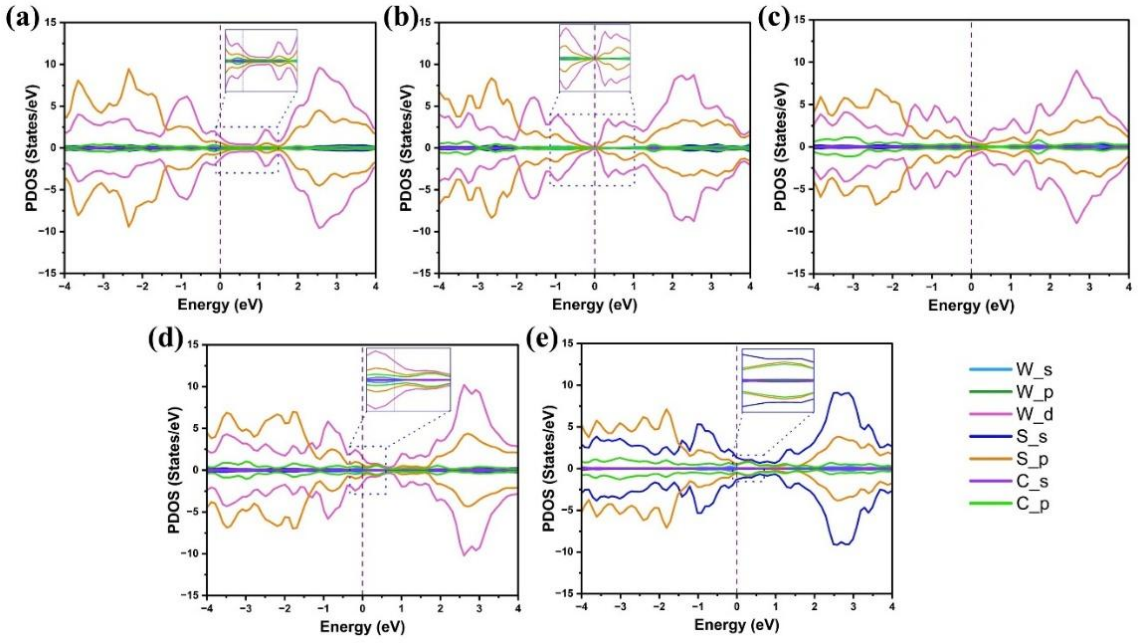

Figure 5.23: PDOS of (a) 1C-V_{1S}, (b) 1C-V_{2S}, (c) 2C-V_{2S}, (d) 2C-V_{1S}, and (e) 3C-V_{1S} WS_2 systems.

the Γ-point but retains its semi-metallic nature with a low yet finite band gap of ~0.07 eV (Fig. 5.22 e,j)). Thus, it is evident that the material becomes electronically semi-metallic when half or more of the S vacant sites in WS_2 are substituted by the C atoms.

The origin of the defect states in the band structures can be understood through the projected density of states (PDOS) plots shown in Fig. 5.21 (d-f) and Fig. 5.23. As discussed earlier, the introduction of dopants and vacancies modifies the structural properties of the materials, such as bond lengths and angles, which subsequently influence the orbital interactions within the systems. Consequently, the defect states in all the systems predominantly arise from the net contributions of the outermost orbitals of the elements W (5*d*), S (3*p*), and C (2*p*). These altered orbital interactions adjust the band states in the CB and VB near the Fermi level, transforming the systems from semiconducting to semi-metallic ones.

5.5 Impact of 0.85 GeV U^{28+} ions on bulk and exfoliated WS_2 systems

5.5.1 SRIM analysis

SRIM calculations were performed in the GeV regime to analyse the stopping power *vs.* energy plot, ion trajectories from the depth *vs*. y-axis plot, uranium (U^{28+}) concentration, and vacancy distribution plots (Fig. 5.24). An energy *vs*. stopping power plot was generated to study the association between U^{28+} ions and the WS_2 (target) material. The results indicate that the dominant energy loss mechanism is electronic stopping (S_e), calculated to be approximately 50.78×10^2 eV/Å, while nuclear energy loss (S_n) remains significantly lower, and is around 14.67 eV/Å (Fig. 5.24 (a)). Furthermore, the projected range of the incident ion beam is estimated to be approximately 26.4 µm, with longitudinal and lateral straggling values of about 1.12 µm and 1.34 µm, respectively. The ion trajectories of U^{28+} ions impacting the WS_2 target are depicted in Fig. 5.24 (b). The U^{28+} concentration *vs.* target depth plot illustrates the affected region of the material, showing an impact depth of up to approximately 26.8 µm (Fig. 5.24 (c)). Notably, vacancy formation was most significant for sulfur (S) at the highest fluence (1×10^{11} ions/cm^2) with a target depth of about 26.4 µm (Fig. 5.24 (d)).

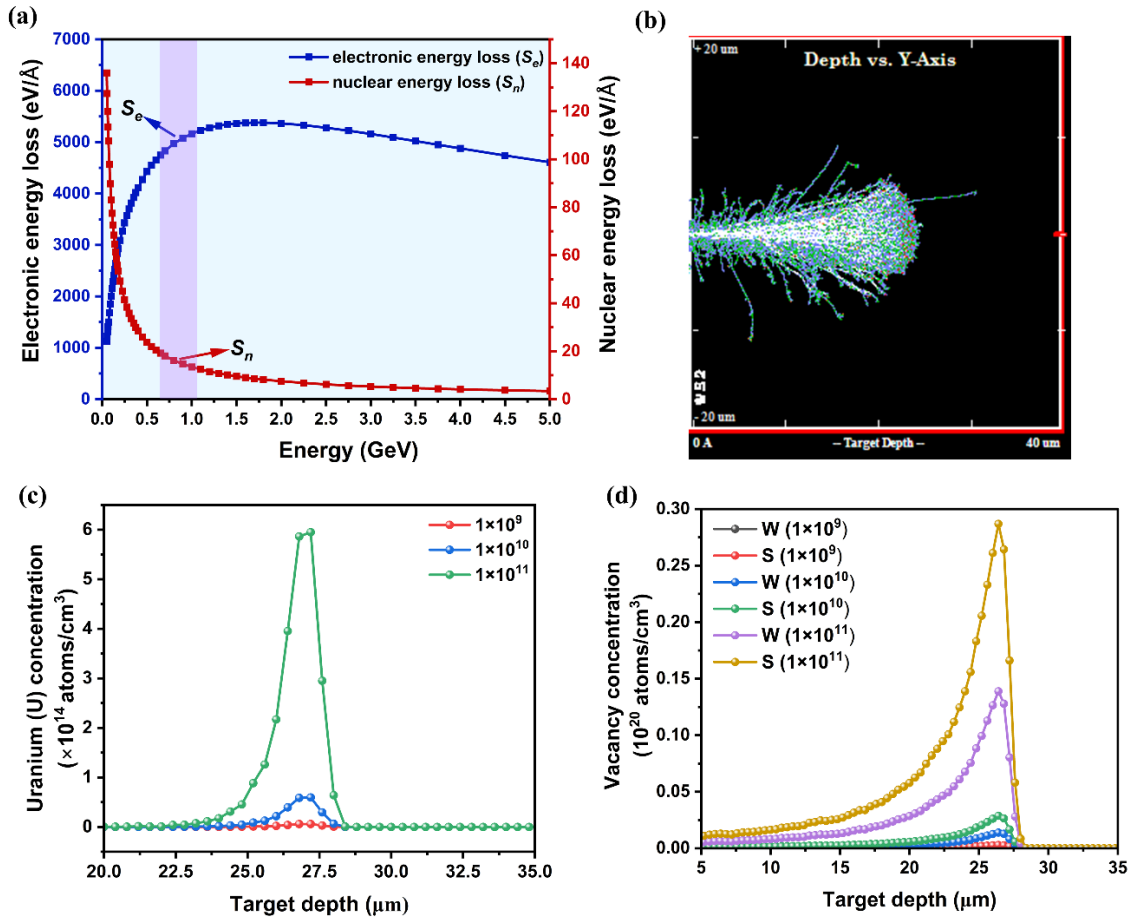

Figure 5.24: SRIM/TRIM simulations of 0.85 GeV U ions in WS_2, (a) stopping power *vs.* energy plot, (b) depth *vs.* y-axis plot, (c,d) uranium (U) and vacancy concentration plots for varied fluences.

5.5.2 Structural and vibrational analysis

The powder X-ray diffraction (XRD) patterns of bulk and exfoliated WS_2 systems exposed to 0.85 GeV U^{28+} ions with fluences ranging from 1×10^9-1×10^{11} ions/cm^2 were obtained using a *CuK*$_\alpha$ operating diffractometer source. The diffraction peaks were obtained in the Bragg's diffraction angles (2θ) ranging from ~10º-65º. The diffraction peaks in all the bulk and exfoliated cases are positioned at 2θ ~14.6º, 29.2º, 44.1º and 59.8º are (002), (004), (006), and (008), respectively, and were indexed to the hexagonal crystal structure of the WS_2 system depicted in Fig. 5.25 [54,55]. The most intense peak in the XRD patterns corresponds to the (002) plane and is oriented along the *c*-axis direction of the phase structure. There is a noticeable change in the lattice parameters and average crystallite size for the 0.85 GeV U^{28+} ion irradiated WS_2 systems (Table 5.6). The expansion and compression in the lattice parameters and anomalous variations in the calculated average

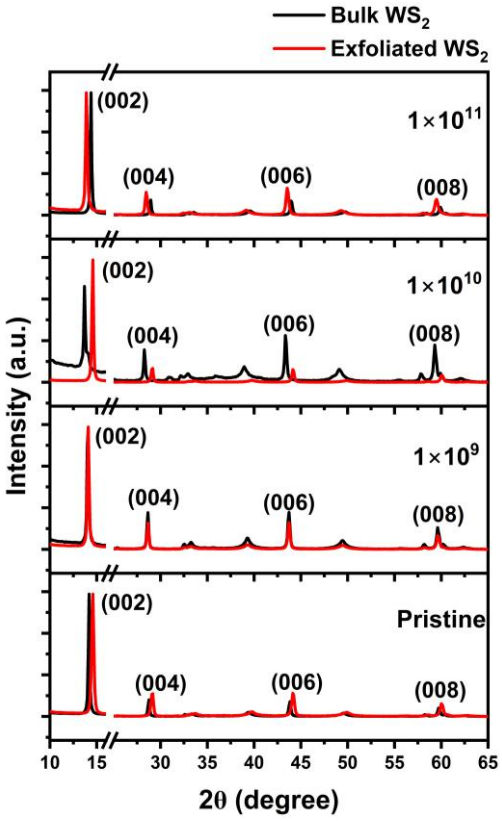

Figure 5.25: Powder XRD patterns of bulk and exfoliated WS_2 systems indexed to the hexagonal crystal structure of space group *P63/mmc*.

Table 5.6. Structural parameters obtained from powder-XRD analysis of bulk and exfoliated systems, subjected to 0.85 GeV U^{28+} ions.

Sl. No.	Sample (fluence in (ions/cm^2))	Lattice parameter along *c*-axis direction (Å)		Crystallite size, d_c in 'nm'	
		bulk WS_2	exfoliated WS_2	bulk WS_2	exfoliated WS_2
1	Pristine (0)	12.49	12.14	41.1	25.4
2	Irradiated (1×10^9)	12.58	12.55	33.2	31.1
3	Irradiated (1×10^{10})	12.90	12.14	43.6	36.8
4	Irradiated (1×10^{11})	12.31	12.72	38.8	29.7

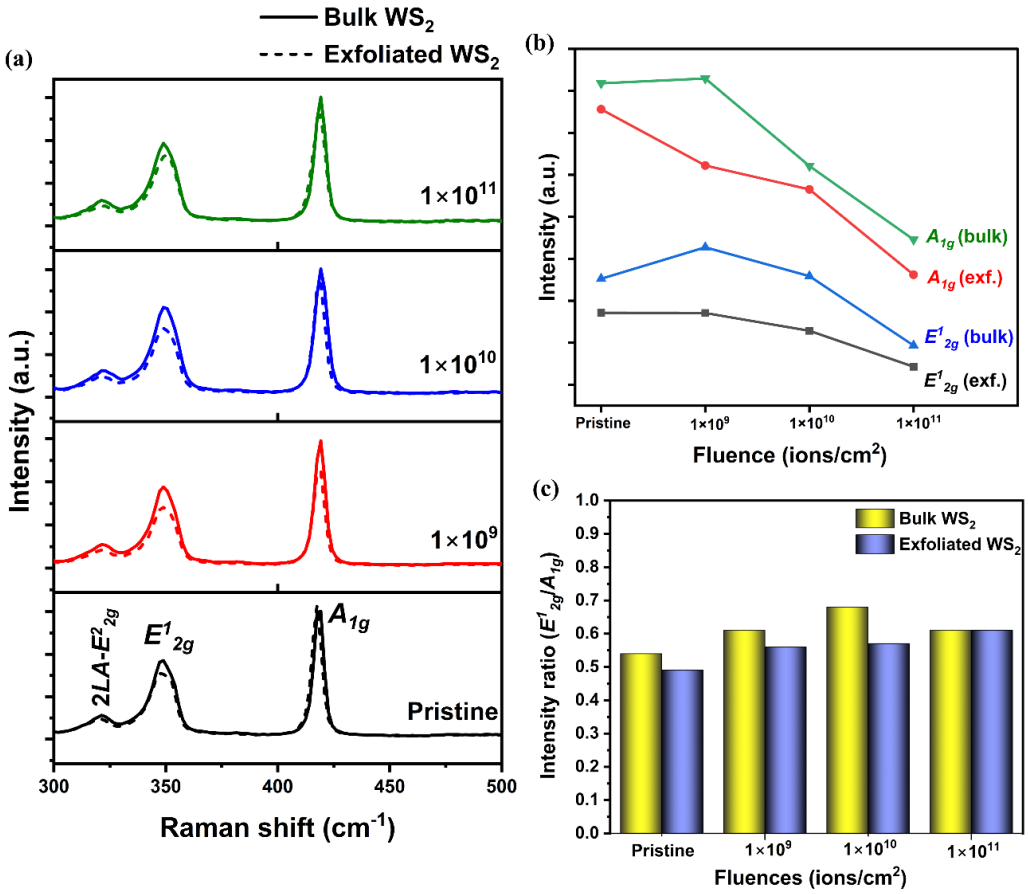

Figure 5.26: (a) Raman spectra of bulk and exfoliated WS_2 systems irradiated with 0.85 GeV U^{28+} ions, (b) decrease in intensity of Raman modes with ion fluences, (c) E^1_{2g}-to-A_{1g} intensity ratio of Raman modes with varied fluences.

crystallite sizes result from the creation and annealing of defects at high temperatures due to SHI irradiation.

Raman spectra of 0.85 GeV U^{28+} ion irradiated bulk and exfoliated WS_2 systems with varied fluences ranging from 1×10^9 - 1×10^{11} ions/cm^2 are shown in the stacked plot in Fig. 5.26 (a). The first-order optical phonon modes of WS_2 systems are denoted by in-plane (E^1_{2g}) and out-of-plane (A_{1g}) modes arising at ~350 cm^{-1} and ~418 cm^{-1} [55,56]. A minute peak appears around 321 cm^{-1}, belonging to the $2LA$-E^2_{2g} higher-order mode [57]. The intensity of Raman modes against the ion fluences was plotted for both bulk and exfoliated WS_2 systems (Fig. 5.26 (b)). The plot indicates a decrease in the intensity of vibrations between the W and S atoms with an increase in ion fluence. This signifies irradiation-induced point defect creation, such as the removal of sulfur atoms from the WS_2 structure in each case. It indicates that a higher number of vacancies are created at higher

ion fluences, and is more prevalent in exfoliated systems. The intensity ratio of E^1_{2g}-to-A_{1g} Raman modes was also calculated for each system (Fig. 5.26 (c)). The ratio significantly increases till 1×10^{10} ions/cm^2 for bulk systems, where separation of layers is predicted with high-energy 0.85 GeV irradiation. This can be predicted by the decrease in the intensity of the out-of-plane vibrational mode, while in-plane vibrational intensity comparably increases, giving a higher E^1_{2g} -to-A_{1g} ratio.

5.5.3 Core level spectra and elemental compositional analysis

The surface elemental composition and bonding states of bulk and exfoliated WS_2 systems irradiated with 0.85 GeV U^{28+} ions were investigated using XPS, as shown in Fig. 5.27 and Fig. 5.28. The XPS core-level spectra for both pristine and irradiated bulk WS_2 at a fluence of 1×10^{11} ions/cm^2 are shown in Fig. 5.27 (a-d), and the survey scans are provided in *Appendix* (Fig. A9). The fitted W 4*f* core-level spectra for the pristine system display W $4f_{7/2}$ and W $4f_{5/2}$ states, corresponding to peaks at approximately 32.3 eV and 34.4 eV,

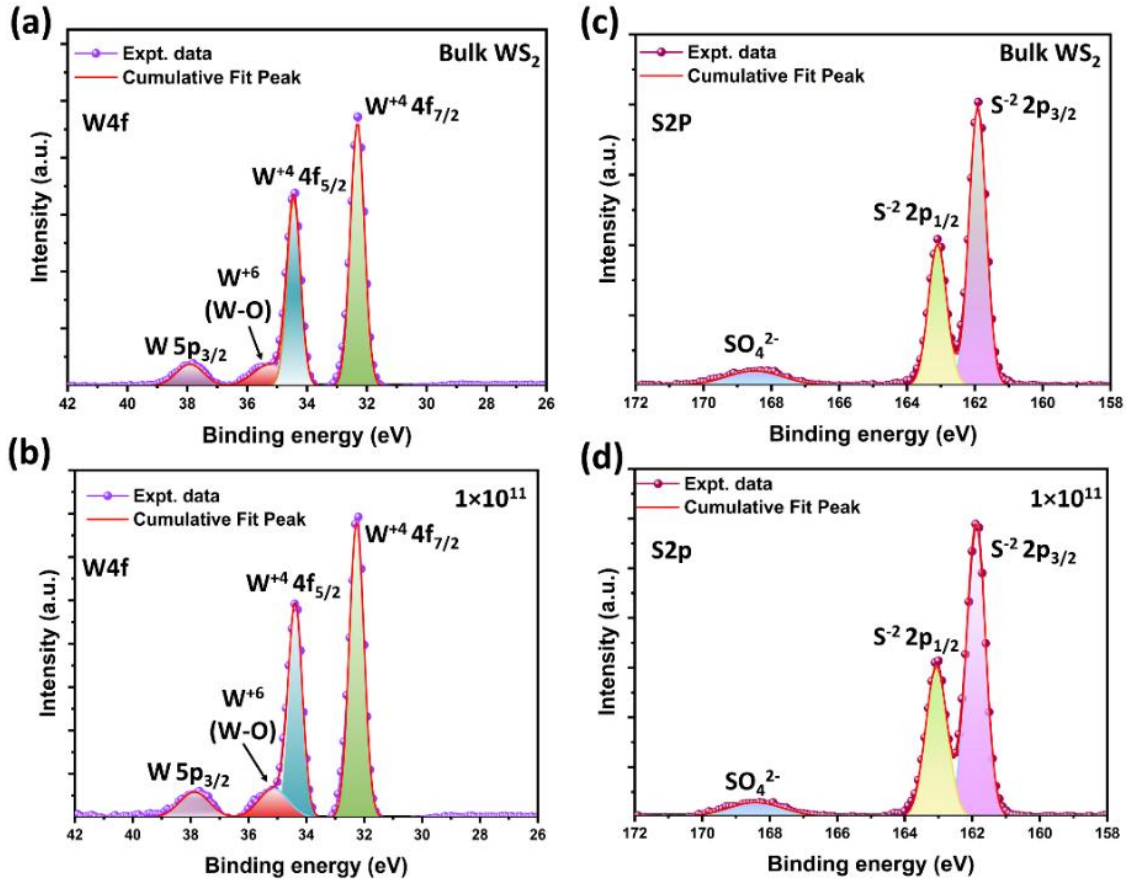

Figure 5.27: (a,b) W 4*f*-core level spectra, (c,d) S 2*p*-core level of pristine (bulk WS_2) and 0.85 GeV U^{28+} ions at fluence 1×10^{11} ions/cm^2, respectively.

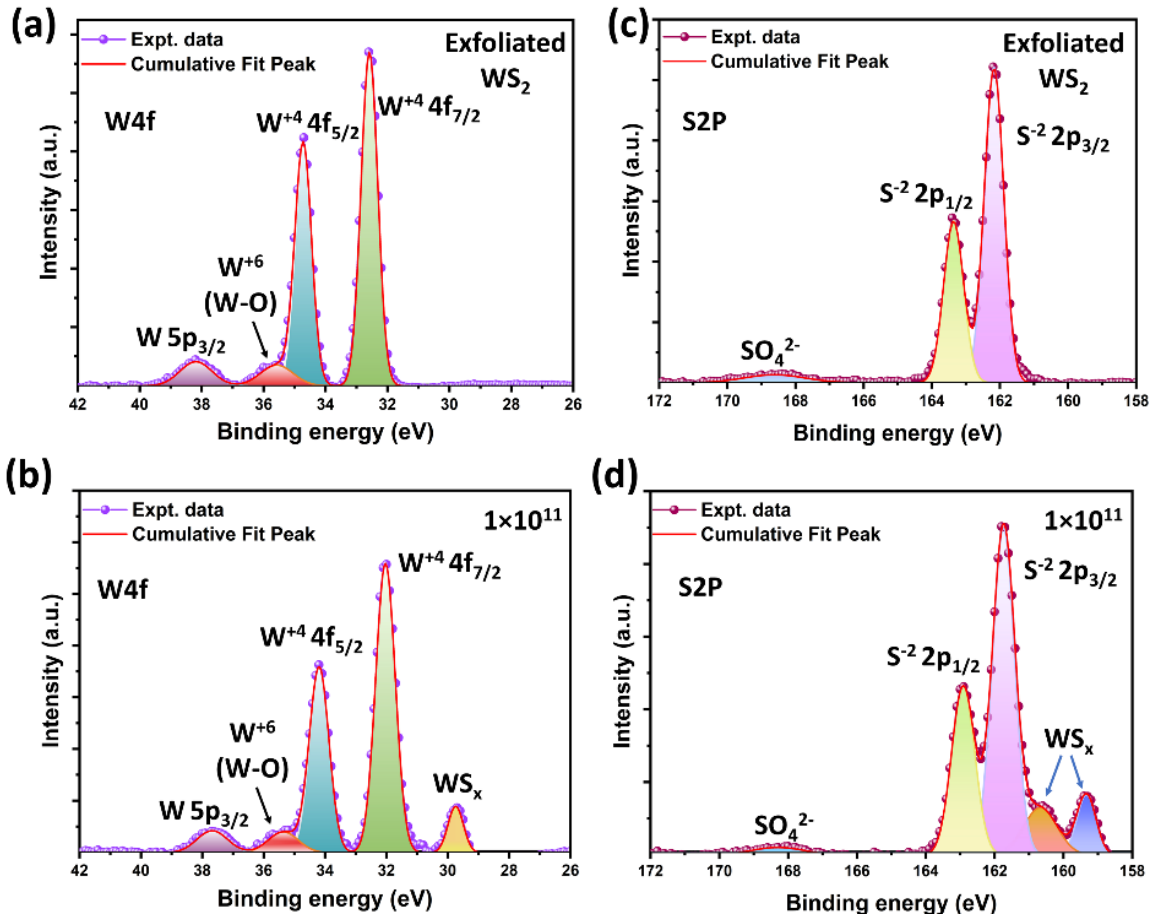

Figure 5.28: (a,b) W 4*f*-core level spectra, (c,d) S 2*p*-core level of pristine (exfoliated WS_2) and 0.85 GeV U^{28+} ions at fluence 1×10^{11} ions/cm^2, respectively.

respectively. Additionally, a broad peak near 37.9 eV represents the W $5p_{3/2}$ state, as shown in Fig. 5.27 (a) [58]. These peaks indicate the W^{4+} oxidation state characteristic of the 2H-WS_2 phase. A small shoulder peak that represents the W-O bond and the W^{6+} oxidation state also emerges at about 35.2 eV. Furthermore, the fitted S 2*p* core-level spectra reveal peaks at approximately 161.9 eV and 163.1 eV, attributed to the S $2p_{3/2}$ and S $2p_{1/2}$ states of divalent sulfide ions (S^{2-}), as shown in Fig. 5.27 (c) [59,60]. A peak near 168.5 eV indicates the presence of SO_4^{2-} in the system due to the formation of the S-O bond. While no significant shift in binding energy is observed after irradiation at a fluence of 1×10^{11} ions/cm^2, a decrease in peak intensity suggests alterations in the atomic composition of the hexagonal WS_2 structure (Fig. 5.27 (b,d)).

The elemental composition of exfoliated WS_2 systems was also analysed using XPS core-level spectra before and after irradiation at a fluence of 1×10^{11} ions/cm^2 (Fig. 5.28 (a-d)). Similar to bulk WS_2, the fitted W 4*f* core-level spectra of pristine WS_2 revealed

W $4f_{7/2}$ and W $4f_{5/2}$ states, corresponding to peaks at approximately 32.6 eV and 34.7 eV, respectively. Additionally, a broad peak associated with the W $5p_{3/2}$ state was observed near 38.2 eV, as shown in Fig. 5.28 (a). A small shoulder peak, indicating the W-O bond and the W^{6+} oxidation state, appeared at around 35.2 eV. The fitted S 2*p* core-level spectra showed peaks at approximately 162.2 eV and 163.4 eV, corresponding to the S $2p_{3/2}$ and S $2p_{1/2}$ states of divalent sulfide ions (S^{2-}), as illustrated in Fig. 5.28 (c). Furthermore, a broad feature near 168.5 eV was attributed to the existence of SO_4^{2-}. After irradiation at the highest fluence, the W $4f_{7/2}$ and W $4f_{5/2}$ states shifted slightly toward lower binding energies by ~0.6 eV and ~0.5 eV, respectively. Similarly, the S $2p_{3/2}$ and S $2p_{1/2}$ states shifted by ~0.4 eV and ~0.5 eV towards lower binding energies. These shifts in the W 4*f* and S 2*p* spectra, and also a reduction in the intensities of the peaks, indicate a sulfur deficiency, suggesting a reduced WS_{2-x} phase in the irradiated WS_2 system [61]. Moreover, new peaks emerged in both the W 4*f* and S 2*p* core-level spectra of the exfoliated system after irradiation at a fluence of 1×10^{11} ions/cm^2. Specifically, a peak appeared at ~29.74 eV in the W 4*f* core-level spectra, while peaks at ~159.3 eV and ~160.7 eV were observed in the S 2*p* core-level spectra. The development of these new peaks also indicates sulfur deficiency caused by SHI irradiation, consistent with the formation of WS_x species, where x is less than 2 [62]. This is observed only in the exfoliated systems, possibly due to a greater accumulation of defects in the material after irradiation compared to the bulk samples.

5.5.4 Morphological analysis

HR-TEM images of bulk and exfoliated WS_2 system after irradiation with 0.85 GeV U^{28+} ions at a fluence of 1×10^{11} ions/cm^2 are shown in Fig 5.29. The planar view of the HR-TEM image reveals the formation of latent tracks of a closely spherical shape in WS_2 systems after irradiation with U^{28+} ions. These tracks are mostly distinct and do not appear to overlap. The morphological analysis characterizes layered surface features and disordered zones within the track regions, embedded within the WS_2 system. The estimated average diameter of the latent tracks is found to be ~6-7 nm in both bulk and exfoliated WS_2 cases, shown as insets in Fig. 5.29 (b, d). Due to the development of latent tracks, the crystal structure becomes disordered within the track core, while the surrounding lattice retains the regular crystalline form of WS_2. The formation of these ion tracks was known to depend on the ion path length and the energy of the incident ion. Typically, a single

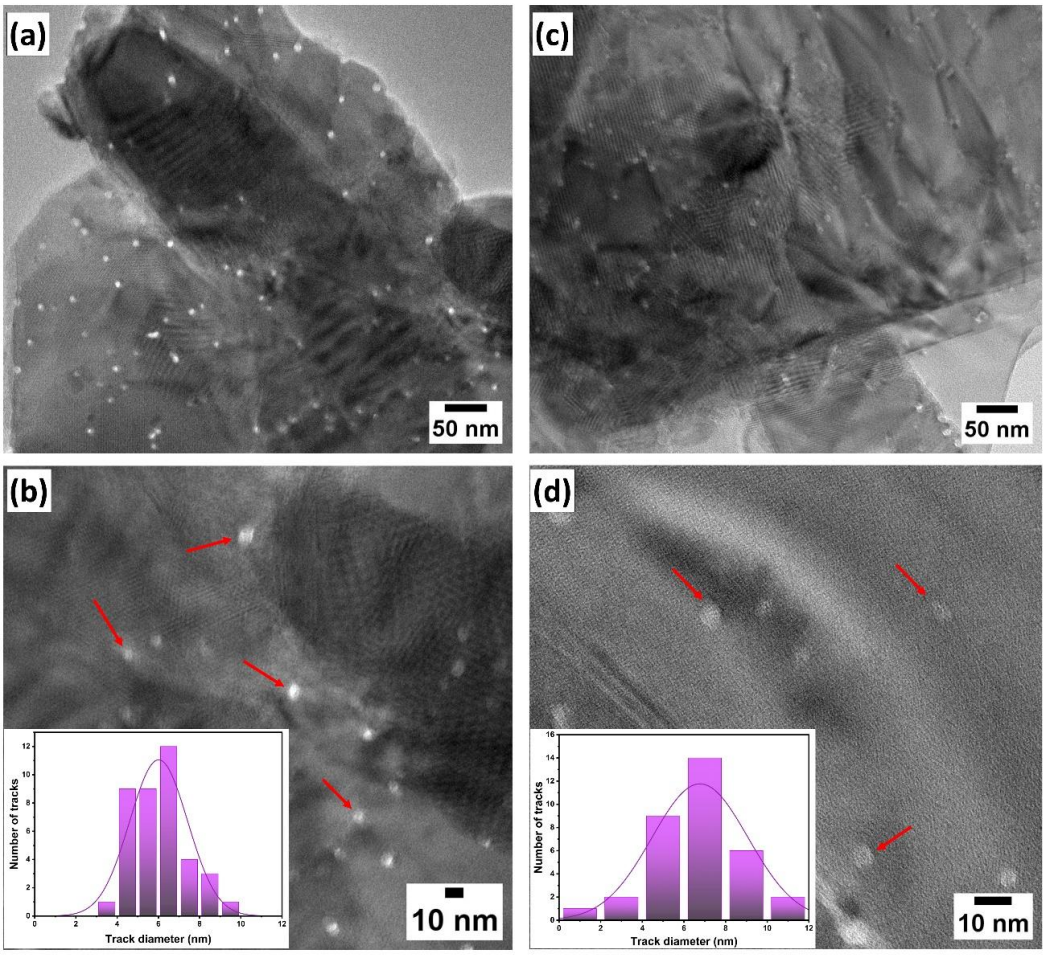

Figure 5.29: HR-TEM images of (a, b) bulk WS_2, and (c,d) exfoliated WS_2 irradiated with 0.85 GeV U^{28+} ions at a fluence of 1×10^{11} ions/cm^2.

heavy ion in the energy range of several hundred MeV to a few GeV creates a continuous ion trajectory led amorphized track, a few nanometers in width and extending over several micrometers in depth [63]. According to the thermal spike model, as the high-energy ion penetrates the material, it transfers its energy primarily to the electronic system and to the lattice atoms. This rapid energy transfer results in a localized temperature spike along the ion trajectory, sufficient to induce melting or amorphization of the material along the ion path [64,65]. The transient molten phase formed due to this intense electronic energy deposition experiences internal pressure, arising from the density difference between the molten and solid (material) phases. This pressure drives the molten material toward the top and bottom surfaces, forming hillocks. These hillocks adopt a spherical shape, as we can see from the HR-TEM images, as the potential energy and the surface area of the sphere are lowest. Upon rapid quenching, which occurs over a timescale of about 10 to 100 ps,

the transient structural modifications result in the formation of latent tracks revealed from the TEM images within the WS_2 system [66,67].

5.5.5 Low-temperature photoluminescence (PL) study

Temperature-dependent steady-state photoluminescence (PL) spectra were recorded at an excitation energy of 2.25 eV (λ_{ex} = 550 nm) for exfoliated WS_2 before irradiation (pristine) and also for bulk and exfoliated WS_2 systems, irradiated with 0.85 GeV U^{28+} ions at a fluence of 1×10^{11} ions/cm^2, along with their respective deconvoluted spectra at ~300 K are shown in Fig. 5.30 (a-f). A near-resonant excitation condition, comparable to the bandgap of the layered materials, was employed to enhance photon emission efficiency. The PL spectra were acquired over a broad temperature range, from room temperature (300 K) down to 10 K. The PL spectra of bulk WS_2 can be followed from already published articles [68,69]. After irradiation, in the bulk WS_2 system, a peak emerges at ~1.93 eV, corresponding to direct exciton (X) emission arising from band-to-band transitions at the *K*-point in the BZ (Fig. 5.30 (c)) [70]. Additionally, a broad spectral shoulder around ~1.85 eV is observed, which is found below the direct exciton peak, identified as defect-related emission (D-peak). Indirect exciton (I) peaks also appear near 1.68 eV. The indirect excitons originate from transitions between different valleys at the conduction band minimum (CBM) and valence band maximum (VBM) in the Brillouin zone [71].

The PL spectra of exfoliated WS_2 before irradiation (pristine case) show a prominent evolution of the defect emission peak near ~1.81 eV below 120 K through the noticeable splitting of the PL peak, as provided in Fig. 5.30 (a). For the exfoliated WS_2 samples irradiated at 1×10^{11} ions/cm^2, the direct exciton (X) and defect (D) emissions experience blueshift to ~2.03 eV and ~1.91 eV, respectively, from the bulk counterpart due to the reduced number of layers processed through liquid phase exfoliation (LPE) [72]. Further, the indirect exciton is observed at ~1.61 eV. The defect-related emission, which arises with an emission energy lower than the direct exciton emission, originates from exciton states bound to isolated defects or vacancies, such as sulfur vacancies, which become more abundant in the WS_2 system, particularly after irradiation. These defects act as carrier trapping centres and create multiple trap energy levels within the bandgap of the WS_2 system, enabling various optical transitions that involve either defect states, or a combination of defect states with the conduction or valence bands [73]. This defect-bound exciton emission becomes dominant below 240 K in exfoliated samples, and redshifts by

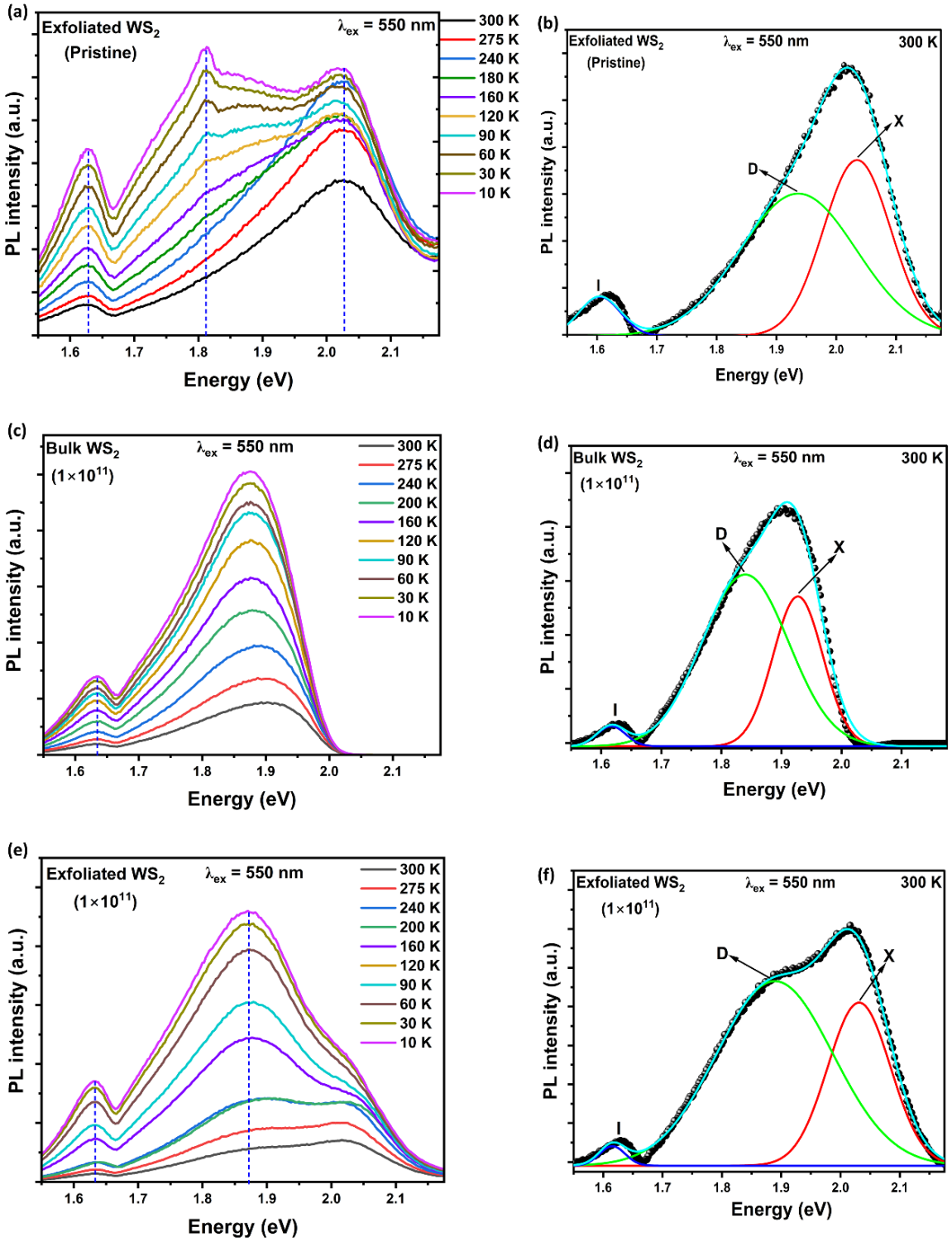

Figure 5.30: Temperature-dependent PL spectra of (a) pristine (exfoliated WS_2) without irradiation, and (c) bulk WS_2 and (e) exfoliated WS_2 after irradiation at a highest fluence of 1×10^{11} ions/cm^2, respectively varied from 10 K to 300 K, (b,d,f) deconvoluted plots shown for PL spectra of each at 300 K.

approximately 0.05 eV as the temperature cools down to 10 K. The evolution of peaks can be visualized upon deconvolution of the spectra recorded at some specific temperatures of 10 K, 90 K and 160 K, as shown in the *Appendix* (Fig. A10). The temperature dependence of PL intensity is generally stated through the relation [74]:

$$I(T) = \frac{I_0 \times k_{rad}(T)}{k_{rad}(T) + k_{nonrad}(T)}, \quad (5.5)$$

where I_0 is the maximum PL intensity at very low temperature, and $k_{rad}(T)$ and $k_{nonrad}(T)$ are the temperature-dependent radiative and nonradiative recombination rates. The nonradiative recombination rates denoted by k_{nonrad} involve the rates of defect trapping, k_{relax} and electron relaxation within the conduction and valence bands [74,75]. Moreover, the PL intensity plots specify a decrease in intensity as the temperature increases from 10 K to 300 K. This reduction can be attributed to stronger electron-phonon interactions at higher temperatures, which promote thermally activated non-radiative recombination processes. This causes a reduction in PL emission intensity, leading to a fall in quantum efficiency as the temperature rises. As the temperature increases, the direct exciton emission dominates, while the emission from defect trap states decreases above approximately 240 K, as visible from Fig. 5.30 (e) [76]. Consequently, emissions related to trap states in semiconducting materials exhibit temperature-dependent localization behaviour, being strongly localized at low temperatures and diminishing at higher temperatures, even before reaching room temperature (300 K). Therefore, the appearance of defect-related emissions facilitates non-radiative carrier transfer to defect states, leading to a reduction in the intensity of near-band-edge direct exciton emission.

Following the study reported by Sharma *et al*., which presented a low-temperature PL investigation of WS_2 nanostructures, a linear temperature dependence was observed in the range of 293-363 K when the variation in emission intensity with temperature was fitted using the proposed equation [77]:

$$I_T = I_{T_0}\,[1 + \alpha(T - T_0)], \quad (5.6)$$

where I_{T0} and I_T are the emission intensities at low temperature (T_0) set as a reference, and at absolute temperature T, respectively, and α is the first-order temperature coefficient. Following equation 5.6, the temperature dependence of PL emission intensity plots acquired for exfoliated WS_2 (pristine), and both bulk and exfoliated WS_2 systems after

irradiation at a fluence of 1×10^{11} ions/cm^2 are plotted as shown in Fig. 5.31, considering 10 K (T_0) as the reference temperature. Initially, it was assumed that emission intensity varies linearly with temperature. The linear fit to the plots based on equation (5.6) was found to adequately describe the defect-bound emissions in all cases (Fig. 5.31 (b,d,f)), as well as the direct exciton emission in irradiated bulk WS_2, as depicted in Fig. 5.31 (c). The first-order temperature coefficients, α, derived from the linear fits to the defect emission intensities of exfoliated WS_2, both pristine and irradiated at a fluence of 1×10^{11} ions/cm^2, were found to be negative, with values of 2.2×10^{-3} K^{-1} and 3.0×10^{-3} K^{-1}, respectively. For the irradiated bulk WS_2 system, the obtained negative α values for direct exciton and defect-bound emissions are 3.0×10^{-3} K^{-1} and 2.5×10^{-3} K^{-1}, respectively. However, this linear assumption may not be sufficiently accurate for displaying the direct exciton emission curve in pristine and irradiated exfoliated WS_2, particularly because the temperature dependence of PL intensity in these cases displays non-linear behaviour. To better represent this feature, a phenomenological approach was adopted by extending equation (5.6) into an empirical relation that incorporates higher-order temperature terms (up to third order). This relation is expressed as:

$$I_T = I_{T_0}\,[\alpha_0 + \alpha_1(T - T_0)^1 + \alpha_2(T - T_0)^2 + \alpha_3(T - T_0)^3], \qquad (5.7)$$

This corresponds to a third-order polynomial function, which can also be written in the form:

$$\frac{I_T}{I_{T_0}} = \sum_{n=0}^{3} \alpha_n (T - T_0)^n \qquad (5.8)$$

From the fitted plots, the coefficients α_0, α_1, α_2, and α_3 were extracted and found to be ~1, -6×10^{-3} K^{-1}, 4.08×10^{-5} K^{-2}, -0.95×10^{-7} K^{-3} for the pristine system and about 1, -5×10^{-3} K^{-1}, 4.72×10^{-5} K^{-2}, -1.26×10^{-7} K^{-3} for the irradiated exfoliated WS_2. The fitted temperature coefficient values of all the samples are presented in Table 5.7. The temperature-dependent trend of the PL intensity for direct exciton emission reveals an initial decrease as the temperature rises from 10 K to around 80 K. This is followed by a gradual increase in intensity up to approximately 200 K. Beyond this point, a sharp decline is observed, which is notably more pronounced in the exfoliated sample, as shown in Fig. 5.31 (a,e). The observed variations in the PL intensity trend suggest the involvement of multiple competing processes that influence the emission behaviour within the temperature range

of 10 K to 300 K. As the temperature increases from 10 K, the PL intensity initially decreases due to thermal quenching, likely caused by enhanced defect-mediated non-radiative recombination at low temperatures. In this regime, defect-bound exciton emission becomes prominent, originating from the interaction between direct excitons and defects introduced through irradiation or exfoliation in the exfoliated systems [78]. Further, as the

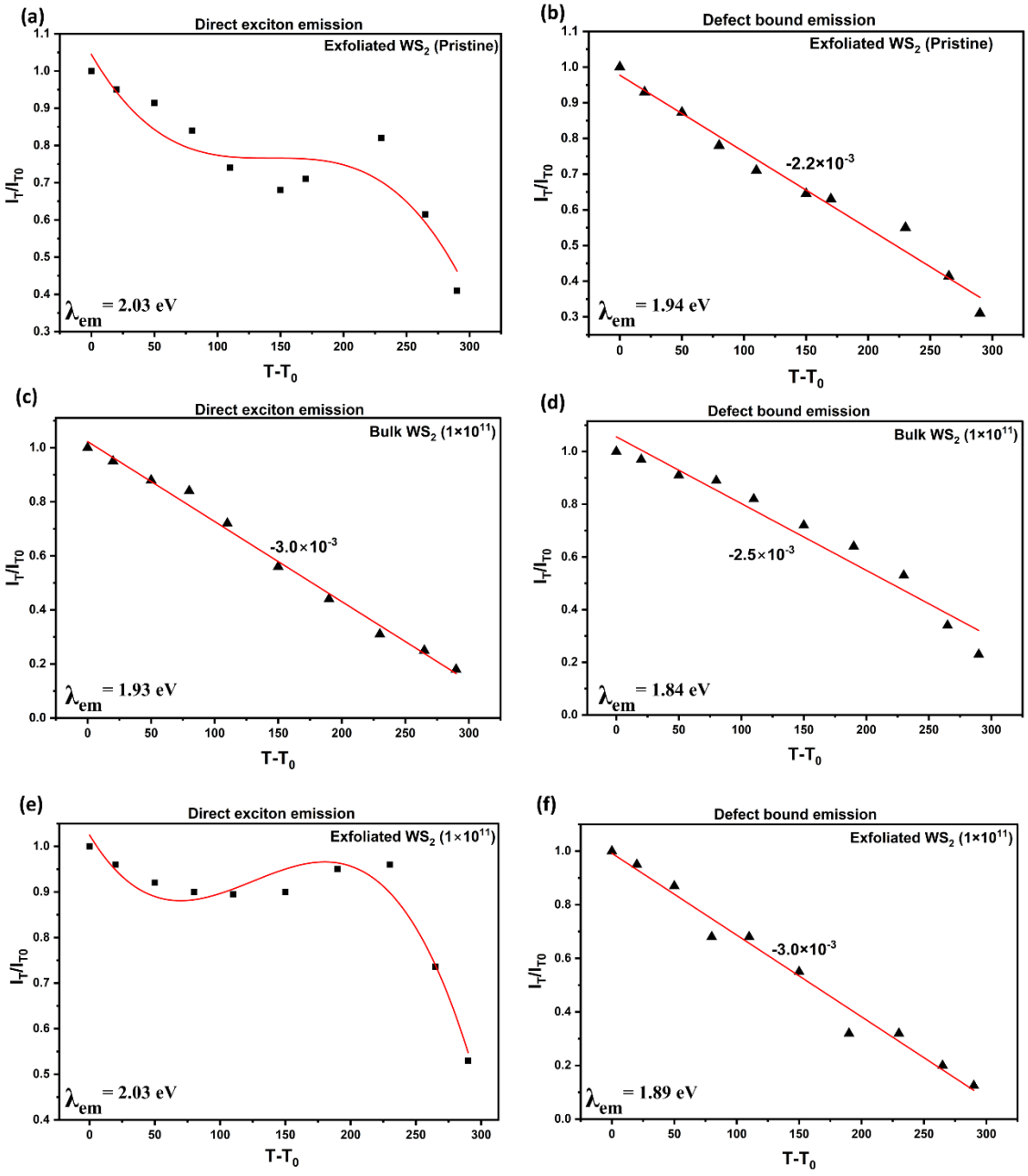

Figure 5.31: Intensity variation plots of direct exciton and defect-bound emission of (a,b) exfoliated WS_2 without irradiation (pristine), (c,d) bulk WS_2, and (e,f) exfoliated WS_2 after irradiation at a fluence of 1×10^{11} ions/cm^2 as a function of temperature.

temperature increases, an increase in the PL emission intensity at an intermediate range of ~80 K to 200 K was observed, which might be caused by the thermal activation of defect-bound excitons into free excitons and the release of electrons from deep-level trap states [79]. This effect appears to be more pronounced in the exfoliated system after irradiation, where a higher concentration of defects is expected. While at higher temperature regions of ~200-300 K, the activation of non-radiative recombination centers and the escape of

Table 5.7. Temperature coefficients (α) values for PL emission of direct and defect-bound exciton energies.

Sl. No.	Sample	Direct exciton	Defect exciton
1	Exfoliated WS_2 (pristine)	$\alpha_0 = 1$ $\alpha_1 = -6.0\times10^{-3}\ K^{-1}$ $\alpha_2 = 4.1\times10^{-5}\ K^{-2}$ $\alpha_3 = -0.95\times10^{-7}\ K^{-3}$	$\alpha = -2.2\times10^{-3}\ K^{-1}$
2	Bulk WS_2 (1×10^{11})	$\alpha = -3.0\times10^{-3}\ K^{-1}$	$\alpha = -2.5\times10^{-3}\ K^{-1}$
3	Exfoliated WS_2 (1×10^{11})	$\alpha_0 = 1$ $\alpha_1 = -5.0\times10^{-3}\ K^{-1}$ $\alpha_2 = 4.7\times10^{-5}\ K^{-2}$ $\alpha_3 = -1.3\times10^{-7}\ K^{-3}$	$\alpha = -3.0\times10^{-3}\ K^{-1}$

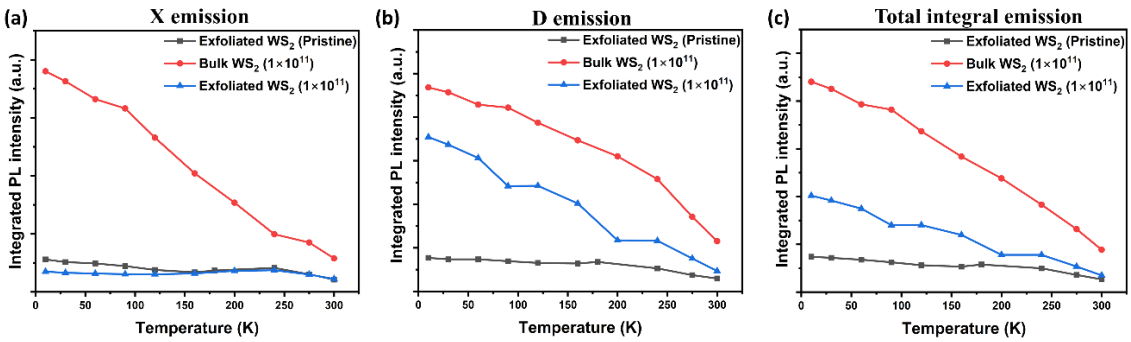

Figure 5.32: Integrated PL intensities of (a) direct exciton (X) emission, (b) defect (D) bound emission, and (c) total emission of exfoliated WS_2 (pristine) and after irradiation of bulk and exfoliated WS_2 system at a fluence of 1×10^{11} ions/cm^2 as a function of temperature.

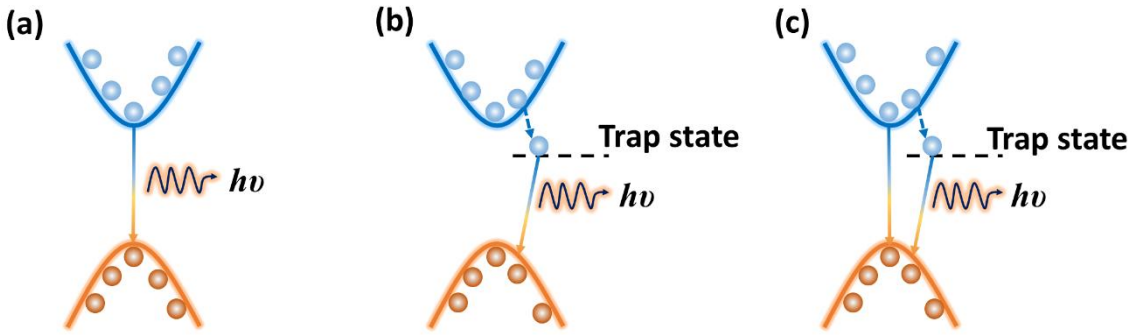

Figure 5.33: Schematic illustration showing (a) direct exciton transition, (b) defect-related exciton transition, and (c) combined emission contributions from both direct and defect-assisted transitions.

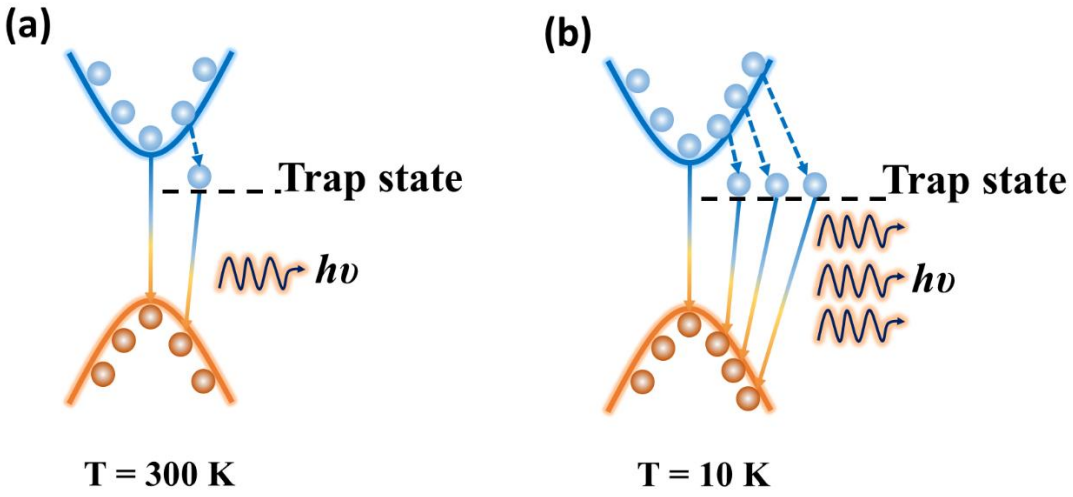

Figure 5.34: Schematic illustrating direct and defect-assisted transitions at (a) room temperature (300 K) and (b) low temperature (10 K).

carriers from the surface and defect states, as well as dissociation of excitons, can occur, leading to thermal quenching of the PL intensity [80]. Also, the possibility of a steady transition from normal scattering of phonons to Umklapp events, which demand association of non-conserved momenta, cannot be discarded.

The integrated PL intensities of the direct exciton transition, defect-bound emission, and total emission for pristine exfoliated WS_2, as well as for bulk and exfoliated WS_2 systems irradiated at a fluence of 1×10^{11} ions/cm^2, as a function of temperature, are shown in Fig. 5.32 (a-c). The schematic diagram in Fig. 5.33 illustrates the probable emission transitions in the WS_2 system, including direct exciton emission, defect-related

emission, and the combined effect of both processes. Notably, temperature-dependent quenching is evident in the integrated intensities of the emission peaks, with a more rapid decrease observed in the irradiated bulk WS_2 system. The exciton emission in the exfoliated WS_2 exhibits a 1.6-fold reduction in intensity after irradiation, as shown in Fig. 5.32 (a). However, at elevated temperatures near 300 K, the irradiated and pristine exfoliated systems display comparable emission intensities. In contrast, defect-bound emission exhibits a significant enhancement, 4.6 times stronger at 10 K post-irradiation, due to the generation of a higher defect density. At 300 K, this enhancement remains but is reduced to approximately 1.6 times compared to the pristine sample (Fig. 5.32 (b)). The enhancement in defect-related emission at 10 K, where the thermal energy is ~0.86 meV, compared to room temperature (~25.8 meV) at ~300 K, is illustrated in the schematic diagram shown in Fig. 5.34. Comparing the irradiated bulk system with the exfoliated counterpart, a significant enhancement in the integrated exciton emission intensity is observed, showing nearly an 11-fold increase at 10 K and a 2.6-fold increase at 300 K. In contrast, the defect-mediated emission exhibits a modest rise, with intensities approximately ~1.3 times higher at low temperatures and about 2.5 times higher at 300 K. The overall integrated PL intensity exhibits a similar temperature-dependent behaviour (linear to slightly sublinear) across all cases (Fig. 5.32 (c)). Moreover, the intensity ratio plots of indirect (I) to defect (D) emission and defect (D) to direct (X) emission, respectively, as shown in Fig. 5.35 (a, b). The I/D ratio is highest in pristine exfoliated WS_2 and decreases with temperature, indicating that phonon-assisted transitions are prominent in pristine material but are suppressed after irradiation due to defects induced in the system. In contrast, defect-related emission becomes dominant over direct band-edge emission at lower temperatures, particularly around 10 K, in the irradiated exfoliated WS_2 samples. However, as the temperature increases to 300 K, this ratio drops, and direct excitonic emission dominates near room temperature. Additionally, the relative quantum yield (QY) was plotted for both pristine and irradiated bulk and exfoliated WS_2, as shown in Fig. 5.35 (c). In bulk WS_2, a sharp decrease in QY is observed with increasing temperature from 10 K to 300 K after irradiation. While exfoliated WS_2 exhibits an anomalous decline in QY with temperature, with a significant reduction near room temperature (~300 K) after irradiation, signifying enhanced nonradiative recombination due to irradiation-induced defects. At low temperatures, the defect-bound PL peak becomes more pronounced because most excited-state electrons are captured by trap states

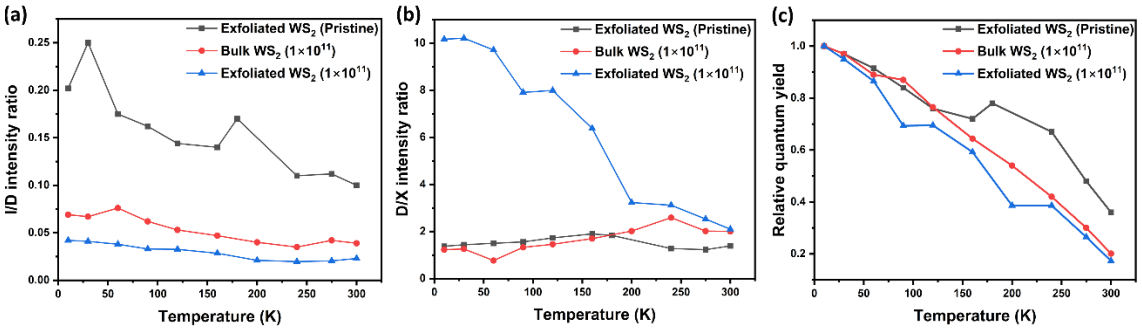

Figure 5.35: (a, b) Plots showing the intensity ratios of indirect (I) to defect (D) emission and defect (D) to direct (X) emission, and (c) the relative quantum yield of pristine exfoliated WS_2, as well as bulk and exfoliated WS_2 irradiated at a fluence of 1×10^{11} ions/cm^2, as a function of temperature.

and decay radiatively. Due to the limited thermal energy available, only a small fraction of electrons can get to the bright state via direct exciton transitions. As a result, defect-related emission is dominant, while direct exciton emission remains weak at low temperatures. As the temperature rises to 300 K, the excited electrons acquire sufficient thermal energy to escape from defect-related trap states. This can be attributed to the increased kinetic energy of the excitons, making them less prone to being captured. Additionally, the exciton and defect emission intensities in both bulk and exfoliated systems can vary from one flake to another, depending on the nature and density of vacancies introduced during or after exfoliation, and due to radiation exposure, as well as variations in the local two-dimensional electron gas concentration. Therefore, the occurrence of radiative recombination is influenced by various factors such as defect density, the presence of non-radiative transitions, electron-phonon interactions, and exciton dissociation in a material.

5.5.6 Photoluminescence decay measurements

Luminescence decay occurs through ultrafast recombination emission decay dynamics, popularly known as time-resolved process. The decay dynamics of both bulk and exfoliated pristine WS_2 and after irradiation at a fluence of 1×10^{11} ions/cm^2 are examined using time-resolved photoluminescence (TRPL) profiles, as illustrated in Fig. 5.36 (a, b), to further comprehend the inner dynamics of exciton emission, which generates the PL emission. The TRPL decay profiles provide insights into the radiative recombination of carriers, along with competing non-radiative recombination processes that affect the

overall decay profiles. The obtained TRPL profiles were fitted with a tri-exponential function,

$$B_1 e^{-t/\tau_1} + B_2 e^{-t/\tau_2} + B_3 e^{-t/\tau_3}, \quad (5.9)$$

where τ_i is the decay lifetime and B_i is the relative amplitude components. The average lifetime (τ_{av}) components of excitons that appeared in steady-state PL emission were calculated using the following formula [81],

$$\tau_{av} = \frac{B_1\tau_1^2 + B_2\tau_2^2 + B_3\tau_3^2}{B_1\tau_1 + B_2\tau_2 + B_3\tau_3} \quad (5.10)$$

The fitting parameters for the TRPL decay profiles of both pristine and irradiated WS_2 systems, at the highest fluence, are summarized in Table 5.8 using a triexponential decay function. The tri-exponential behaviour indicates that the multiple relaxation mechanisms are involved in the overall decay process.

The exciton lifetime increases from 3.64 ns in bulk WS_2 to 3.81 ns in exfoliated WS_2 before irradiation, which can be primarily attributed to defect states introduced during the exfoliation process, such as sulfur vacancies and edge states. These defects create localized states that trap excitons, allowing them to recombine and generate PL emission through localized exciton recombination. Such trapping contributes to the longer lifetime observed for these excitons. The decay components further support this, with the longer lifetime component (τ_3) increasing from 4.001 ns in bulk to 4.371 ns in exfoliated WS_2, reflecting excitons trapped in deeper or localized states and signifying the role of trap-assisted recombination. Moreover, in bulk WS_2, the fast decay parameter (τ_1) decreases from 0.13 ns to 0.11 ns, the intermediate decay parameter (τ_2) drops from 0.92 ns to 0.21 ns, and the slow decay parameter (τ_3) decreases from 4.0 ns to 2.8 ns with 0.85 GeV U^{28+} irradiation. In the exfoliated system, τ_1 remains comparable before and after irradiation, while τ_2 decreases from 0.69 ns to 0.25 ns, and τ_3 reduces from 4.4 ns to 3.3 ns. In fact, both slow and fast components become faster. This means re-trapping of carriers is less likely as compared to de-trapping of carriers, enabling them to participate in the recombination emission events. The calculated decay constants, the shorter, middle and longer lifetimes components, display a complex decay dynamic process that are ascribed to defect-bound exciton transition due to trap-assisted localized states, carrier-phonon scattering, band-edge direct exciton transition, etc. [82].

The average lifetimes (τ_{av}) of excitons decrease by 32% from 3.64 ns to 2.49 ns for the bulk system and from 3.81 ns to 3.01 ns, resulting in a 21% decrease for the exfoliated system after GeV irradiation impact (Table 5.8). This reduction in lifetimes is attributed to the presence of a non-radiative relaxation channel for neutral excitons to recombine. The presence of defects in the system induces trap states within the band gap, which act as recombination centers for carriers near the valence bands. These trap states primarily arise

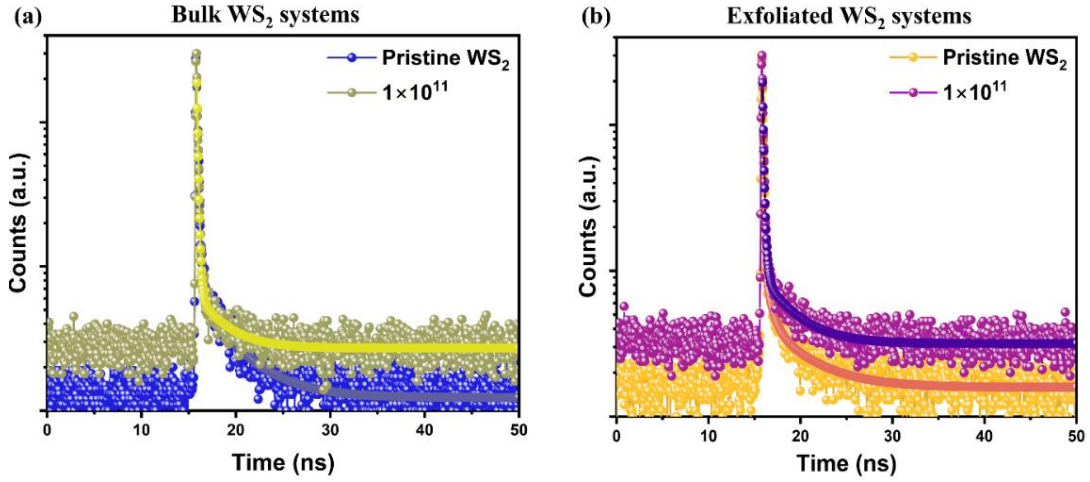

Figure 5.36: TRPL profiles of pristine WS_2 and irradiated WS_2 with 0.85 GeV U^{28+} ions at fluence 1×10^{11} ions/cm^2 for (a) bulk, and (b) exfoliated systems, respectively. The solid lines fit a tri-exponential function.

Table 5.8. Lifetime decay parameters and quantum yield estimated from the TR-PL process.

Sl. No.	Samples (fluence in ions/cm^2)	τ_1 (ns)	B_1 (%)	τ_2 (ns)	B_2 (%)	τ_3 (ns)	B_3 (%)	τ_{av} (ns)	QY (%)
1	Bulk WS_2 (Pristine)	0.132	58.53	0.916	8.45	4.001	33.02	3.64	91.0
2	Bulk WS_2 (1×10^{11})	0.108	63.88	0.206	12.55	2.822	23.57	2.49	88.2
3	Exfoliated WS_2 (Pristine)	0.108	69.78	0.687	10.14	4.371	20.08	3.81	87.2
4	Exfoliated WS_2 (1×10^{11})	0.106	46.45	0.252	19.26	3.257	34.29	3.01	92.4

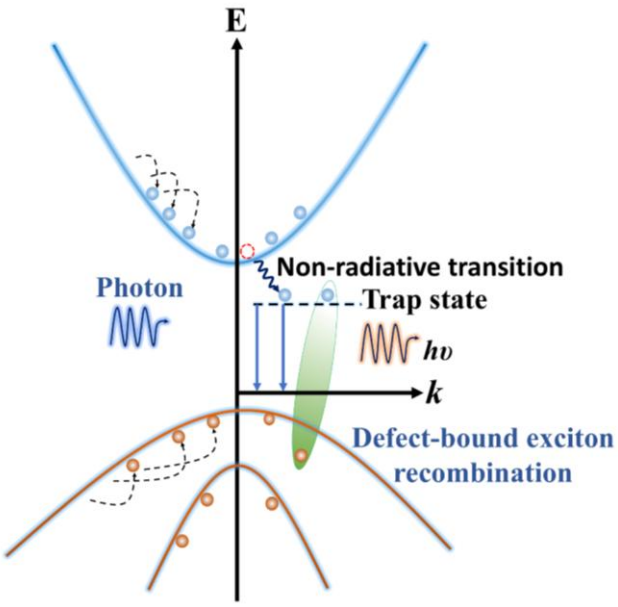

Figure 5.37: A schematic illustration of a possible carrier relaxation process witnessed in the defect-induced WS_2 system.

due to the creation of sulfur vacancies, introduced largely through irradiation. This nonradiative recombination process is due to the multiphonon emission assisted by electron-phonon coupling, where electron-phonon coupling facilitates carrier transition between the localized defect state and the delocalized state. Thus, the shortened exciton recombination lifetime results in suppressed exciton emission due to a significant reduction in the Coulomb interactions between electrons and holes [83,84]. The schematic in Fig. 5.37 illustrates the carrier relaxation processes of defects induced in the WS_2 system. In semiconducting material, intraband relaxation typically takes place via a series of carrier-carrier and carrier-phonon scattering processes. Subsequently, energy dissipation occurs via a non-radiative trapping process. In this phase, charge carriers and excitons are captured by defect-induced trap states, leading to a significant reduction in their lifetimes. These trapping events, often facilitated by single- or multi-phonon interactions, dominate the non-radiative relaxation pathways under photoexcitation. Point defects, such as sulfur vacancies, serve as highly effective trapping centers for photoexcited species, like carriers and excitons in WS_2. The relatively short lifetimes in the decay dynamics as compared to the pristine cases indicate that non-radiative mechanisms are more prominent than radiative ones in governing carrier relaxation. Additionally, the presence of trap states accelerates the relaxation dynamics of the charge carriers [85,86]. Moreover, the quantum yield (QY) corresponding to the average lifetime can be calculated using the equation [87],

$$QY = \frac{\frac{1}{\tau_r}}{\frac{1}{\tau_{avg}}}, \quad (5.11)$$

where τ_r is the radiative lifetime, and τ_{avg} is the average lifetime obtained from TR-PL decay dynamics. Using this relation, the QY (%) values were calculated for both bulk and exfoliated WS_2, before and after irradiation, shown in Table 5.8. The results indicate that bulk WS_2 exhibits a reduced QY of 88.2% after irradiation, accompanied by a shorter average lifetime, suggesting dominant non-radiative recombination events due to defect formation and manifestation. In contrast, exfoliated WS_2 offers an augment in QY of 92.4% after irradiation, even with a decline in average lifetime. This implies that the introduced defect states in the exfoliated system serve as effective radiative centers, enhancing radiative recombination pathways and thus increasing the overall emission efficiency.

5.6 Concluding remarks

In conclusion, in the ion irradiation technique, ion beam, energy, fluence, etc., play a key role in manifesting the properties of a material. This study investigates the effects of low-energy (15 keV) He^{2+}, C^{2+} ions and 0.85 GeV U^{28+} irradiation on the WS_2 system, at varied fluences. The results indicate that the phase structure and crystallinity of WS_2 remain intact even at higher fluences for all the ion types. For He^{2+} ion irradiation, the study examines the self-trapping, nucleation, and diffusion of He bubbles within the layered structures as fluence increases. Interestingly, at a fluence of 5×10^{15} ions/cm^2 under normal incidence (0°), inorganic fullerene (IF)-like structures emerge locally with polyhedral morphologies. While under oblique angle incidence (55°), the WS_2 system exhibits site-specific exfoliation and slipping of sheets.

On the other hand, 15 keV C^{2+} ion irradiation leads to the formation of an immiscible, localized WC phase within the WS_2 sheets. Raman spectra reveal the presence of D and G bands in irradiated WS_2 systems, indicating the incorporation of C atoms into these systems. To complement the experimental findings, first-principles calculations were executed. These calculations demonstrate that incorporating C through ion implantation can effectively tune the electronic bandgap of WS_2. With varying defect densities of C dopants and S vacancies, semiconducting WS_2 can transition into a gapless semi-metallic material. Furthermore, the activation energies of S and C atoms suggest that C dopants preferentially occupy vacant S sites, increasing carbon content with irradiation.

In the case of GeV irradiated WS_2 system, XPS analysis of the W 4*f* and S 2*p* core-level spectra confirms the presence of W^{4+} and S^{2-} oxidation states corresponding to the 2H-WS_2 hexagonal phase. Additionally, new peaks associated with WS_x states emerge, highlighting sulfur deficiency, which is more pronounced in the exfoliated samples. The morphological analysis of U^{28+} irradiated bulk and exfoliated WS_2 reveals the formation of ion tracks with a track diameter of ~6-7 nm. Temperature-dependent steady-state PL measurements reveal that the PL emission intensity of direct excitons exhibits a nonlinear temperature dependence, except in the case of irradiated bulk WS_2. In contrast, the defect-related emission displays a linear temperature trend, with a first-order temperature coefficient of -3.0×10^{-3} K^{-1} after irradiation. Furthermore, integrated PL intensity plots exhibit a 4.6-fold increase in the defect emission intensity after irradiation in exfoliated WS_2, as the temperature cools down to 10 K. The TRPL decay profiles show reduced exciton lifetime from 3.64 ns to 2.49 ns in the bulk system and 3.81 ns to 3.01 ns in the exfoliated case, suggesting the presence of non-radiative transitions caused by defect states arising from sulfur vacancies. Thus, ion irradiation can effectively tailor the structural, morphological and excitonic features of the material through defect creation, offering potential advantages for device applications.

References

[1] Hu, Z., Wu, Z., Han, C., He, J., Ni, Z., Chen, W. Two-dimensional transition metal dichalcogenides: interface and defect engineering. *Chemical Society Reviews*, *47*(9): 3100–3128, 2018.

[2] Khan, K., Tareen, A.K., Aslam, M., Wang, R., Zhang, Y., Mahmood, A., Ouyang, Z., Zhang, H., Guo, Z. Recent developments in emerging two-dimensional materials and their applications. *Journal of Materials Chemistry C*, *8*(2): 387–440, 2020.

[3] Wu, X., Luo, X., Cheng, H., Yang, R., Chen, X. Recent progresses on ion beam irradiation induced structure and performance modulation of two-dimensional materials. *Nanoscale*, *15*(20): 8925–8947, 2023.

[4] Seo, S.Y., Yang, D.H., Moon, G., Okello, O.F., Park, M.Y., Lee, S.H., Choi, S.Y., Jo, M.H. Identification of Point Defects in Atomically Thin Transition-Metal Dichalcogenide Semiconductors as Active Dopants. *Nano Letters*, *21*(8): 3341–3354, 2021.

[5] Bianchi, M. G., Risplendi, F., Re Fiorentin, M., Cicero, G. Engineering the electrical and optical properties of WS_2 monolayers via defect control. *Advanced Science*, *11*(4): 2305162, 2024.

[6] Li, P., Chen, S., Dai, H., Yang, Z., Chen, Z., Wang, Y., Chen, Y., Peng, W., Shan, W., Duan, H. Recent advances in focused ion beam nanofabrication for nanostructures and devices: Fundamentals and applications. *Nanoscale*, *13*(3): 1529–1565, 2021.

[7] Li, Z., Chen, F. Ion beam modification of two-dimensional materials: Characterization, properties, and applications. *Applied Physics Reviews*, *4*(1): 011103, 2017.

[8] Dhara, S. Formation, Dynamics, and Characterization of Nanostructures by Ion Beam Irradiation. *Critical Reviews in Solid State and Materials Sciences*, *32*(1–2): 1–50, 2007.

[9] Zhang, Y., Weber, W.J. Ion irradiation and modification: The role of coupled electronic and nuclear energy dissipation and subsequent nonequilibrium processes in materials. *Appl. Phys. Rev.*, *7*: 041307, 2020.

[10] Krasheninnikov, A. V, Nordlund, K. Ion and electron irradiation-induced effects in nanostructured materials. *Journal of Applied Physics*, *107*(7): 071301, 2010.

[11] Wang, J., Woller, K.B., Kumar, A., Zhang, Z., Zhou, H., Waluyo, I., Hunt, A., LeBeau, J.M., Yildiz, B. Ion irradiation to control size, composition and dispersion of metal nanoparticle exsolution. *Energy & Environmental Science*, *16*(11): 5464–5478, 2023.

[12] Muñoz-García, J., Vázquez, L., Castro, M., Gago, R., Redondo-Cubero, A., Moreno-Barrado, A., Cuerno, R. Self-organized nanopatterning of silicon surfaces by ion beam sputtering. *Materials Science and Engineering: R: Reports*, *86*: 1–44, 2014.

[13] Marchywka, M., Pehrsson, P. E., Vestyck Jr, D. J., Moses, D. Low energy ion implantation and electrochemical separation of diamond films. *Applied Physics Letters*, *63*(25): 3521–3523, 1993.

[14] Sarcan, F., Fairbairn, N.J., Zotev, P., Severs-Millard, T., Gillard, D.J., Wang, X., Conran, B., Heuken, M., Erol, A., Tartakovskii, A.I., Krauss, T.F. Understanding the

impact of heavy ions and tailoring the optical properties of large-area monolayer WS_2 using focused ion beam. *npj 2D Materials and Applications*, *7*(1): 23, 2023.

[15] Medvedev, N., Volkov, A. E., Rymzhanov, R., Akhmetov, F., Gorbunov, S., Voronkov, R., Babaev, P. Frontiers, challenges, and solutions in modeling of swift heavy ion effects in materials. *Journal of Applied Physics*, *133*(10): 100701, 2023.

[16] Wesch, W., Wendler, E. Ion beam modification of solids. *Springer Ser. Surf. Sci*, *61*: 137–182, 2016.

[17] Ziegler, J. F., Ziegler, M. D., Biersack, J. P. SRIM–The stopping and range of ions in matter. *Nuclear Instruments and Methods in Physics Research Section B: Beam Interactions with Materials and Atoms*, *268*(11–12): 1818–1823, 2010.

[18] Valappil, M. O., Anil, A., Shaijumon, M., Pillai, V. K., Alwarappan, S. A Single-Step Electrochemical Synthesis of Luminescent WS_2 Quantum Dots. *Chemistry–A European Journal*, *23*(38): 9144–9148, 2017.

[19] Muniz, F. T. L., Miranda, M. A. R., Morilla dos Santos, C., Sasaki, J. M. The Scherrer equation and the dynamical theory of X-ray diffraction. *Acta Crystallographica Section A: Foundations and Advances*, *72*(3): 385–390, 2016.

[20] Abhirami, K. M., Matheswaran, P., Gokul, B., Sathyamoorthy, R., Asokan, K. Swift heavy ion provoked structural, optical and electrical properties in SnO_2 thin films. *Applied Physics A*, *111*(4):1175–1180, 2013.

[21] Mignuzzi, S., Pollard, A.J., Bonini, N., Brennan, B., Gilmore, I.S., Pimenta, M.A., Richards, D., Roy, D. Effect of disorder on Raman scattering of single-layer MoS_2. *Physical Review B*, *91*(19): 195411, 2015.

[22] Wang, J., Ling, Q., Yao, Y., Zhu, D., Shu, S., Zhou, Z., Wu, X., Wu, P. Willow Catkin-like Co_4S_3–WS_2 Nanostructured Electrocatalyst for Efficient Overall Alkaline Water Splitting. *ACS Applied Nano Materials*, *7*(21): 24408–24416, 2024.

[23] Wang, X., Gan, X., Hu, T., Fujisawa, K., Lei, Y., Lin, Z., Xu, B., Huang, Z.H., Kang, F., Terrones, M., Lv, R. Noble-Metal-Free Hybrid Membranes for Highly Efficient Hydrogen Evolution. *Advanced materials (Deerfield Beach, Fla.)*, *29*(4): 1603617, 2017.

[24] Adilbekova, B., Lin, Y., Yengel, E., Faber, H., Harrison, G., Firdaus, Y., El-Labban, A., Anjum, D.H., Tung, V., Anthopoulos, T.D. Liquid phase exfoliation of MoS_2 and WS_2 in aqueous ammonia and their application in highly efficient organic solar cells. *Journal of Materials Chemistry C*, *8*(15): 5259–5264, 2020.

[25] Arnold, A. J., Shi, T., Jovanovic, I., Das, S. Extraordinary Radiation Hardness of Atomically Thin MoS_2. *ACS Applied Materials & Interfaces*, *11*(8): 8391–8399, 2019.

[26] York, A. P. E. Inorganic Fullerenes, Onions, and Tubes. *Journal of Chemical Education*, *81*(5): 673, 2004.

[27] Tenne, R., Margulis, L., Genut, M., Hodes, G. Polyhedral and cylindrical structures of tungsten disulphide. *Nature*, *360*(6403): 444–446, 1992.

[28] Horcas, I., Fernández, R., Gomez-Rodriguez, J. M., Colchero, J., Gómez-Herrero, J., Baro, A. M. WSxM: A software for scanning probe microscopy and a tool for nanotechnology. *Review of scientific instruments*, *78*(1): 013705, 2007.

[29] Abhijith, T., E, S., Suthar, R., Sharma, P., Thomas, S., Karak, S. Understanding the linear and nonlinear optical responses of few-layer exfoliated MoS_2 and WS_2 nanoflakes: experimental and simulation studies. *Nanotechnology*, *33*(43): 435702, 2022.

[30] Li, D.H., Zheng, H., Wang, Z.Y., Zhang, R.J., Zhang, H., Zheng, Y.X., Wang, S.Y., Zhang, D.W., Chen, L.Y. Dielectric functions and critical points of crystalline WS_2 ultrathin films with tunable thickness. *Phys. Chem. Chem. Phys.*, *19*(19): 12022–12031, 2017.

[31] Singh, B. N., Trinkaus, H. An analysis of the bubble formation behaviour under different experimental conditions. *Journal of Nuclear Materials*, *186*(2): 153–165, 1992.

[32] Li, Y. G., Zhou, W. H., Ning, R. H., Huang, L. F., Zeng, Z., Ju, X. A Cluster Dynamics Model For Accumulation Of Helium In Tungsten Under Helium Ions And Neutron Irradiation. *Communications in Computational Physics*, *11*(5): 1547–1568, 2012.

[33] Krasheninnikov, A. V, Nordlund, K. Ion and electron irradiation-induced effects in nanostructured materials. *Journal of applied physics*, *107*(7): 071301, 2010.

[34] Kalita, P., Ghosh, S., Gutierrez, G., Rajput, P., Grover, V., Sattonnay, G., Avasthi, D. K. Grain size effect on the radiation damage tolerance of cubic zirconia against simultaneous low and high energy heavy ions: Nano triumphs bulk. *Scientific Reports*, *11*(1): 10886, 2021.

[35] Van Nguyen, T., Do, H.H., Tekalgne, M., Van Le, Q., Nguyen, T.P., Hong, S.H., Cho, J.H., Van Dao, D., Ahn, S.H., Kim, S.Y. WS_2–WC–WO_3 nano-hollow spheres as an efficient and durable catalyst for hydrogen evolution reaction. *Nano Convergence*, *8*(1): 28, 2021.

[36] Bhowmick, S., Mukherjee, J., Ghosal, M., Nayak, C., Satpati, B., Pramanik, G., Karmakar, P. Green to deep-red emissive carbon dot formation by C^+ ion implantation on nitrogen beam created self-masked nano-template. *Nanotechnology*, *35*: 125301, 2024.

[37] Bhowmick, S., Mukherjee, J., Ghosal, M., Karmakar, P. Carbon ion beam induced chemical modification and nano-pyramid growth on Si surface. *Physica Scripta*, *98*: 015028, 2023.

[38] Wenzel, A., Hammerl, C., Königer, A., Rauschenbach, B. Formation of titanium carbide by high-fluence carbon ion implantation. *Nucl Instrum Methods Phys Res B*, *129*: 369–76, 1997.

[39] Bhatt, S. V, Deshpande, M. P., Sathe, V., Rao, R., Chaki, S. H. Raman spectroscopic investigations on transition-metal dichalcogenides MX_2 (M= Mo, W; X= S, Se) at high pressures and low temperature. *Journal of Raman Spectroscopy*, *45*(10): 971–979, 2014.

[40] Hao, R., Li, X., Zhang, L., Zhang, L., You, H., Fang, J. Casted MoS_2 nanostructures and their Raman properties. *Nanoscale*, *14*(29): 10449–10455, 2022.

[41] Aryeetey, F., Ignatova, T., Aravamudhan, S. Quantification of defects engineered in single layer MoS_2. *RSC advances*, *10*(39): 22996–23001, 2020.

[42] Mrabet, S. El, Abad, M. D., López-Cartes, C., Martínez-Martínez, D., Sánchez-López, J. C. Thermal evolution of WC/C nanostructured coatings by Raman and in situ XRD analysis. *Plasma Processes and Polymers*, *6*(S1): S444–S449, 2009.

[43] Parkin, W.M., Balan, A., Liang, L., Das, P.M., Lamparski, M., Naylor, C.H., Rodríguez-Manzo, J.A., Johnson, A.C., Meunier, V., Drndic, M. Raman shifts in electron-irradiated monolayer MoS_2. *ACS nano*, *10*(4): 4134–4142, 2016.

[44] Xu, D., Li, Y., Li, N., Lei, F., Liu, J., Shi, Y., Yin, L., Zhang, L. A facile synthesis of CDs from quinoa for nanosensors and bio-imagining. *Nano Express*, *1*(2): 020001, 2020.

[45] Miao, X., Qu, D., Yang, D., Nie, B., Zhao, Y., Fan, H., Sun, Z. Synthesis of carbon dots with multiple color emission by controlled graphitization and surface functionalization. *Advanced materials*, *30*(1): 1704740, 2018.

[46] Pal, A., Sk, M. P., Chattopadhyay, A. Recent advances in crystalline carbon dots for superior application potential. *Materials Advances*, *1*(4): 525–553, 2020.

[47] Yoshimura, A., Lamparski, M., Kharche, N., Meunier, V. First-principles simulation of local response in transition metal dichalcogenides under electron irradiation. *Nanoscale*, *10*(5): 2388–2397, 2018.

[48] Ma, L., Tan, Y., Ghorbani-Asl, M., Boettger, R., Kretschmer, S., Zhou, S., Huang, Z., Krasheninnikov, A.V., Chen, F. Tailoring the optical properties of atomically-thin WS_2 via ion irradiation. *Nanoscale*, *9*(31): 11027–11034, 2017.

[49] Ullah, H., Kim, H. J., Shin, Y.-H. Influences of vacancy and doping on electronic and magnetic properties of monolayer SnS. *Journal of Applied Physics*, *124*(6): 2018.

[50] Lau, C.S., Chee, J.Y., Ang, Y.S., Tong, S.W., Cao, L., Ooi, Z.E., Wang, T., Ang, L.K., Wang, Y., Chhowalla, M., Goh, K.E.J. Quantum Transport in Two-Dimensional WS_2 with High-Efficiency Carrier Injection through Indium Alloy Contacts. *ACS Nano*, *14*(10): 13700–13708, 2020.

[51] Tan, Q.H., Ren, S.L., Shen, T., Liu, X.L., Shi, W., Sun, Y.J., Deng, H.X., Tan, P.H., Zhang, J. Unraveling the Defect Emission and Exciton–Lattice Interaction in Bilayer WS_2. *The Journal of Physical Chemistry C*, *123*(7): 4433–4440, 2019.

[52] Cui, Z., Yang, K., Shen, Y., Yuan, Z., Dong, Y., Yuan, P., Li, E. Toxic gas molecules adsorbed on intrinsic and defective WS_2: gas sensing and detection. *Applied Surface Science*, *613*: 155978, 2023.

[53] Yang, X., Dong, Z., Sun, C. Q. Effects of doping concentration on bond length and bond energy studied by Raman shift. *Applied Physics Letters*, *123*(5): 053101, 2023.

[54] Yan, J., Lian, S., Cao, Z., Du, Y., Wu, P., Sun, H., An, Y. CVD controlled preparation and growth mechanism of 2H-WS_2 nanosheets. *Vacuum*, *207*: 111564, 2023.

[55] Mohan, V. V, Manuraj, M., Anjana, P. M., Rakhi, R. B. WS_2 nanoflowers as efficient electrode materials for supercapacitors. *Energy Technology*, *10*(3): 2100976, 2022.

[56] Rawat, S., Bamola, P., Bisht, M., Bhandari, B. S., Dwivedi, C., Sharma, H. Temperature dependence Raman spectroscopy studies of CVD grown few layer MoS_2 triangular domains. *Materials Today: Proceedings,* 2023.

[57] Sourisseau, C., Cruege, F., Fouassier, M., Alba, M. Second-order Raman effects, inelastic neutron scattering and lattice dynamics in 2H-WS_2. *Chemical Physics*, *150*(2): 281–293, 1991.

[58] Jha, R. K., Nanda, A., Bhat, N. Ultrasonication assisted fabrication of a tungsten sulfide/tungstite heterostructure for ppb-level ammonia detection at room temperature. *RSC advances*, *10*(37): 21993–22001, 2020.

[59] Urbanová, V., Lazar, P., Antonatos, N., Sofer, Z., Otyepka, M., Pumera, M. Positive and Negative Effects of Dopants toward Electrocatalytic Activity of MoS_2 and WS_2: Experiments and Theory. *ACS Applied Materials & Interfaces*, *12*(18): 20383–20392, 2020.

[60] Lei, T., Chen, W., Huang, J., Yan, C., Sun, H., Wang, C., Zhang, W., Li, Y., Xiong, J. Multi-functional layered WS_2 nanosheets for enhancing the performance of lithium–sulfur batteries. *Advanced Energy Materials*, *7*(4): 1601843, 2017.

[61] Kastl, C., Koch, R.J., Chen, C.T., Eichhorn, J., Ulstrup, S., Bostwick, A., Jozwiak, C., Kuykendall, T.R., Borys, N.J., Toma, F.M., Aloni, S. Effects of Defects on Band Structure and Excitons in WS_2 Revealed by Nanoscale Photoemission Spectroscopy. *ACS Nano*, *13*(2): 1284–1291, 2019.

[62] Kieczka, D., Bussolotti, F., Maddumapatabandi, T.D., Bosman, M., Shluger, A., Regoutz, A., Goh, K.E.J. Unveiling surface dynamics: in situ oxidation of defective WS_2. *Nanoscale*, 17: 10082–10094, 2025.

[63] Amekura, H., Chettah, A., Narumi, K., Chiba, A., Hirano, Y., Yamada, K., Yamamoto, S., Leino, A.A., Djurabekova, F., Nordlund, K., Ishikawa, N. Latent ion tracks were finally observed in diamond. *Nature Communications*, *15*(1): 1786, 2024.

[64] Zhang, S., Hu, P., Xu, L., Chen, H., Maaz, K., Zhai, P., Li, Z., Liu, L., Ai, W., Zeng, J., Liu, J. Exciton Transitions in Monolayer WS_2 Activated by Swift Heavy Ion Irradiation. *The Journal of Physical Chemistry C*, *125*(37): 20389–20396, 2021.

[65] Toulemonde, M., Trautmann, C., Balanzat, E., Hjort, K., Weidinger, A. Track formation and fabrication of nanostructures with MeV-ion beams. *Nuclear Instruments and Methods in Physics Research Section B: Beam Interactions with Materials and Atoms*, *216*: 1–8, 2004.

[66] Xu, L.J., Zhai, P.F., Zhang, S.X., Zeng, J., Hu, P.P., Li, Z.Z., Liu, L., Sun, Y.M., Liu, J. Characterization of swift heavy ion tracks in MoS_2 by transmission electron microscopy. *Chinese Physics B*, *29*(10): 106103, 2020.

[67] Krasheninnikov, A. V, Nordlund, K. Ion and electron irradiation-induced effects in nanostructured materials. *Journal of Applied Physics*, *107*(7): 071301, 2010.

[68] Molas, M. R., Nogajewski, K., Slobodeniuk, A. O., Binder, J., Bartos, M., Potemski, M. The optical response of monolayer, few-layer and bulk tungsten disulfide. *Nanoscale*, *9*(35): 13128–13141, 2017.

[69] Cong, C., Shang, J., Wang, Y., Yu, T. Optical properties of 2D semiconductor WS_2. *Advanced Optical Materials*, *6*(1): 1700767, 2018.

[70] Liu, H., Wang, C., Zuo, Z., Liu, D., Luo, J. Direct visualization of exciton transport in defective few-layer WS_2 by ultrafast microscopy. *Advanced Materials*, *32*(2): 1906540, 2020.

[71] Tan, Q.H., Ren, S.L., Shen, T., Liu, X.L., Shi, W., Sun, Y.J., Deng, H.X., Tan, P.H., Zhang, J. Unraveling the Defect Emission and Exciton–Lattice Interaction in Bilayer WS_2. *The Journal of Physical Chemistry C*, *123*(7): 4433–4440, 2019.

[72] Rahman, M.A., Yomogida, Y., Ahad, A., Ueji, K., Nagano, M., Ihara, A., Nishidome, H., Omoto, M., Saito, S., Miyata, Y., Gao, Y. Synthesis and optical properties of WS_2 nanotubes with relatively small diameters. *Scientific Reports*, *13*(1): 16959, 2023.

[73] Singh, A., Dey, P., Kumari, A., Sikdar, M. K., Sahoo, P. K., Das, R., Maiti, T. Temperature-dependent excitonic emission characteristics of lead-free inorganic double perovskites and their third-order optical nonlinearities. *Physical Chemistry Chemical Physics*, *24*(6): 4065–4076, 2022.

[74] Nan, H., Wang, Z., Wang, W., Liang, Z., Lu, Y., Chen, Q., He, D., Tan, P., Miao, F., Wang, X., Wang, J. Strong Photoluminescence Enhancement of MoS_2 through Defect Engineering and Oxygen Bonding. *ACS Nano*, *8*(6): 5738–5745, 2014.

[75] Chen, Y., Wen, W., Zhu, Y., Mao, N., Feng, Q., Zhang, M., Hsu, H.P., Zhang, J., Huang, Y.S., Xie, L. Temperature-dependent photoluminescence emission and Raman scattering from $Mo_{1-x}W_xS_2$ monolayers. *Nanotechnology*, *27*(44): 445705, 2016.

[76] Wu, K., Zhong, H., Guo, Q., Tang, J., Yang, Z., Qian, L., Yuan, S., Zhang, S., Xu, H. Revealing the competition between defect-trapped exciton and band-edge exciton photoluminescence in monolayer hexagonal WS_2. *Advanced Optical Materials*, *10*(6): 2101971, 2022.

[77] Sharma, S., Bhagat, S., Singh, J., Ahmad, M., Sharma, S. Temperature dependent photoluminescence from WS_2 nanostructures. *Journal of Materials Science: Materials in Electronics*, *29*(23): 20064–20070, 2018.

[78] Davila, Y.G., Silva, F.W., Oliveira, M.C., Yu, Z., Carvalho, T.C., dos Santos, C.C., Souza Filho, A.G., Terrones, M., Alencar, R.S., Viana, B.C. Temperature and power-dependent photoluminescence spectroscopy in suspended WSe_2 monolayer. *Journal of Physics D: Applied Physics*, *57*(16): 165304, 2024.

[79] Lu, W., Tarekegne, A. T., Ou, Y., Kamiyama, S., Ou, H. Temperature-dependent photoluminescence properties of porous fluorescent SiC. *Scientific Reports*, *9*(1): 16333, 2019.

[80] Fu, X., Li, H., Yue, H., Li, Z., Feng, J., Zhang, H. Cr^{3+}/Yb^{3+} Codoped $Cs_2NaInCl_6$ Double Perovskites for Near-Infrared Light-Emitting Diodes. *Inorganic Chemistry*, *64*(17): 8782–8791, 2025.

[81] De, C. K., Routh, T., Roy, D., Mandal, S., Mandal, P. K. Highly Photoluminescent InP Based Core Alloy Shell QDs from Air-Stable Precursors: Excitation Wavelength

Dependent Photoluminescence Quantum Yield, Photoluminescence Decay Dynamics, and Single Particle Blinking Dynamics. *The Journal of Physical Chemistry C*, *122*(1): 964–973, 2018.

[82] Li, Y., Wu, X., Liu, W., Xu, H., Liu, X. Revealing the interrelation between C-and A-exciton dynamics in monolayer WS_2 via transient absorption spectroscopy. *Applied Physics Letters*, *119*(5): 051106, 2021.

[83] Liu, Y., Liu, H., Wang, J., Liu, D. Defect-Type-Dependent Carrier Lifetimes in Monolayer WS_2 Films. *The Journal of Physical Chemistry C*, *126*(10): 4929–4938, 2022.

[84] Abakumov, V. N., Perel, V. I., Yassievich, I. N. *Nonradiative Recombination in Semiconductors*, ISBN:9780444600820, North Holland, 1991.

[85] Gao, L., Hu, Z., Lu, J., Liu, H., Ni, Z. Defect-related dynamics of photoexcited carriers in 2D transition metal dichalcogenides. *Physical Chemistry Chemical Physics*, *23*(14): 8222–8235, 2021.

[86] Shi, H., Yan, R., Bertolazzi, S., Brivio, J., Gao, B., Kis, A., Jena, D., Xing, H.G., Huang, L. Exciton Dynamics in Suspended Monolayer and Few-Layer MoS_2 2D Crystals. *ACS Nano*, *7*(2): 1072–1080, 2013.

[87] Yuan, L., Huang, L. Exciton dynamics and annihilation in WS_2 2D semiconductors. *Nanoscale*, *7*(16): 7402–7408, 2015.